Ville Kivijärvi

Numerical optimization of grating couplers in nanophotonic waveguides

School of Electrical Engineering

Thesis submitted for examination for the degree of Master of Science in Technology.

Espoo 4.3.2014

Thesis supervisor:

Prof. Ilkka Tittonen

Thesis advisor:

M.Sc. Mikhail Erdmanis

Aalto University
School of Electrical
Engineering

AALTO-YLIOPISTO
SÄHKÖTEKNIIKAN KORKEAKOULU

DIPLOMITYÖN
TIIVISTELMÄ

Tekijä: Ville Kivijärvi

Työn nimi: Diffraktioon perustuvien hilakytkinten numeerinen optimointi nanofotonisissa aaltojohdoissa

Päivämäärä: 4.3.2014 Kieli: Englanti Sivumäärä:9+86

Mikro- ja nanotekniikan laitos

Professuuri: Optinen Teknologia Koodi: S-3011

Valvoja: Prof. Ilkka Tittonen

Ohjaaja: DI Mikhail Erdmanis

Optisten taajuuksien käyttö tietotekniikassa voi mahdollistaa nykyistä suuremmat kaistanleveydet ja pienemmän energian kulutuksen. Piifotoniikka pyrkii ohjaamaan ja manipuloimaan näitä taajuuksia piialustalla. Piifotoniikalla on sovelluksia esimerkiksi sensoritekniikassa ja tietoverkoissa. Epäsuora energia-aukko estää tehon tuottamisen suoraan piialustalla, jolloin optinen teho täytyy tuoda piihin ulkoisesta lähteestä. Tämä edellyttää kytkennän rakentamista teholähteen ja sirun välille. Kytkentä voidaan toteuttaa esimerkiksi diffraktiohilan avulla. Diffraktiohilan etuja ovat joustava sijoitus piirilevylle ja samanaikainen kytkeytyminen useisiin signaalilähteisiin. Hilan aallonpituusriippuvuus vaikuttaa kytkentään, joka on tehokas ainoastaan hilalle ominaisella resonanssitaajuudella. Kytkentähyötysuhde riippuu diffraktiohilan geometriasta, kuten sen koosta, jaksollisuudesta ja hilaelementtien muodoista. Hyötysuhteen maksimointi voidaankin toteuttaa hilan geometriaa optimoimalla. Tämä työ käsittelee kytkentähyötysuhteen parantamista geometrian avulla. Optimointi perustuu numeeriseen mallinnukseen FEM-menetelmällä (Finite Element Method). FEM-menetelmän käyttö on perusteltua, koska äärellisen kokoisten hilarakenteiden analyyttinen mallintaminen on vaikeaa mielivaltaisille geometrioille. Riittävän suuri parametrisilmukka pystyy käymään useimmat geometriat läpi, jolloin erilaisten vaihtoehtojen joukosta löydetään optimaalinen geometria. Tällainen laskenta hyötyy FEM-menetelmän eduista, joihin kuuluu lyhyt laskenta-aika. Tämän työn laskennassa hyödynnettiin COMSOL Multiphysics ohjelmistoa, koska kyseinen ohjelmisto mahdollistaa parametrisilmukoiden automatisoinnin. Optimoinnin jälkeen saavutettuja taajuusvasteita verrattiin alkuperäiseen taajuusvasteeseen. Näin voitiin varmistua siitä, että saavutettu aallonpituusriippuvuus vastaa teoriaa parantuneella maksimihyötysuhteella. Taajuusvasteella on voimakas maksimi resonanssiaallonpituudella, mikä havaittiin kaikilla optimoiduilla geometrioilla.

Avainsanat: Kytkentähyötysuhde, Fotoniikka, Simulaatio, SOI, FEM, Aaltojohto, Valokuitu, Diffraktiohila, Gaussinen säde, Aaltomuoto

AALTO UNIVERSITY
SCHOOL OF ELECTRICAL ENGINEERING

ABSTRACT OF THE
MASTER'S THESIS

Author: Ville Kivijärvi

Title: Numerical optimization of grating couplers in nanophotonic waveguides

Date: 4.3.2014 Language: English Number of pages:9+86

Department of Micro- and Nanosciences

Professorship: Optical Technology Code: S-3011

Supervisor: Prof. Ilkka Tittonen

Advisor: M.Sc. Mikhail Erdmanis

Use of optical frequencies in information technology can provide increased bandwidth and reduced energy consumption compared to modern applications. In silicon photonics, optical signals are processed in circuits that are mainly based on silicon and silica structures. Silicon photonic applications can be utilized, for example, in sensors and in telecommunication networks. The indirect bandgap of silicon prevents the construction of a laser type power source on a silicon substrate. Hence, power in silicon photonics has to be produced outside the chip. This demands a device, which can couple signal power to silicon. One example of such a device is a diffraction grating. Gratings can be flexibly placed on the chip and they can couple to multiple power sources simultaneously. When a grating coupler is utilized, one crucial parameter that defines its performance is the coupling efficiency. This figure denotes the fraction of source power, which can be transmitted to the chip. Many studies have been performed to maximize this fraction. Coupling efficiency depends on the grating geometry, which can be optimized by altering the grating parameters, such as period or groove depth. In this work, such optimization was performed by simulating the grating structure while varying the geometric dimensions. Numerical simulation is necessary because finite sized gratings cannot be modelled analytically for arbitary shapes. The simulations were performed on finite element method (FEM) using the COMSOL Multiphysics software. An advantage of the FEM is fast calculation, essential when computing large scale parametric sweeps required by the optimization procedure. The main objective of this study was to compare the initial and optimized frequency responses as they define the coupling efficiency and the operation bandwidth. The comparison revealed an improved coupling at the resonance wavelength for certain geometries found by the sweeps. The achieved frequency responses around this maximum are in agreement with grating theory and previous studies made on the topic.

Keywords: Coupling Efficiency, Photonics, Simulation, SOI, FEM, Waveguide, Optical fiber, Diffraction grating, Gaussian beam, Mode

Preface

This thesis is wide, and many people have helped me during the process. First, I would like to thank professor Ilkka Tittonen for his patience during this project. Second, I would like to thank him for an opportunity to work in the MQS (Micro- and quantum systems) group in Micronova nanotechnology centre, with a topic, which I found very interesting.

I would like to thank my supervisor Mikhail Erdmanis for his assistance. I want to thank him for a great amount of advice, providing me references, and for reading my work through. Thank you for developing my writing skills and introducing me to the research of photonics.

I also want to thank Ville Pale for good instructions in writing. These instructions made my work clearer and understandable for someone not involved in the topic. Actually, I should thank all the MQS personnel for practical advice and good working atmosphere.

Special thanks for Julius Nieminen, Christoffer Kauppinen, Perttu Sippola, Patrick Grahn, Anna Mannila, Sami Kujala, Osmo Vänskä, Andriy Shevchenko, and Mikko Ruoho, for your opinions of my work and my writing style.

In addition, I would like to thank Aalto Department of Radio Science and Engineering for offering me the basic theory necessary to understand the behaviour of light. For same reasons, I would like to thank Matti Kaivola and his group for many interesting courses in optical technology that formed the basis of this work.

Last, I would like to thank my friends and relatives. Your support was crucial to complete this thesis as I completed it.

Otaniemi,4.3.2014

Ville S. Kivijärvi

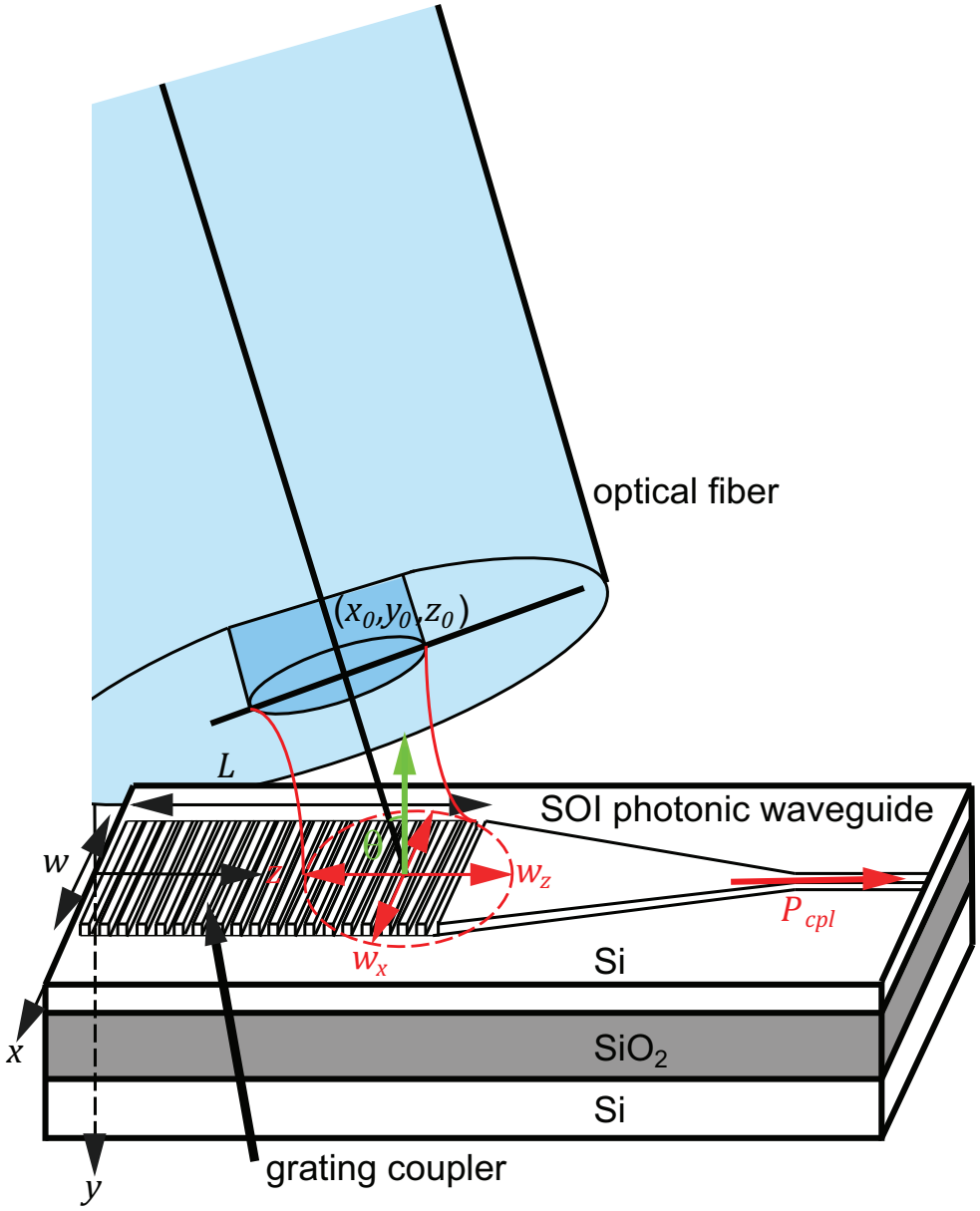

Figure 0.1: Grating coupler and a single mode fiber. Taken from [1].

Contents

Symbols and Abbreviations

Symbols

$i = \sqrt{-1}$	imaginary unit
(x, y, z)	cartesian coordinates
$(\hat{\mathbf{x}}, \hat{\mathbf{y}}, \hat{\mathbf{z}})$	cartesian unit vectors
$\hat{\mathbf{m}}$	unit vector in $\mathbf{m}$ direction
r	distance from the origin
$\mathbf{r}$	position vector
$\hat{\mathbf{r}}$	unit vector in $\mathbf{r}$ direction
ρ	distance from the z axis
ρ	position vector in cylindrical coordinates
$\hat{\rho}$	unit vector in ρ direction
t	PML-layer length variable
S	surface area
$\mathrm{d}S$	differential surface area
$\mathbf{S}$	directed surface area
$\mathbf{dS}$	differential vector surface area
$\mathrm{d}l$	differential length in $\mathbf{l}$ direction
$\mathbf{dl}$	differential path length vector
$\mathbf{n}$	surface normal (unit vector)
D	computational domain
∂D	edge of domain D
f	frequency
c	speed of light in vacuum
$\hbar$	reduced Planck's constant
λ	wavelength in vacuum
n	refractive index
k	wavenumber
$\mathbf{k}$	wavevector
β	propagation constant, wavenumber longitudinal component
α	attenuation
ω	angular frequency
t	time
Λ	grating period
L_{cpl}	coupling length
η	efficiency, coupling efficiency
N	grating groove number, number of objects
d	distance
w	width, Gaussian width measured between e^{-1} points
σ	standard deviation, Gaussian width
$G(z)$	Gaussian profile
P	power
E	electric field strength

$\mathbf{E}$	electric field
H	magnetic field strength
$\mathbf{H}$	magnetic field
I	intensity
S	Poynting's vector amplitude
$\mathbf{S}$	Poynting's vector
$\epsilon = \epsilon_0 \epsilon_r$	permittivity
$\mu = \mu_0 \mu_r$	permeability
R	Fresnel reflection coefficient
T	Fresnel transmission coefficient
N_i	linear nodal shape functions
$\mathbf{w}_l$	curl conforming vector basis functions

Operators

$\mathbf{a} \cdot \mathbf{b} = a_x b_x + a_y b_y + a_z b_z$	dot product of vectors $\mathbf{a}$ and $\mathbf{b}$
$\mathbf{a} \times \mathbf{b} =$ $\hat{\mathbf{x}}\left(a_y b_z - b_y a_z\right) - \hat{\mathbf{y}}\left(a_x b_z - b_x a_z\right) + \hat{\mathbf{z}}\left(a_x b_y - b_x a_y\right)$	cross product of vectors $\mathbf{a}$ and $\mathbf{b}$
$\nabla = \hat{\mathbf{x}}\frac{\partial}{\partial x} + \hat{\mathbf{y}}\frac{\partial}{\partial y} + \hat{\mathbf{z}}\frac{\partial}{\partial z}$	gradient operator
$\nabla\left(F\right) = \hat{\mathbf{x}}\frac{\partial F}{\partial x} + \hat{\mathbf{y}}\frac{\partial F}{\partial y} + \hat{\mathbf{z}}\frac{\partial F}{\partial z}$	gradient of function F
$\nabla \cdot \mathbf{F}$	divergence of function $\mathbf{F}$
$\nabla \times \mathbf{F}$	curl of function $\mathbf{F}$
$\lvert F \rvert$	absolute value of number or function F
$\lvert \mathbf{F} \rvert$	vector norm of $\mathbf{F}$ ("length" of the vector)
$\int_D F \mathrm{d}V$	integral of function F over volume D
$\int_{\partial D} F \mathrm{d}S$	integral of function F over boundary of D
$\int_S \mathbf{F} \cdot \mathbf{dS}$	integral of function $\mathbf{F}$ over surface S
$\int_c \mathbf{F} \cdot \mathbf{dl}$	integral of function $\mathbf{F}$ over path c
$\mathrm{erf}\left(z\right)$	Gaussian function integral from $-\infty$ to z

Abbreviations

CMOS	complementary metal oxide semiconductor
SOI	silicon on insulator (generally silica) layout in silicon photonics
PML	perfectly matched (absorbing) layer
TE	transverse electric field polarization
TM	transverse magnetic field polarization
LP	linear polarization
RF	radio frequencies ($f <\approx 300$GHz)
MoM	method of moments
FEM	finite element method
SEM	scanning electron microscope
FCC	face centered cubic

1 Introduction

Photonics is a set of technologies that focuses on controlling photons on the micro- and nanoscale. The term "photonics" is analogous to electronics where electrons are controlled. Whereas electrons carry electric current, photons carry optical power, such as light. Visible light covers a wide range of wavelengths around 550 nm (or 500 THz). This range extends from 380 nm to 740 nm [2, ch. 52]. However, photonic technology generally utilizes wavelengths in the near infrared. For example, the wavelengths of ≈ 1.3 μm and ≈ 1.55 μm are typically used in photonic applications [3]. Therefore, from now on, the term "light" is used for electromagnetic radiation in the optical regime, which covers both the visible and near infrared wavelengths.

The main benefits of photonics are connected to bandwidths. Wide range of frequencies allows for parallel transmission of data in a single channel. In comparison to RF (radio frequency) technology, much wider bandwidth is available for optical signals. Whereas the finite electron mass limits the oscillation frequency of an electronic circuit, no such limitation exist for electromagnetic radiation created by atomic or molecular transitions.

Silicon photonics denotes photonics made with silicon. The applications in silicon photonics take advantage of the wide bandwidth associated to the optical communication wavelengths and low losses of a silicon waveguide. For example, telecommunication and data processing gain higher speed when signals can be processed over wider bands. Low losses during propagation of a signal allow for more flexible positioning of components and a longer range of communication links. [4] Improved positioning and range can, furthermore, reduce the power consumed by the circuit in operation. For instance, an optical waveguide of 50 μm can achieve a much lower power consumption than an electrical wire of similar length [5].

The major prospects offered by silicon photonics reside in integrated optics, such as optical interconnects (OICs). Development of silicon photonics occurs in the frame set by the manufacturing technology of electronics [6]. Silicon is widely utilized in CMOS (complementary metal oxide semiconductor) technology. The light guiding properties of silicon waveguides allow for manufacturing nanoscale CMOS compatible optical elements. These elements act as fundamental building blocks in integrated circuits. Optical integrated circuits can be used in telecommunications, datacenters, supercomputers or in designing more distributed computer architecture.

Modern optical technology mainly utilizes combined electronic and optical signal processing. Such processing has the benefits described earlier and some additional functions impossible to realize with electronics or photonics alone. Many challenges of the modern technology show that this combination is essential. For example, modern fiber-to-computer links have to convert optical signals into electrical form. As a result, silicon photonics has became a significant topic of research.

From a commercial point of view, several companies have recently started manufacturing or testing simple devices based on silicon photonics. Some examples are

Kotura [7] and Luxtera [8] who have manufactured wavelength division multiplexing (WDM) transceivers and variable optical attenuators, respectively. Optical interconnects have also been tested, and at least Sony and IBM have projects involving them. [9] Other companies interested in silicon photonics can be listed: HP, Intel, ST Microelectronics, Mellanox and ARM have announced their goals concerning photonic technology [10].

Waveguiding technology is a significant part of the commercial photonics. Waveguides are structural building blocks of a photonic circuit or a communication system [11, ch. 2]. They form connections between different systems, chips or components. Filters, resonators, amplifiers or any other type of components are generally constructed to operate at a junction between two waveguides.

Despise high number of applications, silicon photonic circuits generally require an external power source. The material properties of silicon are challenging for construction of power sources, such as lasers utilizing silicon as a gain medium. Therefore, a coupler device is required to feed the power into the chip. Power is generally transmitted through the coupler device into a waveguide.

Many types of coupler devices exist. Common for all these devices is their ability redirect incident light such that it is captured inside the waveguide. The signal is thus converted into a waveguide mode to be processed by the other circuit elements. It is possible to utilize waveguides with varying dimensions, different tapers, prism on the top of a waveguide or a diffraction grating to achieve highly efficient coupling.

This work is mainly focused on the grating couplers. A grating coupler is a periodic array of perturbations in the waveguide refractive index. A typical structure of a photonic grating is an array of shallow etches on the top surface of a photonic waveguide. These etches can deflect the propagation of light by scattering from the refractive index discontinuities. The constructive and destructive interference determine the angles, for which the input signal can be efficiently coupled to the grating. Grating etches resonantly transmit light coming from a certain angle but reject light incident at other angles. The transmission resonance for a given angle of incidence changes with the wavelength because the interference is inherently wavelength dependent. The resonance is also influenced by the grating geometry and can be altered for example by modifying shapes or sizes of the grating elements.

Grating couplers have several benefits from the view point of the silicon photonics. First, flexible placing of couplers on a chip allows for easier construction of photonic circuits. Second, gratings can provide vertical coupling with respect to the chip surface, which is impossible by other means. Third, grating couplers are compact, which supports miniaturization of the circuits. Hence, they override the other coupling techniques in several applications.

This thesis is divided into eight parts. First, the fundamentals of silicon photonics are represented in Chapter 2. After this, Chapter 3 represents the typical waveguide structures in silicon photonics. Basic theory of coupling to a silicon waveguide

is represented in Ch. 4, with several examples of typically used coupler devices. Diffraction gratings are studied in Chapter 5. Therefore, the five first chapters cover the physical phenomenon of coupling through a grating. Chapter 6 describes the numerical basis of the finite element method (FEM) and the simulation methods utilized in this work. The FEM is utilized to optimize the grating geometry with respect to the coupling efficiency. Finally, a comparison of the optimized and initial coupling efficiencies is performed over communication wavelengths around 1.55 μm for TE-polarization (transverse electric field) in Chapter 7. Chapter 8 represents conclusions of the obtained results.

2 Silicon photonics

Silicon photonics denotes silicon based technology, which aims to control light on the micro- and nanoscale. Silicon photonics utilizes many different materials in active and passive components. However, silicon generally enables the operation of those components constructed of other materials. SOI (silicon on insulator) is a subset of silicon photonics with particular importance in this work. SOI technology utilizes silicon components constructed on a SiO_2 layer on a silicon platform. Operation of SOI components is based on high refractive index of silicon on optical communication bands.

2.1 Material properties of silicon

Silicon is a material widely popular in electronics and photonics. In electronics, silicon is used for its low price, strength, adequately wide energy gap, tunable conductivity through doping and ability to form silica (SiO_2) when interacting with oxygen. Silica is suitable for masking of silicon surface in component manufacture. It also has passivating and insulating characteristics, which can protect a silicon chip.

Silicon can be utilized in photonics to avoid compatibility problems with modern electronics. In electronics, manufacturing methods are widely based on CMOS (complementary metal oxide semiconductor) technology. [13, pp. 35-36]. Masking and lithography used in CMOS are developed on silicon properties and allow for dense packaging of integrated circuit elements. Photonic components can be produced by similar means as those used in electronics. Such components are CMOS compatible and combinable with electronic circuits because they utilize similar materials [5].

Silicon is classified as a semiconductor in the period IV of the periodic table. The atomic number of silicon is 14. This leads into an electron configuration of $1s^2 2s^2 2p^6 3s^2 3p^2$, which means silicon has 4 electrons on the outermost electron shell. Semiconducting properties of silicon can be understood through this confinement [12, ch. 12.1]. It follows that silicon creates covalent bonds and tends to organize itself in diamond (double FCC, face centered cubic) lattices. Furthermore, the structure of a silicon lattice creates a band gap between the valence and conduction bands (Fig. 2.1) with only valence band filled at zero temperature. In higher temperatures the valence electrons can be excited to the conduction band inducing conductivity of silicon. [12, ch. 12]

Conductivity has insignificant effect on attenuation on optical bands around 1.55 µm, as mentioned in [5]. This distinguishes silicon photonics from plasmonics, where charge carriers are involved in signal propagation. On other bands, conductivity causes losses during light propagation for charge carriers ability to absorb energy from electromagnetic field.

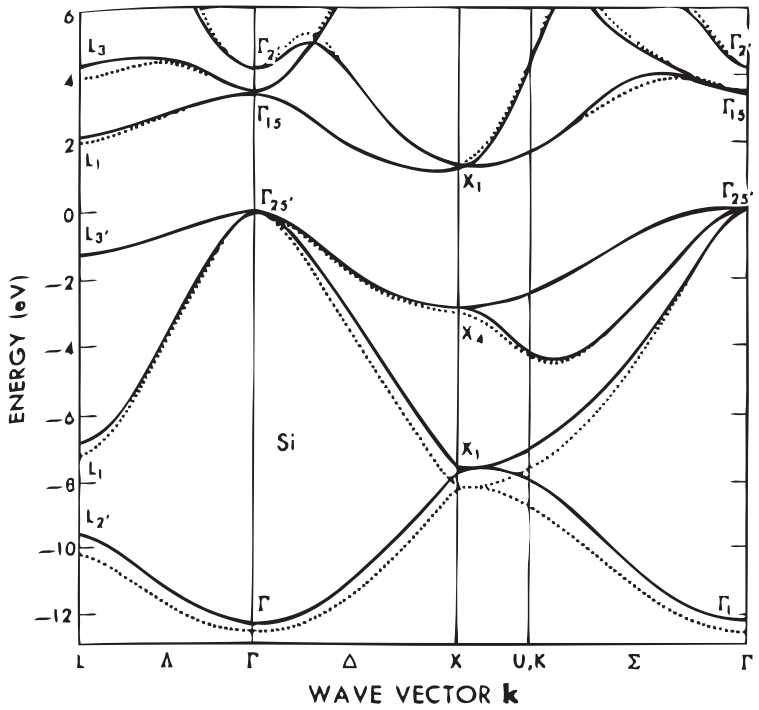

Figure 2.1: Silicon energy band diagram (drawn on a plane of lattice symmetry). Short explanation of the diagram is given in Appendix A. Explained in [12, pp. 421]. Taken from [12, pp. 421].

Light can propagate in silicon with low absorption due to suitable material properties. Energy of a photon can be absorbed directly when the difference between two energy levels in an atomic system corresponds to absorbed light wavelength. Such absorption is behind opaque behaviour of many insulators. Silicon has an indirect bandgap. Photon absorption can occur between the valence- and conduction bands. Generally the energy is transferred between the valence band maximum point and conduction band minimum, which is the so called $k = 0$ point. This rarely occurs in silicon because the points are associated with different wavenumbers. Momentum of the excited particle depends on the wavenumber and should thereby change in the absorption. This would require a change of momentum carried by the absorbed photon. Typically IR (infrared) photons used in photonics have not enough momentum, and described transitions between the two bands are not possible [15, p. 630]. The bandgap of silicon corresponds to 1.12 eV energy and 1.1 µm wavelength [15, p. 636]. However, typically used optical communication wavelengths of 1.3 µm and 1.55 µm lie over 200 nm above this wavelength, the lowest being determined by the optical cable cut off wavelength at 1260 nm [16, p. 133].

Low absorption of silicon allows for construction of light guiding structures without considerable attenuation. High refractive index of silicon enables trapping of light inside the material. The propagating light can reflect totally, for example, due to

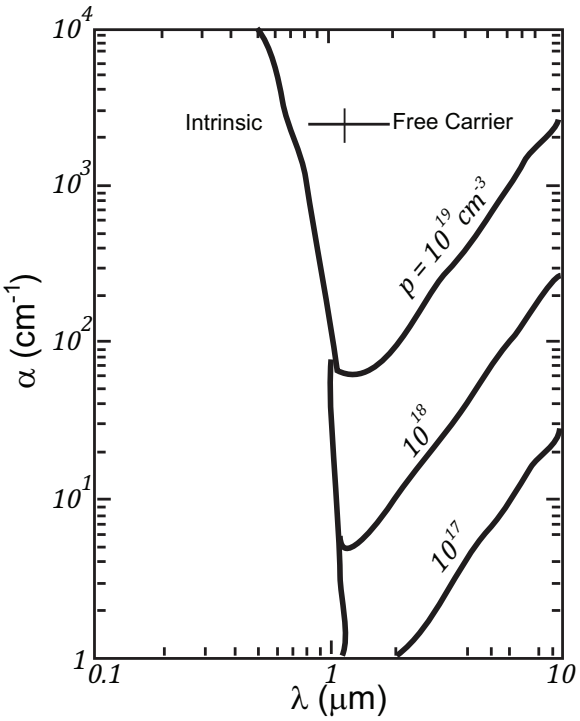

Figure 2.2: Intrinsic and Free Carrier absorption coefficients for silicon. Taken from [14]

.

high refractive index contrast on a silicon-silica boundary. Such contrast is essential on the nanoscale photonics because it allows for construction of tightly bending waveguides with 90° bends and 1 μm bending radius. These waveguides form a prerequisite for dense packaging of components.

Frequency dispersion of silicon has limiting impact on component operation in photonics. Dispersion makes different wavelengths propagate at different group velocities in silicon structures. Problems can arise in optical communication because signal shapes are distorted and inhomogeneous structures can appear different for different wavelengths. The fundamental cause of the dispersion is the wavelength dependent refractive index of silicon, which can be approximated by the Sellmeier's equation [15, p. 180]

$$\epsilon(\lambda) = n^2(\lambda) = 1 + \frac{10.6684\lambda^2}{\lambda^2 - (0.3015\ \ (\mu\text{m}))^2} + \frac{0.0030\lambda^2}{\lambda^2 - (1.3470\ \ (\mu\text{m}))^2} + \frac{1.5413\lambda^2}{\lambda^2 - (1104.0000\ \ (\mu\text{m}))^2} + \ldots \tag{2.1}$$

Sellmeier's equation resembles the Lorentz oscillator model, which states the refractive index originates from charges oscillating in a driving electric field. These oscillations depend on the wavelength in a similar manner as the Sellmeier's relation [17]. However, Sellmeier's equation is an experimental fit, and the wavelengths in the denominators of different terms do not denote physical resonances.

2.2 Typical components in silicon photonics

Silicon photonic systems can be used in signal conversion or routing in communication networks. Components in these systems can be divided to passive and active devices. Active devices include, for example, lasers, amplifiers and modulators. Passive components include waveguides, resonators, and couplers. Light can be confined in subwavelength structures because the silicon index exceeds the surrounding indices by far. This allows downscaling of photonic components and also utilization of nonlinear phenomena that is essential in signal modulation. Hence, circuits in silicon photonics can be constructed in micrometer scale.

Generally, nanophotonic components utilize silicon-silica-silicon (silicon on insulator, SOI) structure. Silicon components are placed on the top of a silica layer, which has typical thickness of ≈ 2 µm. This value can, however, vary between different applications, 2 µm being a standardized value available from the most of the manufacturers [27]. The silica layer covers silicon, which is the host material of the wafer. Bottom silicon has some influence on device operation. However, it has an insignificant effect to the light propagation in structures, which do not emit radiation to their surroundings, and have adequately thick bottom oxide layer. [28], [27]

The simplest photonic circuit element is a waveguide. Waveguides can connect components on a chip or act as building blocks for the other devices (such as resonators or couplers). They steer optical signals in intended direction. These signals are concentrated inside waveguide core due to the high permittivity contrast. A typical realization of a waveguide is composed of a silicon core and a bottom oxide layer, both piled upon each other on silicon substrate. A top oxide cover layer can be used to protect the waveguide and improve the light confinement.

Operation of photonic waveguides is analogous to the waveguides in RF (radio frequency) technology or metal wires in electronics. However, a photonic waveguide carries signals in THz frequencies, which are about three orders of magnitude higher than those used in RF technology. Thus, dimensions of a waveguide are on micrometer scale, which is comparable to a wavelength. Waveguides are treated with more detail in Chapter 3.

Micrometer scale waveguides cannot carry signals over long distances. However, optical signals of these waveguides can also propagate in fibers. Optical fibers can connect distant parts of a photonic system to each other [29, pp. 16]. Typically, photonic technology utilizes single mode fibers that only permit the lowest order

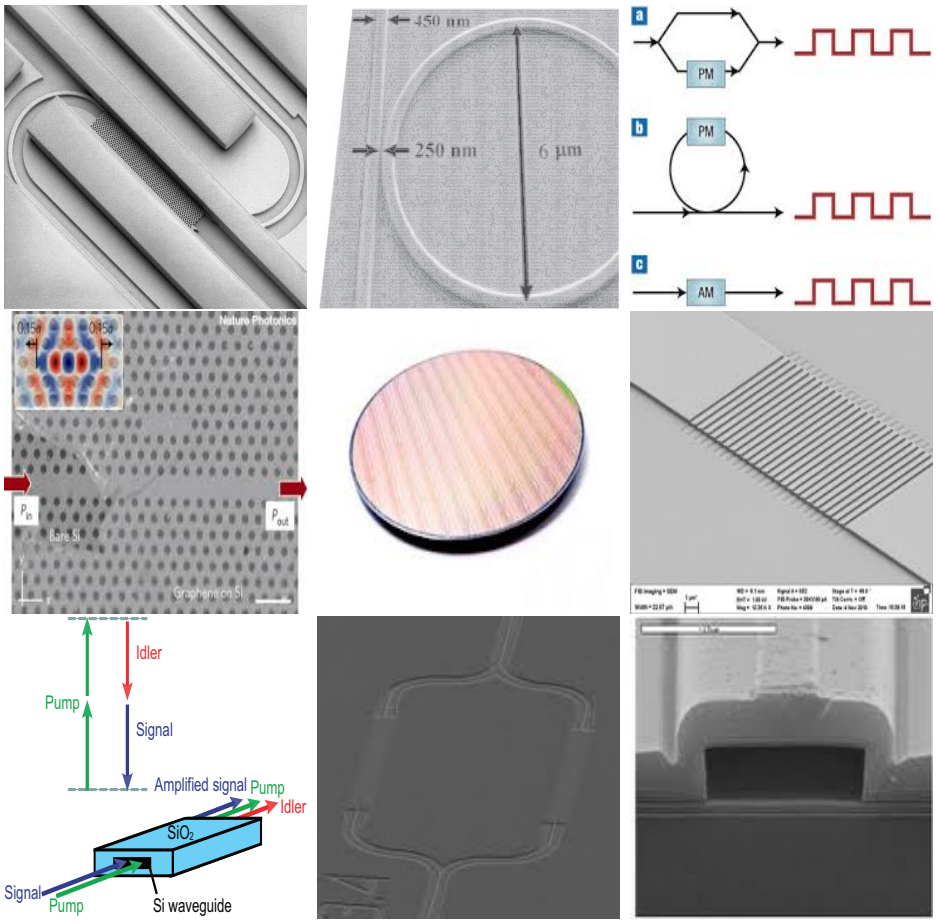

Figure 2.3: Overall picture of typical structures in nanosized silicon photonics. 1st. up: Waveguides and micro-scale structures, taken from [18], 2nd. up: Waveguide ring resonator, taken from [19], 3rd. up: System presentations of different photonic components, taken from [20], 1st middle: Photonic crystal waveguide, taken from [21], 2nd middle: SOI wafer, taken from [22], 3rd middle: grating coupler, taken from [23], 1st down: Mixer device, taken from [24], 2nd down: Mode divider with two T-junctions, taken from [25], 3rd down: Silicon photonic waveguide cross section, taken from [26].

mode to propagate [30, ch. 1.2]. Hence, modal dispersion and additional complexity can be avoided. This requires adequately small fiber core diameter, which is typically ≈ 8 µm for fibers used in photonic applications [31, pp. 77].

Optical fibers generally operate on communication bands around 1.3 µm and 1.55 µm wavelengths, although other bands are also utilized in fiber communication [16]. Photonic devices, which are connected to each other by optical fibers have to share their operation wavelengths. These wavelengths are not suitable for power generation inside silicon, and they set a requirement for external power sources.

Active components in silicon photonics require either strong nonlinearity (high electric field strength) or combination of several materials. Silicon indirect bandgap

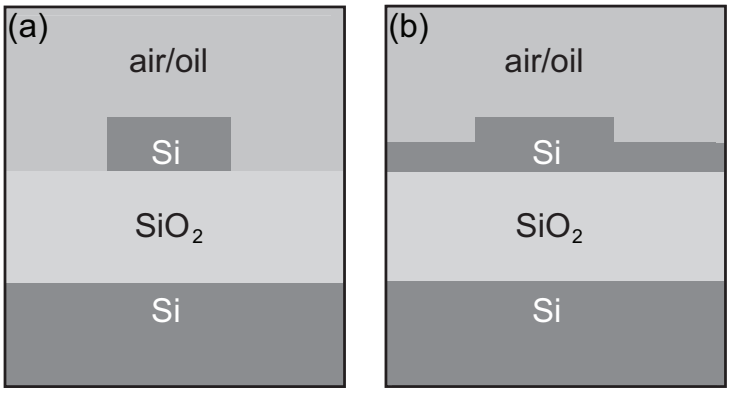

Figure 2.4: Two typically used SOI waveguide types, (a) silicon channel waveguide and (b) silicon rib waveguide. Taken from [15, p. 311].

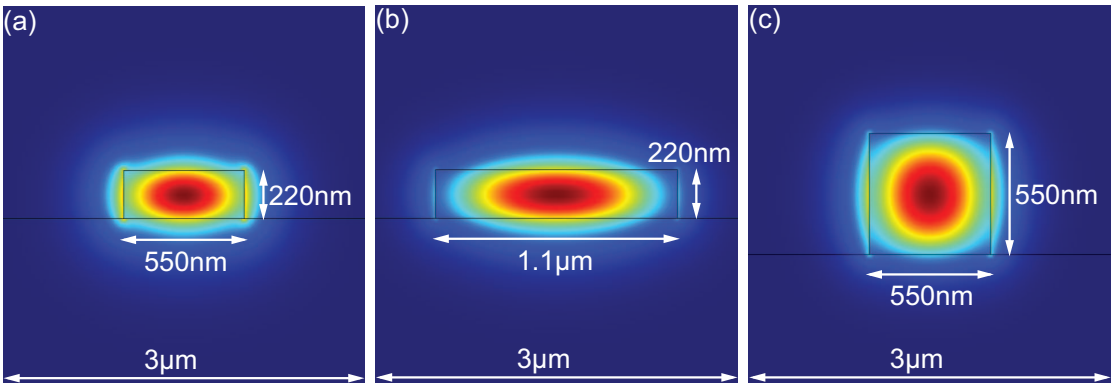

Figure 2.5: Fundamental mode in three different SOI waveguides. Red color denotes the highest field amplitude.

prevents such functions as conventional laser operation or amplification. This is due to hardly achievable population inversion in pure silicon [32]. Generally, other semiconductor materials are utilized, or the active components are placed outside the chip.

Practical issues limit techniques to build lasers or other power sources on silicon platform. One technique utilizes other semiconductors embedded in the silicon chip. Such structures can be composed of GaAs or other direct bandgap semiconductors enclosed in a cavity. Another technique is based on stimulated Raman scattering where intense pump beam excites silicon atoms to the upper vibrational energy levels. Generally Raman lasers cannot be realized without another laser because high pump intensities are required to induce significant scattering. [33] Also more sophisticated techniques exist, which utilize quantum wells or complex atomic transitions to generate the lasing effect [34]. None of these techniques have proven simple and efficient enough to solve the power production problem in silicon. For this reason,

modern photonics prefers external power sources, such as fiber lasers.

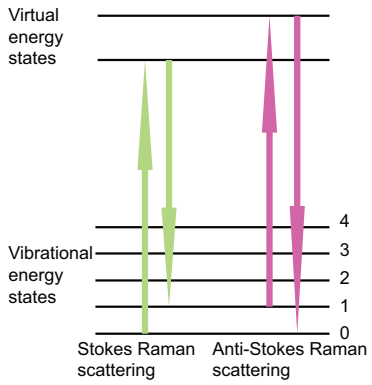

Figure 2.6: Stokes (loss) and Anti-Stokes (gain) versions of Raman shift, which is behind the stimulated Raman scattering. Taken from [35].

Couplers are devices designed to insert external light in the photonic waveguides. A coupler device can guide the power into the chip with an efficiency of nearly 1 [36]. Couplers are essential because power production inside a waveguide is difficult due to the issues, which arise with the active silicon components. Other semiconductors could be used instead of silicon but with the expense that material discontinuities would cause reflections and the overall structure would become more fragile. Therefore, it is preferred to produce optical power outside the crystal. The light encircling in a photonic circuit can originate, for example, from a laser. A more detailed description of couplers is given in Chapter 4.

2.3 Waveguides in silicon photonics

Many different waveguide types exist in silicon photonics. These topologies utilize different materials, as well as different geometries and different physical principles of operation. However, as they are structures of silicon photonics, they all utilize silicon or some chemical mixture of silicon as their building material.

Waveguides in silicon photonics generally utilize silicon oxide, silicon nitride, silicon oxynitride, doped silica, doped silicon, or polysilicon as waveguide materials [31, ch. 6.1]. These materials enable low losses combined with adequately high refractive index contrast to guide optical power. Whereas silica waveguides generally have large dimensions, silicon based waveguides provide a means to realize submicrometer sized structures [31, pp. 30]. Particularly SOI (silicon on insulator) waveguides combine the benefits of low losses (0.1 dB/cm) and small dimensions [31, pp. 30]. SOI waveguides utilize silicon and silica to achieve the required refractive index contrast.

Small dimensions can also be achieved by utilizing multiple reflecting boundaries. Bragg reflector consists of dielectric boundaries, piled upon each other. Adequately many boundaries provide almost perfect reflection, which can be utilized to guide

light [15, ch. 8.4]. Hence, Bragg grating waveguides do not require as strict material selection as conventional silicon waveguides. The idea can be extended further into higher dimensions.

Photonic crystal waveguides utilize multiple reflectors to guide light in two or three dimensional patch. The idea corresponds to the one represented for the Bragg grating waveguides. However, whereas Bragg waveguides have planar geometry, photonic crystals allow compact channel like waveguides where light can travel with low losses. These waveguides can steer the light over sharp (90°) corners without considerable bending losses. [15, pp. 313] The trade off of the improved functionality is more complex manufacture and high prise compared to simpler waveguide geometries.

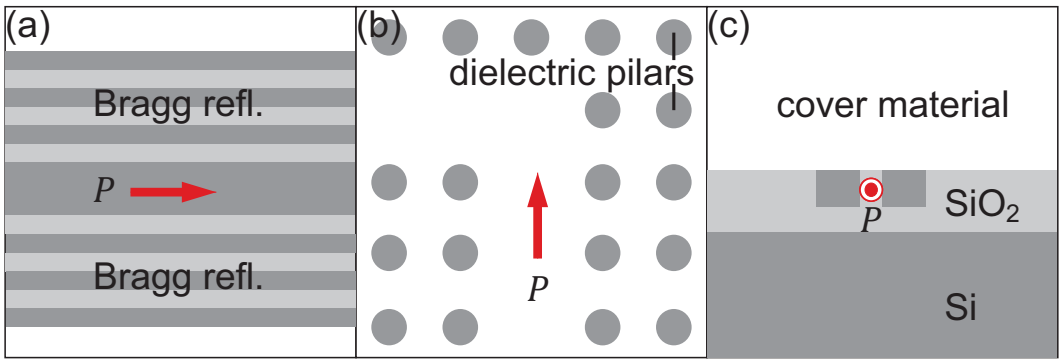

Figure 2.7: Typical waveguides in silicon photonics, (a) Bragg grating waveguide, (b) photonic crystal waveguide, (c) SOI slot waveguide. The channel waveguide is represented in Fig. 2.4.

Slot waveguides realized in SOI technology are an example of a simple waveguide realization. A slot waveguide consists of two silicon slabs set next to each other. Between the slabs, a subwavelength gap is left to guide the optical power. The gap can lie horizontally or vertically between the slabs, which can be placed side-to-side or in a sandwitched structure. The power travels in the gap because the slab index of refraction exceeds the gap index by far. Therefore, total internal reflections can occur inside the slabs. However, the reflected fields have evanescent extensions outside the slabs. These fields overlap and produce high intensity between the slabs. This phenomenon is insensitive to the wavelength. [1, ch. 2.1.2]

Channel waveguides have highest field strength inside the silicon. Therefore, power propagates in a channel, which can be placed on the top of a dielectric layer. However, it is also possible to embed the channel inside the silica or to cover the whole silica layer with silicon. The fundamental principle of operation is the same for slot waveguides and channel waveguides. In channel waveguides, only one evanescent field extension exist, and no overlap is produced with an other field. Therefore, the field obtains the highest value inside the waveguide core. [31, pp. 30], [15, pp. 310]

3 Silicon waveguidess

Guided propagation of light forms an essential requirement for photonic applications. A light pulse in homogeneous space diverges and experiences reformation after being generated by a light source. This limits the use of free light in data applications because diverging pulses can mix to each other, their paths of propagation are straight lines or difficult to control, and power is lost while the pulse propagates. [37, 38] Free space optical communication offers some benefits not achievable through guided technology. Such benefits include multiport systems and flexible component placement. However, utilizing waveguides has advantages, which make them necessary in many applications. Guided optics preserves pulse power and reduces interference of different signals. It also avoids beam direction issues and enables use of nonlinearity in signal manipulation. The simplest waveguide is composed of two mirrors put opposite to each other [15, ch. 8.1].

3.1 Channel waveguides in silicon photonics

Many different waveguide structures have applications in silicon photonics. Common for most of them is a waveguiding layer composed of silicon, set on top of a dielectric layer above the host silicon lattice. This layer can be horizontally wide or restricted in two dimensions. Such layer is the central part of silicon nanowires and silicon rib-waveguides (Fig. 2.4).

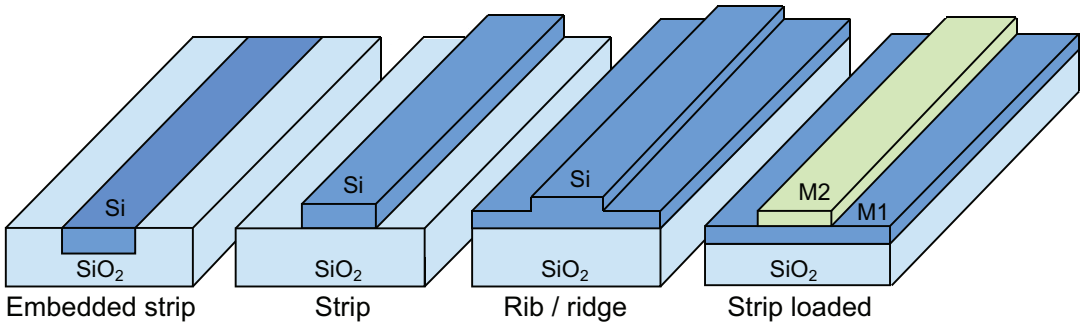

Figure 3.1: Different channel waveguide geometries. In the rightmost figure, the materials M1 and M2 can be, for example, silicon and doped silicon respectively. Taken from [15, p. 310].

Channel waveguides are composed of a high refractive index channel surrounded by materials of lower indices. High refractive index contrast makes light well confined in the channel part of the waveguide. A 2D structure can squeeze light into subwavelength dimensions in two perpendicular directions. This allows for dense packaging of components on a chip. In some aspects, channel waveguides resemble

microstrips used in RF (radio frequency) technology. However, significant differences in field distributions exist compared to microstrips. In microstrips electric field is confined between a metallic wire and bottom material [39, ch. 5] whereas photonic waveguides confine the fields in the channel.

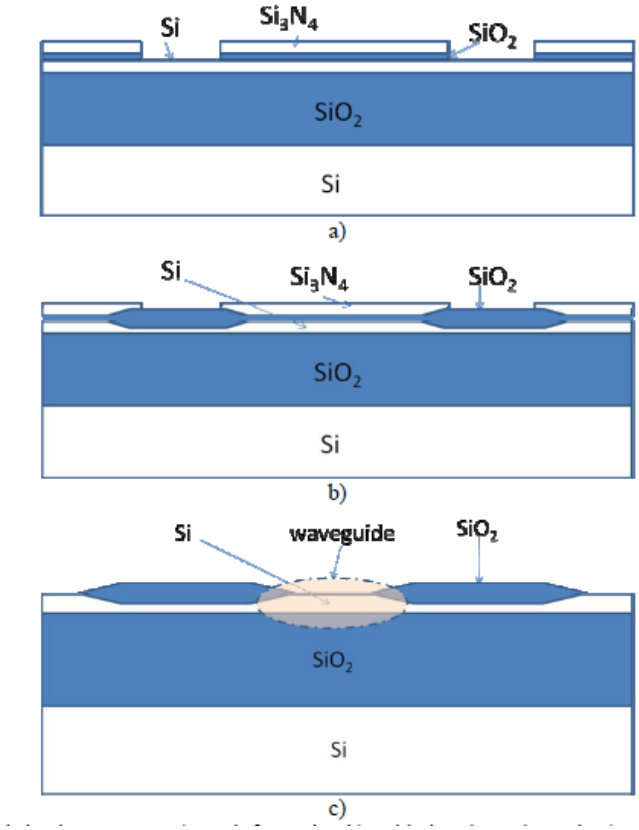

Figure 3.2: Fabrication of a rib type waveguide by LOCOS (local oxidation of silicon) technique, a) mask formation, b) oxidation, c) mask removal. The figure shows the two last phases of the manufacturing process. Taken from [40].

Field propagation in the waveguide can be understood as propagation of multiple planewaves bouncing between four boundaries framing the waveguide domain. Each wave has evanescent extension outside the waveguide as a result of total internal reflection. Superposition of these waves forms a mode of the waveguide. [15, ch. 8.3]

Channel waveguides can be manufactured by CMOS (complementary metal oxide semiconductor) technology. For example, a rib type waveguide is created when following steps are performed: (1) exposing a silicon wafer to oxygen, which causes reaction producing the silica layer, (2) growing additional silicon on the silica layer, (3) growing an additional silica layer, (4) covering the whole structure with photoresist, (5) utilizing suitable radiation with designed mask to break the photoresist in selected regions, (6) etching the resist and the silica from the surface, which does not cover the waveguide channel, (7) converting the silicon into silica through oxidization on these areas, and (8) removing the resist. [13, ch. 13], [40] This process is

completely compatible with CMOS technology. The achieved accuracy depends on the lithography with proportionality to the used wavelength. Therefore, nanoscale manufacturing becomes possible, as the wavelength used in lithography can be several nanometers long.

Planar (slab) waveguide is an useful simplification of a channel waveguide. Planar waveguides extend over an infinite planar surface. In practice, waveguide cannot have infinite dimensions or an ideally planar geometry. A planar waveguide is an excellent approximation if one of the waveguide dimensions is significantly larger than the others. In such structure, borders of the waveguide only have influence near them leading into planar waveguide modes in the centermost parts of the waveguide. Therefore, the waveguide can be modeled by its longitudinal cross section, which contains all the information about the waveguide geometry. The approximation is valid, for example, when waveguide width extends 12 μm in horizontal direction and the waveguiding layer has thickness of 220 nm.

Several applications have emerged around nearly planar waveguides. Some examples are liquid crystal waveguides [41] and slab-coupled waveguide lasers [42]. More importantly, planar waveguides have been utilized in couplers [43] and sensor applications [44]. In both cases, waveguide dimensions have to be matched to ones of the environment. This requirement can arise from the need to couple light to an optical fiber or to measure some external quantity. Such characteristics are related to high top surface area, which is typical for nearly planar waveguides.

3.2 Physics of nearly planar waveguides

The waveguides studied in this work have large width compared to height and can therefore be considered as planar structures [45]. A detailed mathematical description of planar waveguides is given in this section. Such description includes propagation and shape of electric fields in these waveguides.

The material above a planar waveguide is generally called the cover and the one below is called the cladding of the waveguide. For a planar waveguide, refractive index has to be higher in the waveguiding layer than in the surrounding media. Therefore, the cover and the cladding materials can have any indices between 1 (free space) and waveguiding layer index. Here, only the simplest structure is described, with equal indices for the surrounding materials. Equal indices correspond to some waveguide structures studied in this work.

Full mathematical description of a planar waveguide requires study of both polarizations with respect to all waveguide boundaries. Such study would be necessary to form the field expressions for the TE (transverse electric field) and TM (transverse magnetic field) modes of the waveguide. Considering both polarization is possible but gives no additional insight to one offered by analysis of TE polarization. Thus, simplified mathematical analysis is represented here for TE polarization, with the

notion that similar treatment can also offer the solution of the TM modes of the waveguide.

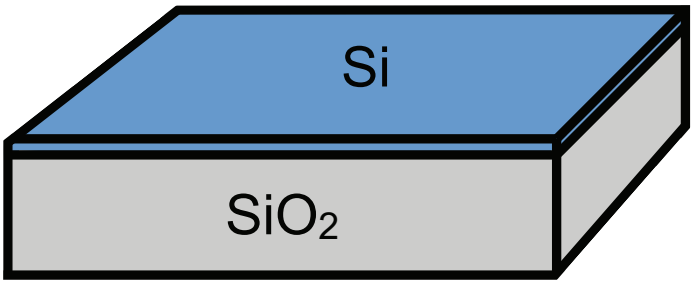

Figure 3.3: Planar "slab" waveguide. Taken from [46].

Operation of a planar waveguide can be understood through reflecting waves obeying Helmholtz equation. These waves have unique propagation direction and they behave as single rays of light, which interfere with each other. For each wave, reflections occur between the cover and cladding interfaces. The angle of reflection can exceed the critical angle that results in a zero leakage out of the waveguide. Reflecting plane waves can propagate along the waveguide simultaneously generating the waveguide modes as a superposition of the single wave fields. Such superposition carries finite amount of energy and is equal to a Fourier series presentation of a periodic mode in the waveguide. Thus, slightly unphysical concept of a plane wave can be applied to describe angular frequency components of a waveguide mode.

Plane wave description can also be applied to two dimensional channel waveguides. However, such treatment becomes complex because reflections of propagating light can occur in vertical and horizontal planes, and also between two perpendicular waveguide boundaries. Therefore, only ideally planar structure is considered here. Following is based on Chapter 8 in [15].

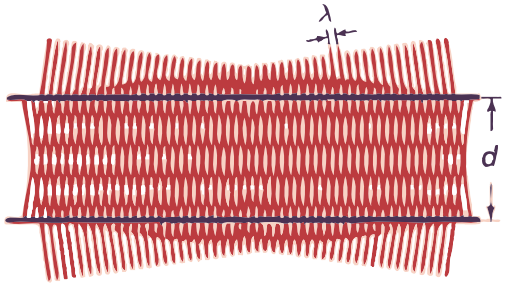

Figure 3.4: Interference of two plane waves in a slab waveguide. Taken from [15, p. 292]

A plane wave is described by a complex number representation [47, ch. 2]

$$\mathbf{E} = \mathbf{u} E e^{i\left(\omega t - \mathbf{k}\cdot\mathbf{r}\right)}, \tag{3.1}$$

where unit vector $\mathbf{u}$ describes the polarization of the plane wave. A plane wave defined by Eq. (3.1) propagates in $\mathbf{k}$ direction with phase velocity of $v_p = \omega/k$. In a photonic slab waveguide, two plane waves exist simultaneously with opposite propagation perpendicular to the waveguide plane (original and reflected waves). The total electric field in the waveguide forms as the superposition of these plane waves (Fig. 3.4). For x directed TE polarization

$$\mathbf{E} = \hat{\mathbf{x}}\left[E_+ e^{-i\left(kz\cos\theta + ky\sin\theta\right)} + E_- e^{-i\left(kz\cos\theta - ky\sin\theta\right)}\right], \tag{3.2}$$

where θ is the complement of the angle of reflection. This expression describes a waveguide mode if the reflected field E_- reproduces the original field after two reflections. Each reflection causes a phase shift -ϕ, which affects the reflected field phase. Therefore

$$E_- = E_+ e^{-i\phi}. \tag{3.3}$$

The reflected field equals the original if the fields have similar phases after two reflections, or formally

$$\begin{aligned} kd\sin\theta &= -kd\sin\theta + 2\phi + m2\pi \\ 2kd\sin\theta &= 2\phi + m2\pi, \end{aligned} \tag{3.4}$$

where d denotes the waveguide height. This equals both waves moving distance d perpendicular to the waveguide plane with unaltered phase of the superposition. Different angles θ require different numbers m to fulfill equation 3.4. This lead into quantized values of θ because the change in the phase during the translation depends on the propagation direction. Equation 3.4 cannot be solved analytically because generally the phase change in reflection, ϕ, depends on the angle θ. The dependency follows from Fresnel reflection coefficient, which are functions of θ. These coefficients can be written as

$$R = \frac{n_1\sin\theta_1 - n_2\sin\theta_2}{n_1\sin\theta_1 + n_2\sin\theta_2}. \tag{3.5}$$

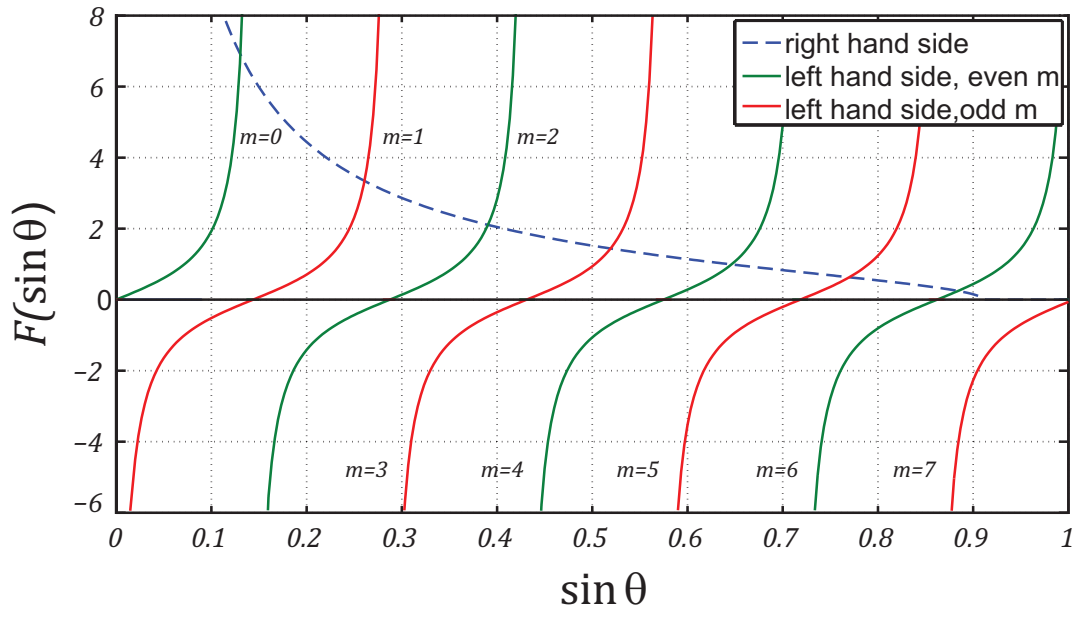

Figure 3.5: Solution of Equation (3.14) when $\lambda_0 = 1.55$ μm and $d = \lambda_0$. Indices n_1 and n_2 are 3.48 and 1.44 respectively.

Equation (3.5) transforms into a complex number when it is written as a function of $\theta_1 = \theta$ and θ approaches 0. The nominator can be written as

$$n_1 \sin\theta - n_2\sqrt{1 - \cos^2\theta_2}. \tag{3.6}$$

Snell's law can be utilized for the complement angles to write the equation as

$$n_1 \sin\theta - n_2\sqrt{1 - \frac{n_1^2}{n_2^2}\cos^2\theta} = n_1 \sin\theta - n_2\sqrt{1 - \frac{n_1^2}{n_2^2} + \frac{n_1^2}{n_2^2}\sin^2\theta}, \tag{3.7}$$

which equals to

$$n_1 \sin\theta - n_2\sqrt{\frac{n_1^2}{n_2^2}\left(\frac{n_2^2}{n_1^2} - 1 + \sin^2\theta\right)} = n_1 \sin\theta - in_1\sqrt{1 - \frac{n_2^2}{n_1^2} - \sin^2\theta}. \tag{3.8}$$

Taking $n_1 \sin^2\theta$ as a common factor gives

$$n_1 \sin\theta \left[1 - i\sqrt{\left(1 - \frac{n_2^2}{n_1^2}\right) / \sin^2\theta - 1}\right], \tag{3.9}$$

which is the same as

$$n_1 \sin\theta \left[1 - i\sqrt{\frac{\sin^2\theta_c}{\sin^2\theta} - 1}\right], \tag{3.10}$$

where θ_c is the complement of the critical angle of reflection on the waveguide boundary. Therefore, the equation obtains phase value -ϕ, which can be determined by summing the phases of the nominator and denominator of the expression. These phases have equal magnitude and the overall phase becomes two times the nominator phase value. This phase is given by equation

$$\tan\frac{\phi}{2} = \sqrt{\frac{\sin^2\theta_c}{\sin^2\theta} - 1}, \tag{3.11}$$

Combining Equation (3.11) with the self consistency condition (3.4) gives

$$\phi = kd\sin\theta - m\pi = 2\arctan\sqrt{\frac{\sin^2\theta_c}{\sin^2\theta} - 1}. \tag{3.12}$$

The equation can be simplified furthermore:

$$\frac{kd\sin\theta}{2} - \frac{m\pi}{2} = \arctan\sqrt{\frac{\sin^2\theta_c}{\sin^2\theta} - 1}, \tag{3.13}$$

which is a transcendental equation:

$$\tan\left(\frac{kd\sin\theta}{2} - \frac{m\pi}{2}\right) = \sqrt{\frac{\sin^2\theta_c}{\sin^2\theta} - 1}. \tag{3.14}$$

Numerical solution of the equation (3.14) yields a discrete set of angles θ. These angles can be determined drawing the right and left sides of Equation (3.14) and searching the crossing points of two curves for each m (Fig. 3.5). It follows that in an adequately narrow waveguide, only one angle is found, resulting in single mode operation. Such crossing points correspond to different waveguide modes with different field patterns calculated from (3.2). As shown in Fig. 3.6, different bounce angles lead into different number of nodes on the waveguide cross section. Each waveguide mode has then unique field pattern, which is observed in the output.

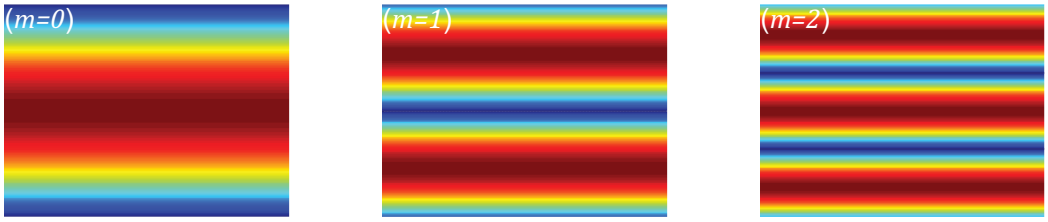

Figure 3.6: Simulated three first modes of a slab waveguide. Red color denotes the highest field amplitude. The plots correspond to free space wavelength of 1.55 µm and waveguide thickness equal to wavelength. The indices n_1 and n_2 are 3.48 and 1.44 respectively.

Equation (3.2) gives additional information about the field amplitudes. The amplitudes E_+ and E_- have remained unspecified until now. These amplitudes can be any real quantities without alterations to the self consistency condition (3.4). Therefore, E_- can have equal or opposite sign with respect to E_+. Symmetry guarantees that the absolute values $|E_+|$ and $|E_-|$ match to each other. Otherwise, the superposition of the fields would propagate in y direction inside the waveguide (an illuminating ray through the waveguide would exist).

Signs and magnitudes combined, the Expression (3.2) results in "even" and "odd" modes. Even modes are those where the plane wave components have equal sign and odd modes are those where the signs are different. The nature of modes depends on the field confinement in the waveguide. To achieve maximum confinement, the fields have to interfere constructively in the middle of the waveguide. Thus, even values of m associate to the even modes and odd values associate to the odd modes.

Field equations of a planar waveguide are obtained as sums of the plane wave fields. These plane waves become evanescent because they reflect totally from the waveguide boundaries. Combining the field equations inside and outside the waveguide gives cosine function inside the waveguide and exponential function outside the waveguide. [15, ch. 8.2] Hence, the electric field has a following piecewise expression [15, ch. 8.2]:

$$\begin{array}{lll} \mathbf{E}\,(x,y) \quad = & & \\ \hat{\mathbf{x}} E_{0i} \cos\left(ky \sin\theta_m\right) & m \text{ even}, & |y| < d/2 \\ \hat{\mathbf{x}} E_{0i} \sin\left(ky \sin\theta_m\right) & m \text{ odd}, & |y| < d/2 \\ \hat{\mathbf{x}} E_{0o} \exp\left(\gamma_m \left[y + d/2\right]\right) & & y < -d/2 \\ \hat{\mathbf{x}} E_{0o} \exp\left(-\gamma_m \left[y - d/2\right]\right) & & y > d/2 \end{array} \quad . \tag{3.15}$$

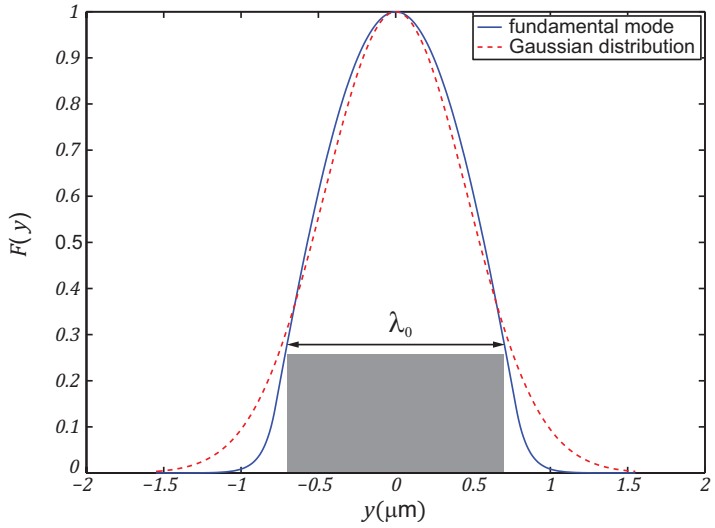

Figure 3.7: Fundamental mode of a slab waveguide and a Gaussian distribution. The used waveguide dimensions and excitation parameters correspond to the ones used in Fig. 2.5*a*.

Equation (3.15) satisfies electric boundary conditions. These conditions require electric field tangential component to be continuous across waveguide boundaries. TE polarized plane waves only have a tangential component, and they satisfy the boundary conditions for a continuous total field. In contrast, electric flux density only has a condition for the normal component continuity. This condition is automatically satisfied for the zero amplitude normal components on the both sides of the boundary.

The plane wave picture offers important insight to several loss mechanisms present in the realistic waveguides. Losses can arise from variable refractive index. Any deflections from uniform index can cause scattering, which transforms a part of the propagating mode into light propagating in multiple directions. For this light, angles of reflection can become clearly smaller than the critical angle. This enables scattered light to escape from the waveguide. Another example is the influence of

surface roughness on waveguide properties. Surface roughness can cause scattering similar to the refractive index imperfections. The scattering, however, becomes stronger for the higher order modes because the angle of reflection is smaller for them. Higher order modes have greater number of reflections in particular length of the waveguide than lower order modes. Therefore, they "touch" the surface many times more compared to the light that travel directly through the waveguide. Each "touch" with a rough surface causes scattering and leakage out of the waveguide. This can be utilized, for example, in grating couplers. Couplers utilize an altered surface structure to guide power into or out of a waveguide (Fig. 3.8).

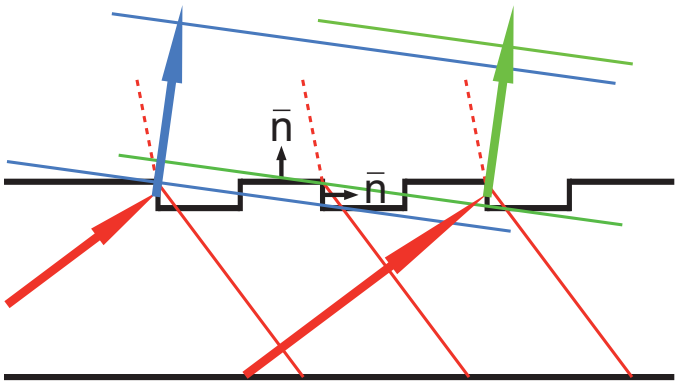

Figure 3.8: Scattering by a grating. The image is a simplification but can be used to visualize surface scattering.

4 Coupling to silicon waveguides

Coupler devices have been developed to overcome challenges in power injection to waveguides in silicon photonics. Challenges in the coupling arise from the small size and high refractive index of silicon waveguides. These waveguide characteristics cause undesirable losses in coupling. To avoid losses, special coupler devices have been developed. These devices realize matching between the waveguide and the power source and transmit power to the silicon photonic circuits. [1, ch. 1.2]

4.1 Theory of coupling

An efficient coupler device has to overcome several limiting processes to achieve maximal coupling. These processes inhibit transfer of power between the source and the waveguide. Coupling losses can arise from, for example, reflections in dielectric boundaries, different sizes and shapes of the fields, waveguide scattering, or back coupling. Some of these phenomena can be combined into single processes, which enables writing the following equation:

$$P_{cpl}\left(dB\right) = P_{in}\left(dB\right) - \Gamma\left(dB\right) - 10\log\left(1 - |R|^2\right), \tag{4.1}$$

where Γ denotes losses due to electric field mismatch and $1 - |R|^2$ term takes into account the losses due to reflections [1, pp. 22]. Mismatch term Γ contains both the loss due to mismatch in field dimensions and in the shapes of the fields.

Field mismatch Γ can be calculated utilizing coupled wave theory of silicon waveguides. The theory is represented in [30, pp. 172], and in [48], and is therefore omitted. The resulting value of Γ depends on the overlap of the incident source field and the excited mode of the waveguide. Such overlap is determined by an integral

$$\Gamma \sim \left| \int_S \int \mathbf{E}_{input} \times \mathbf{H}^*_{mode} \cdot \mathbf{dS} \right|^2. \tag{4.2}$$

This integral can be simplified and normalized to a maximum value of 1. Such treatment yields the actual expression for Γ:

$$\Gamma = \left| \int_{-\infty}^{\infty} \int_{-\infty}^{\infty} |E_{input}|\,|E_{mode}|\,\mathrm{d}x\ \mathrm{d}y \right|^2, \tag{4.3}$$

where E_{input} and E_{mode} fields are normalized as

$$\int_{-\infty}^{\infty}\int_{-\infty}^{\infty} |E_{input}|^2 \, \mathrm{d}x \; \mathrm{d}y = 1. \tag{4.4}$$

Equation (4.3) shows that the incident field and the excited mode have to have similar electric field strengths on the coupling boundary, where the integrals are evaluated. Equality of field profiles maximize the overlap of the fields. This overlap is shown in Fig. 4.1.

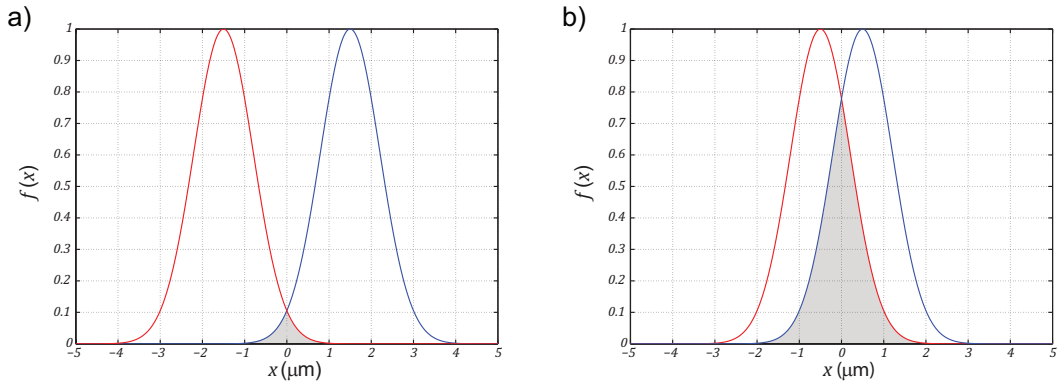

Figure 4.1: Overlap of two Gaussian functions. A) small overlap, b) significant overlap.

Figure 4.1 demonstrates that losses due to electric field mismatch can arise for several reasons. First, fields that have different size have small overlap relative to the larger field. Spatially wide input beam can only couple a low fraction of power into a mode, which has considerably smaller spatial confinement. This situation occurs when power is coupled between a single mode fiber and a nanophotonic waveguide. Commercial fibers have a mode field diameter (MFD) of ~ 10 μm whereas thickness of a waveguide can be several hundreds of nanometers. Second, fields with different profiles cannot have a large overlap. Therefore, any deviation of the rightmost curve in Fig 4.1 from a Gaussian shape would cause coupling losses if the functions were the field profiles in Eq. (4.3). Third, field phases have to match each other.

Phase matching has the greatest importance in transverse direction. In other words, an excitation, which is incident to the coupler in an angle, may have perfectly matched field profile. However, the wavefront associated to this profile approaches the coupling boundary in an angle, which results in a delay between different parts of a wavefront. Therefore, the field profile apparent to the coupler has a distorted shape. This can be avoided if the advancing wavefront of the excitation reaches the coupling boundary without delay. Hence, the coupling boundary has to lie on a surface, where the excitation has uniform phase.

Equation (4.1) also has the reflection term, which describes additional losses. Any dielectric boundary, or conversion of mode propagation constants, causes reflection according to Fresnel's coefficients. These coefficients can be written as

$$R = \frac{n_{eff1} - n_{eff2}}{n_{eff1} + n_{eff2}} \tag{4.5}$$

$$T = 1 + R, \tag{4.6}$$

where R describes reflection, T describes transmission, and n_{effi} are the effective refractive indices of two modes, defined as $\beta_i = k_0 n_{effi}$. Modal conversion is always present when coupling to a nanophotonic silicon waveguide. Therefore, the effective index difference in (4.5) cannot be 0. Reflection occur, for example, between cover, cladding, waveguide core, and fiber boundaried.

Generally power is coupled into and out of a silicon chip by optical fibers. In such case, any coupling loss is doubled. This simplification arises from the reciprocity of coupler devices. In addition, waveguide losses have to be taken into account. The result of this analysis is the equation for overall loss:

$$P_{cpl}\,(dB) = P_{in}\,(dB) - L_{cpl,in} - L_{cpl,out} - \alpha L, \tag{4.7}$$

where alpha is the attenuation coefficient, and L is the length of the waveguide [1, pp. 21].

4.2 Coupler devices

Modern techniques have achieved coupling of almost 100 % efficiency [49]. Typical efficiencies are lower with simpler manufacture of coupler devices. However, efficiencies have been improving for these devices by far. These improvements are based on shrinking of the incident beam size and matching of the output to the waveguide mode.

A prism can focus and reshape the incident light couple it to a waveguide. The prism can be set, for example, above a nearly planar waveguide or a thin semiconductor layer. The waveguide surface and the prism cannot touch each other, but rather there is a gap between them. Such gap is essential because the technique is based on refractive index differences between four materials. Prism, gap, waveguide and cladding indices have the following dependencies: $n_{prism} > n_{waveguide} > n_{cladding} > n_{gap}$. [1, pp. 26]

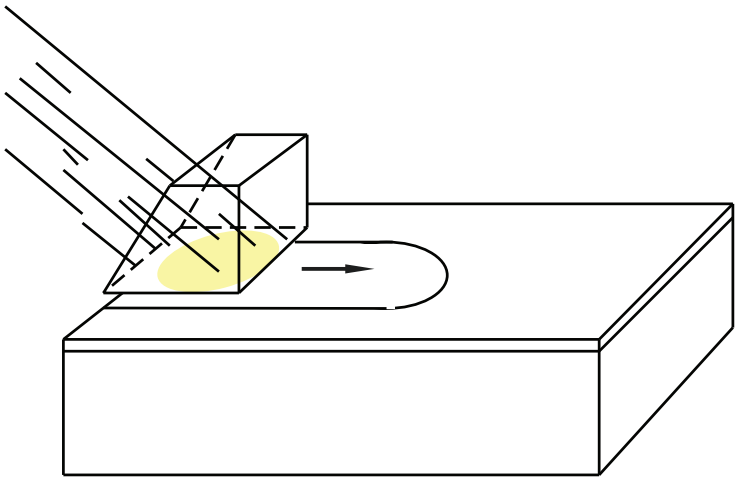

Figure 4.2: Prism coupler device. Taken from [50]

Prism couplers utilize total internal reflection on the prism-gap boundary inside the prism. Such reflection is possible because the prism has a higher refractive index than the gap material. Totally reflected waves have an evanescent (attenuating) extension on the other side of the boundary compared to the side of reflection. Evanescent waves propagate in the direction of the boundary. Therefore, their direction of propagation corresponds to the propagation of waveguide modes. This enables the coupling to the waveguide when the phases of the evanescent waves travel with similar speed to the waveguide modes. This condition is only satisfied on a certain frequency band for each angle of incidence, and prism coupling shows resonant behaviour. [51]

Majority of modern couplers do not utilize the prism technique. The idea of utilizing prism has roots in the late 60s. At that time, 50 % of the incident power could be coupled in semiconductor films [51]. Later, few publications have been made, partially because coupling to rib type waveguides causes high losses [52]. These losses are accompanied with a risk of damaging the waveguide surface and practical difficulties of realizing refractive index higher than the index of silicon [1, pp. 26].

Prism couplers are suitable for some special applications. In [53], a prism was utilized to insert 75 % of the incident power in a silicon square cavity, which somehow resembles coupling to a waveguide. In addition, prism couplers have been utilized in sensor applications, where coupling to the waveguide modes depends on the cover material. The couplings shows as dips in the reflectance spectrum of the coupler [54]. These dips can be utilized in characterizing the surrounding materials.

Different tapers are alternatives of the prism couplers. They are waveguide sections, expanding towards the input dimensions with adequately smooth space, leading to $\sim$ 1000 µm length of an adiabatic taper structure [1, pp. 29]. Tapers can also become narrower towards the input, which is the case in the inverse taper structures. The end point of an inverse taper can be several tens of nanometers thin [55].

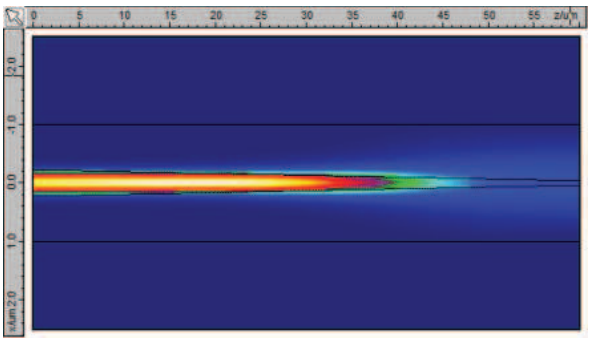

Figure 4.3: Simulated field distribution in an inverse tapered waveguide. Taken from [56]

Tapers utilize the gradual change of the effective refractive index experienced by the input beam. The gradual change guarantees that no considerable reflection occur and the incident beam is slowly adapted to the waveguide [57]. Change in the refractive index is tolerant to changes in the wavelength, which results in high coupling efficiency over broad bandwidth [57], [1, pp. 31].

Tapers have utilized in silicon photonic couplers. These couplers mainly utilize inverse tapering structures because broadening of a silicon waveguide is difficult in two directions. However, two stage tapers can avoid these fabrication difficulties by using two piled layers, which both are tapered in horizontal direction [57]. Generally single layer tapers do not achieve high coupling efficiencies [1, pp. 28].

Inverse tapers offer benefits over those achievable by conventional taper structures. Inverse tapers have been demonstrated to achieve losses below 1 dB [1, pp. 29]. Inverse technique can also reduce the length of the taper to 200 µm [1, pp. 29]. In 2003, it was demonstrated that a parabolic shaped inverse transition could achieve low losses of 3.3 dB with only 40 µm length. The fraction of mode mismatch was only 0.25 dB of the losses. The short length of the taper a significant improvement in inverse taper technology because one limiting factor of the tapers in miniaturized circuits is their length. [58]

Grating couplers can solve the problems of coupler length and restrictions in position. They are compact, generally 12 µm x 12 µm sized devices, which can be located in any part of a circuit [1, ch. 3.5], [59]. Coupling in these devices is achieved through diffraction, which arises from light interacting with periodic alterations of the waveguide surface (diffraction grating).

Diffraction can change propagation direction of incident light. Therefore, light in a grating coupler can turn in an angle that corresponds to one of the waveguide modes to be excited. Formally, this change of propagation is described by matching the phases of the incident radiation and the waveguide mode. The requirement for the

phase matching sets a condition for the grating dimensions. This condition turns into the strong frequency dependence [1, pp. 31] of grating couplers, because light diffracted from all grating elements have to be matched to the waveguide mode. [60]

Narrow bandwidth, back coupling and reflections are limiting factors of the grating couplers. Particularly, a grating acts as surface roughness in the waveguide. Therefore, light can leave the grating in many directions. In SOI (silicon on insulator) structure, down scattered light can interfere with the waveguide light, which leads to a dependency of the coupling efficiency from the bottom oxide thickness [49]. Coupled light can also reflect from the grating and be scattered back out of the waveguide [1, pp. 31]. Furthermore, grating operation is limited by strong polarization dependence, complex fabrication and requirements for precise alignment for coupling. However, these limitations can be avoided by optimizing the grating structure.

Grating couplers have achieved coupling efficiencies of over 50 % of the incident power. Efficiencies as high as 80 % can be achieved by alteration of the cover medium, bottom oxide thickness, and the element shapes, and utilizing a bottom reflector beneath the grating. Some of the achieved coupling figures are gathered in Table 4.1:

Table 4.1: Coupling efficiencies reported in several articles. The values are for uniform geometries.

Configuration	Coupling (%)	Ref.
No additional techniques	37	[49]
Index matching oil	44	[49]
Optimized bottom oxide (silica) layer	53	[49]
Bottom reflector	79	[49]
Perfect optimization	80	[61], [62]
Fully etched grooves	49	[?]

5 Grating theory

Diffraction gratings are utilized to deflect light propagation and to divide light in spectral components. The deflecting property of a grating can be utilized to guide light in various structures. The periodic nature of a grating allows for changing the propagation direction in angles unreachable for ordinary reflection and refraction.

5.1 Diffraction theory

Diffraction in wave optics denotes bending of waves when passing obstacles, which can change the propagating intensity distribution. Generally diffraction occurs when an aperture is illuminated by a light source. An interference pattern appears on the back side of the aperture in such an experiment [63, ch. 10].

Diffraction is not equivalent to scattering. Scattering denotes deviations of the wave propagation from direct propagation caused by localized non-uniformities in the propagation medium. A huge obstacle compared to the wavelength can bend light through diffraction but does not necessarily scatter the light. However, these definitions partially overlap when talking about diffraction gratings where light is deviated by small non-uniformities in refractive index. These non-uniformities can extend tens of wavelengths in one direction and be subwavelength long in the other direction (for example, a DVD-disc). Here, the deviations can be thought to scatter light whereas one could also speak about diffraction. Hence, term scattering is used in this work when describing these gratings. This is consistent with some literature about the gratings [64].

Diffracted fields can be represented as a superposition of plane waves propagating in different directions. This representation is called angular spectrum [65, ch. 2]. Angular spectrum representation explains diffraction because obstacles limit the propagation of the plane wave components. Obstacles alter the spectrum of the fields causing interference of the remaining components on the other side of the obstacle [66, ch. 2]. Hence, interference and diffraction are closely related to each other [67, ch. 30].

Similar interpretation is obtained through Kirchoff's formulation. This formulation states that the interference pattern observed on the back side of the aperture originates from secondary emitters in the aperture surface. This is equivalent to the Huygens principle where each point in a wave front is thought to emit a spherical wave [68, ch. 7.2-7.4]. These waves can interfere beyond the aperture forming a pattern.

Formally, the diffracted field u for any type of wave motion can be calculated from

the Fresnel-Kirchoff diffraction integral [63, ch. 10]:

$$u(\mathbf{r}) = u_0 \frac{i}{\lambda} \int_{S_a} \frac{e^{-ik(\rho+r)}}{\rho r} \frac{\cos(\hat{\mathbf{n}} \cdot \hat{\mathbf{r}}) - \cos(\hat{\mathbf{n}} \cdot \hat{\rho})}{2} \, \mathrm{d}S, \tag{5.1}$$

where ρ and r are the distances from the source to the aperture midpoint, and from the midpoint to the field point, respectively. Quantities $\hat{\mathbf{r}}$, and $\hat{\rho}$ are unit vectors from the aperture midpoint to the directions spanned by the source and the field point. Dot products with the aperture normal $\hat{\mathbf{n}}$ depend on the angle of observation. The equation presumes a point source adequately far from the aperture. It can be justified through the general wave equation and Green's theorem [63, Appendix 2].

The integration in Eq. (5.1) is performed over the aperture surface S_a, which is divided to differential pieces $\mathrm{d}S$. It sums up the contributions of each differential surface area to the diffracted field. For example, a rectangular aperture of side lengths a and b can be integrated as follow:

$$u(\mathbf{r}) = u_0 \frac{i}{\lambda} \int_{-a/2}^{+a/2} \int_{-b/2}^{+b/2} \frac{e^{-ik(\rho+r)}}{\rho r} \frac{\cos(\hat{\mathbf{n}} \cdot \hat{\mathbf{r}}) - \cos(\hat{\mathbf{n}} \cdot \hat{\rho})}{2} \, \mathrm{d}y \, \mathrm{d}x. \tag{5.2}$$

Based on the Pythagorean theorem and [63, pp. 498], ρ and r can be written as:

$$\rho = \sqrt{(x - x_S)^2 + (y - y_S)^2 + (z - z_S)^2} \tag{5.3}$$

$$r = \sqrt{(x - x_F)^2 + (y - y_F)^2 + (z - z_F)^2}, \tag{5.4}$$

and $y_S = z_S = y_F = z_F = x = 0$, when the source and the field point are adequately distant from the aperture. Other terms in the integral can be opened writing the aperture normal as $\hat{\mathbf{z}}$ when the dot product term yields $(1 + \cos\theta)/2$ [63, ch. 10]. Hence, the radiation from the aperture is mainly concentrated beyond the aperture, parallel to the incoming light.

The aperture of Fig 4.1 starts to resemble a point source when observed from a distance significantly larger than a wavelength. Generally, this condition yields the far field of the aperture. Far field approximation is valid, when the distance from the aperture is large compared to the largest dimension of the aperture, W [63, pp. 464]:

$$\frac{W^2}{\lambda} << R. \tag{5.5}$$

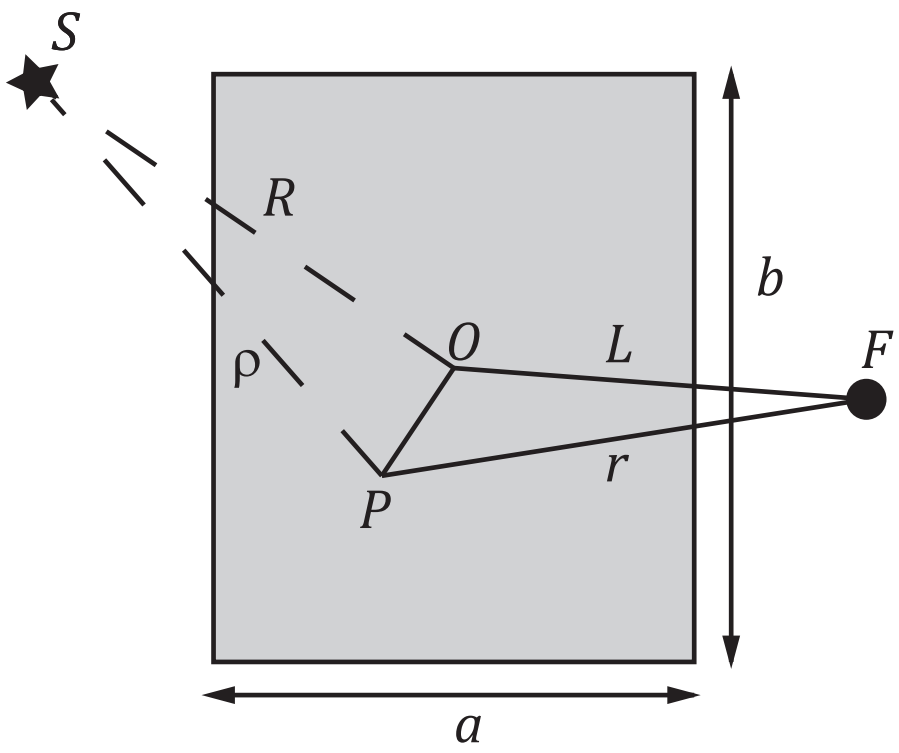

Figure 5.1: Diffraction from a rectangular aperture. S denotes the source point and F is the observation point of the field. The figure is three dimensional: the source resides on the back side of the aperture.

In far field, light radiated by the aperture can be considered in paraxial approximation. In the approximation, rays interfere with each other in simplified picture. Two adjacent rays have a phase difference, which depends on aperture dimensions and the angle θ. Similar theory also describes diffraction gratings.

A diffraction grating consists of periodic disturbances in refractive index. These disturbances can be slits, grooves or variations in surface height. In addition, they can be variations in the grating materials. [69, ch. 1.1].

Grating diffraction is analyzed as diffraction from multiple slits in far field. Therefore, the basic principles of constructive and destructive interference remain unaltered. Gratings are divided, based on their operational principle, in reflection and transmission gratings [69, ch. 1.1]. Grating elements can either transmit or reflect the incoming light. Operation of a diffraction grating is solely based on the interference between the deflected rays.

As shown in Fig. 5.3, interference in a grating origins from the path differences from A to B and from C to D. The distances AB and CD can be written as functions of the angles of incidence and diffraction, θ_i and θ_m, where m refers to the order of diffraction:

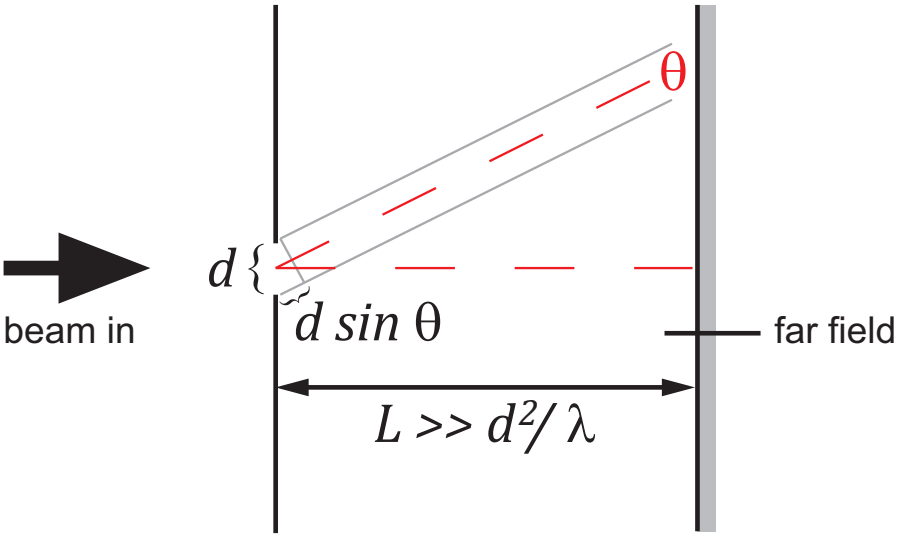

Figure 5.2: Fraunhofer diffraction in the far field.

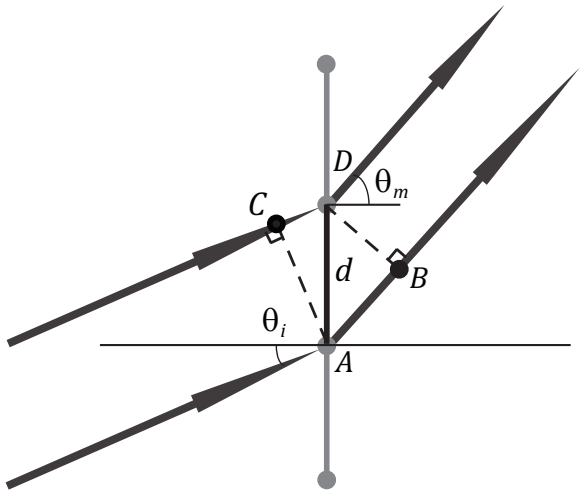

Figure 5.3: Diffraction from a grating. Taken from [63, ch. 10].

$$AB = d \sin \theta_m$$
$$CD = d \sin \theta_i.$$

The total path difference between the rays scattered from A and D is hence

$$AB - CD = d\,(\sin \theta_m - \sin \theta_i) = m\lambda, \tag{5.6}$$

where the last equality yields the angles θ_m for the diffraction maxima. This is equal to

$$kd\left(\sin\theta_m - \sin\theta_i\right) = 2m\pi, \tag{5.7}$$

which can be written for the minima as

$$kd\left(\sin\theta_m - \sin\theta_i\right) = \left(2m+1\right)\pi. \tag{5.8}$$

In above equation, m is an integer. Equations (5.6)-(5.8) can be interpreted as matching of wavenumber transverse components. Dividing (5.7) by d yields

$$\begin{aligned} k\sin\theta_m - k\sin\theta_i = k_{mT} - k_{iT} = \frac{2m\pi}{d}. \\ k_{mT} = k_{iT} + \frac{2m\pi}{\Lambda}. \end{aligned} \tag{5.9}$$

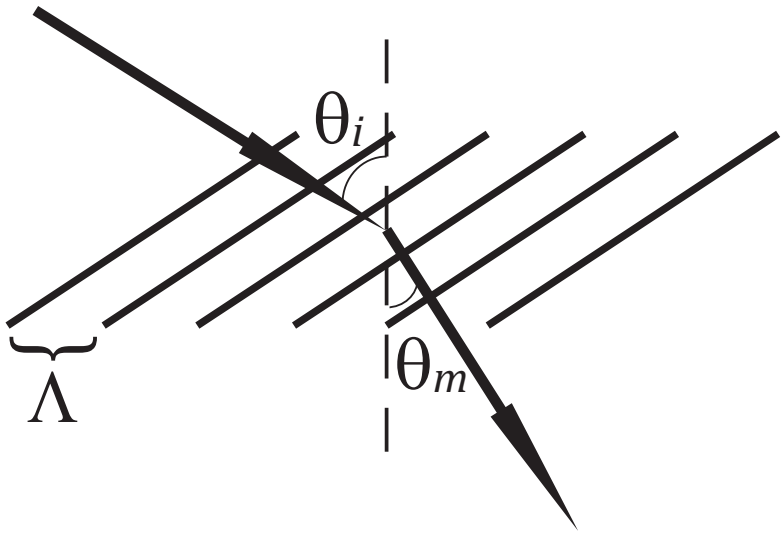

Figure 5.4: Diffraction from an array of long wires.

Here, the last expression states that the diffracted order m has to have a transverse wavenumber k_{mT}, equal to the incident light summed to a lattice vector $2\pi/\Lambda$. Variable Λ denotes the grating period and is equal to d in Fig. 5.3. Equation (5.9) requires the phases of the incident and diffracted waves to be matched on the grating boundary. When multiplied by Planck's constant, the equation is converted into

Table 5.1: Angles of incidence calculated for the diffracted wavenumber of $11.48 \cdot 10^6$ rad/m, and parameters of $\Lambda = 630$ nm, $\theta_i = 17.5\,^\circ$, and $\lambda = 1.55$ µm. These parameters are close to those optimal for SOI (silicon on insulator) waveguide gratings at 1.55 µm [1, pp. 51]. The angles were calculated for the five first diffraction orders. The grating equation has no solution for $m = 0, 2, 3$ or 4.

m	0	1	2	3	4
θ_i(deg)	-	21.8	-	-	-

$$\hbar k_{mT} = \hbar k_{iT} + \hbar \frac{2m\pi}{\Lambda}. \tag{5.10}$$

Equation (5.10) describes conservation of photon momentum. The left hand side of the equation describes the diffracted photon momentum whereas the right hand side describes the sum of the incident momentum and a term arising from lattice interaction [12, ch. 4.4], [70, ch. 3]. Therefore, Equation (5.10) can be applied also in subwavelength structures where the ray interpretation of light is not correct.

Equation (5.10) allows for calculating the angles of incidence (θ_i) when the diffracted wavenumber is known. This is done in Table (5.1). In the calculations, the grating was approximated by an array of thin slits acting as cylindrical sources when illuminated by a plane wave (Fig. 5.4). This treatment is justified in the far zone. As the table shows, a particular angle corresponds to the constructive diffraction for a given wavenumber.

5.2 Gratings couplers in silicon photonics

Diffraction gratings offer the possibility to couple light to a photonic waveguide. They serve as a typical realization of a coupler device besides lateral tapers described in Ch. 4. The use of a grating as a coupler is possible due to the interaction with a periodic lattice and the incoming light. Modes in a SOI (silicon on insulator) waveguide have higher propagation constant due to silicon index of refraction. Such propagation constant is unachievable for light incident from air above a silicon waveguide. Even though the wavevector of the incident light would be parallel to the waveguide, the longitudinal component would not be as high as the propagation constant of the lowest order modes. However, introducing a grating allows for adding a lattice vector to the longitudinal wavenumber. This mathematically describes the operation of the grating. With adequately high m, the required wavenumber is met enabling the coupling.

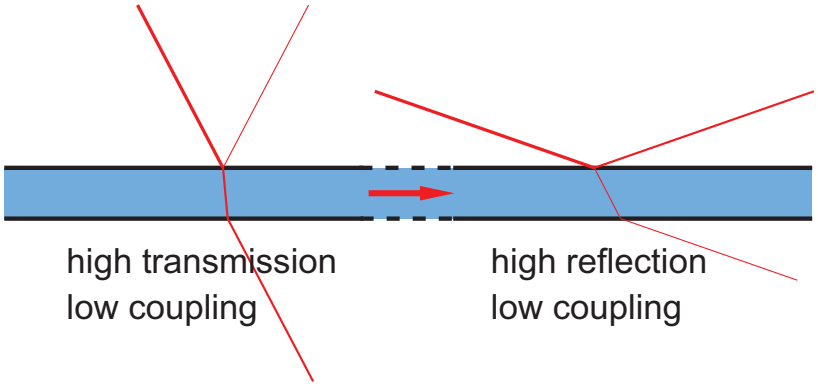

Figure 5.5: Small and large angles of incidence result in low coupling to a SOI waveguide. For small angles, the majority of power passes the waveguide, for large angles, the reflection becomes dominant. Grating couplers can solve this problem.

Grooves or irregularities in the waveguide surface can collect light because the propagation of the incident beam makes smaller angle with the waveguide boundary. Large angles of incidence favor reflection whereas small angles favor direct transmission. Transmission in the longitudinal direction of the waveguide is required to achieve coupling. Because reflection and transmission depend on polarization, as do the photonic waveguides, gratings in silicon photonics are strongly polarization dependent components.

5.2.1 Grating types

The simplest grating geometry consists of an infinite amount of narrow, infinitely long, rectangular grooves with an uniform spacing. These grooves have an aspect ratio of 50 %, as they fill half the period of the grating. Such geometry is called uniform or symmetric because it only contains the grooves of equal dimensions. In principle, two rectangular uniform geometries can only be different if their grooves are not equally deep or if their aspect ratios are different. In addition, the scale of the geometries can vary. Uniform geometries have a well defined period and the phase matching condition can be applied to them.

When considering finite size gratings, a single uniform geometry is divided to two categories. The grating can be composed of grooves or ridges, which are thicker sections of the waveguide. Both geometries can be considered uniform, as their period is constant and all the grating elements are equal. However, the geometries function differently because the ridge geometry provides space for a mode to expand.

For waveguides of similar thickness, the ridge geometry has higher effective refractive index. This is due to the "weighted average" nature of the effective index, which takes into account all the materials surrounding the waveguide. However, generally the order of the indices is opposite, because the manufacturing process leads to thicker

waveguides for groove geometry. Effective index affects the scattering properties and reflections inside the waveguide.

Figure 5.6: Groove- and ridge-geometries of a finite sized uniform grating.

Reflections from the grating surface can be minimized by altering element shape. One alternative is to utilize slanted gratings. Slanted gratings consist of elements bent in some angle with respect to the grating normal. This enables higher coupling efficiencies at normal incidence, improved tolerance to the fiber alignment and broadband frequency response [71]. The improved vertical coupling can be understood by the reflection and transmission occurring with respect to the element normal, which is inclined at angle [69, ch. 2.1]. Similar approach is to utilize triangular or "sawtooth" elements. These geometries are called blazed and they can be utilized to shrink the grating in longitudinal direction [72].

Figure 5.7: Blazed "sawtooth" geometry.

The diffraction pattern produced by the grating depends on element sizes. If each element is seen as a slit, the maximum diffracted intensity is proportional to the slit area. This follows from the integration (18) where borders change according to the aperture size. Hence, wider grating elements produce stronger diffraction.

Figure 5.8: A grating modulated by altering the element width.

Selecting the element widths according to the desired distribution allows for tuning of the diffracted intensity distribution [45]. Similar effect is achievable by altering the element size by other means. Tuning the element dimensions can significantly reduce the losses caused by the mode mismatch of Eq. (4.3). Furthermore, applying an element distribution restricts the grating length to a finite value, which has important secondary effects to the coupling.

The phase matching equation does not describe finite length gratings accurately. The grating profile has discontinuities on the edges. This can be interpreted as a group of wavenumbers associated to the grating (as in Fourier analysis). Hence, the grating period is not mathematically well defined. This broadens the angular spectrum available for the grating, because the angle of incidence where the coupling occurs depends on the period. [73], [74], [1, ch. 3.2]

Furthermore, also finite width limits the description of gratings. The two dimensional picture provided by the earlier description fails to describe gratings accurately. Nevertheless, in many cases a planar waveguide approximation can be extended also in the grating. If the grating width is significantly larger than the waveguide thickness, it resembles an infinite structure in transverse direction. This approximation is shown to yield 2 % higher coupling efficiencies compared to the real efficiencies [45].

The dimensional structures provide applications, which would otherwise be impossible to realize. For example, polarization dependency of a grating coupler can be compensated by a grating, which is composed of two perpendicular uniform gratings. These gratings form a superposition of a square lattice. [75] This lattice geometry can be utilized to separate different polarizations on a SOI (silicon on insulator) platform. [76].

SOI gratings typically consist of an array of grooves etched in the silicon waveguide. A shallow etched grating is one where the etches can be approximated as small perturbations in the waveguide surface. Such grating does not interfere the mode propagation and the waveguide modes remain unaltered [77]. The only effect of the grating is to reduce the propagating power due to the scattering.

5.2.2 Coupling through a shallow etched grating

Shallow etched gratings can be considered periodic arrays of line like scattering sources, which justify use of phase matching condition as approximative tool. The grating elements can be approximated as slits radiating the mode energy outwards from the waveguide. Hence, the grating equation can be written as

$$\beta_i = k_{scT} + \frac{2m\pi}{\Lambda}, \tag{5.11}$$

where β_i is the propagation constant of the ith mode of the waveguide. Parameter β can also be written as

$$\beta = k_0 n_{eff}, \tag{5.12}$$

where n_{eff} is the effective mode index of the waveguide. Equation (5.11) allows for determining the angle, which corresponds to the maximal coupling. This angle is equal to the angle, calculated for diffraction maximum.

Above equations are valid for switched input and output of the grating. This reciprocity implies that a grating scatters waveguide power to the same direction, where maximal coupling is achieved in reciprocal excitation. In other words, highest scattered intensity is achieved in the angle, which corresponds to the highest coupling to the waveguide [78, ch. 4]. Consequently, the field profile mismatch and coupling efficiency follow similar reciprocity.

Rigorous treatment of diffracted intensity begins from solution of Maxwell's equations. Similar methods are valid for solving the fields inside the grating or the scattered fields above the grating surface. These fields obey the wave-equation [79, pp. 34], which can be written for y-directed TE-polarization (transverse electric field) as

$$\frac{\partial^2 E_y(x,z)}{\partial x^2} + \frac{\partial^2 E_y(x,z)}{\partial z^2} + k_0^2 \epsilon(x,z) E_y = 0. \tag{5.13}$$

In addition, they satisfy electromagnetic boundary conditions, such as continuity of the field tangential components and flux density normal components. Additional conditions arise from the periodicity of the grating structure. The fields have to share the periodicity of the grating [79, pp. 35]:

$$E_y(x,z) = \sum_{m=-\infty}^{\infty} G(z)\, e^{i\frac{2\pi m}{\Lambda}x}, \tag{5.14}$$

where $2\pi m/\Lambda$ is the x-component of the lattice vector described earlier. Electric field E_y is said to be "pseudo-periodic" [79, pp. 38] because it is modulated by the grating.

Figure 5.9: TE-polarized field propagating in a grating.

Fields inside the grating have periodicity of E_y. Equation 5.14 can be inserted in the wave-equation, which can be solved by separation of variables, $E_y(x,z) = E_y(x)\,E_y(z)$. The solution of the field becomes

$$E_y(x,z) = \sum_{m=-\infty}^{\infty}\sum_{l=-\infty}^{\infty} P_{ml} e^{i\frac{2\pi m}{\Lambda}x}\left[a_l e^{i\gamma_l z} + b_l e^{-i\gamma_l(z-h)}\right], \tag{5.15}$$

where terms $e^{i\pm\gamma_l z}$ represent bouncing waves in the waveguide and coefficients P_{ml} depend on $\epsilon(x,z)$. These coefficients can be obtained by inserting $E_y(x)$ into the wave-equation, multiplying the result by $e^{-i\alpha x}$, doing this for each grating element and solving the resulting matrix equation [80](J. Turunen).

Fields outside the grating can be calculated in a similar method. In the case of infinite grating and plane wave excitation, they are periodic in the direction of grating [79, pp. 35]. However, when a spatially restricted beam is incident, the diffracted magnitude drops farther from the focus of the beam.

The grating elements in the beginning of the grating scatter the power otherwise available for the elements on the other side of the grating. This power is directly reduced from the waveguide mode in the small perturbation approximation. Hence, a differential equation can be written for the power propagating in the waveguide (origin is located at the beginning of the grating):

$$\frac{\partial P(z)}{\partial z} = -2\alpha(z)\,P(z). \tag{5.16}$$

Symmetric gratings have constant α, which leads to an exponential solution of the equation

$$P(z) = P_0 e^{-2\alpha z}. \tag{5.17}$$

Exponentially dropping power generates exponential output intensity distribution, which allows to define a measure called coupling length. Coupling length is the length of grating where most power is coupled into or out of the waveguide. A general definition of the coupling length is obtained setting the exponential of Eq. (5.17) to -2. [81] This produces expressions

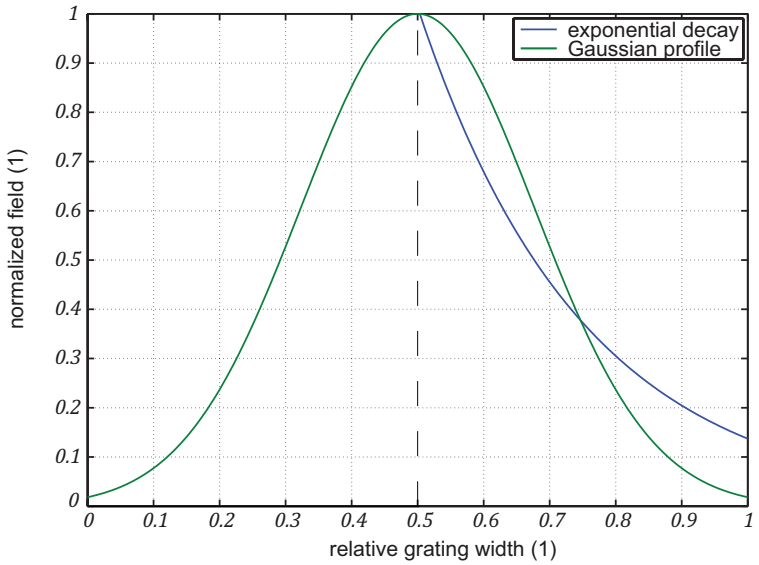

Figure 5.10: Maximum overlap of a Gaussian profile and exponential decay.

$$-2\alpha L_{cpl} = -2.$$
$$L_{cpl} = \frac{1}{\alpha}. \tag{5.18}$$

Coupling length can be optimized to utilize the major part of the scattered power. This optimization is performed by calculating the overlap with the exponentially decaying output field and, for example, fundamental fiber mode [82]. The field profile overlap is maximized when the exponential decay is matched to the other half of the Gaussian profile (Fig. 5.10). [49] This yields coupling length of

$$L_{cpl} = \frac{w_0}{1.37 \cos\theta_i}, \tag{5.19}$$

where w_0 denotes the radial width of the Gaussian. The reciprocal situation can be utilized to determine the optimal number of grating elements. If a beam with Gaussian intensity profile is directed to the grating center, the grating has to be at least twice the coupling length wide to collect the highest amount of power. For example, when the beam is incident at 17.5 ° and 1.55 µm wavelength, an uniform grating with 630 nm has to be $\approx$ 6.3 µm long. Hence, 13 elements are required to achieve optimal coupling. Gratings with more elements start to scatter the light out of the waveguide, which reduces the coupling efficiency.

Grating coupling has several loss mechanisms in addition to the mode mismatch. Grating elements can reflect a fraction of propagating light backwards. This issue is met particularly when power is excited from the waveguide. Back reflection can be observed as a counter propagating wave in the diffraction pattern produced by the grating. When the excitation comes from the free space (fiber-to-chip links), reflection from the waveguide surface, as well as transmission through the waveguide, serve as loss mechanisms (Fig. 5.5). Reflection from the fiber facet can cause losses when the power is propagating to the fiber. The coupled power can be represented as an approximative sum, which takes into account the major loss mechanisms in grating coupling:

$$P_{cpl} = P_{in} - \left(R_{back} + R_{top} + T_{pass} + (1 - \eta_{overlap})\right) P_{in}. \tag{5.20}$$

Terms R and T represent reflection and transmission and depend strongly on polarization. The last term inside the brackets describes mode matching, including the back scattering effect. Element sizes can be tuned to reduce the mode mismatching losses. This turns α to a function of z. The Equation (5.16) can be solved for alpha when knowing the scattering distribution $\partial P\left(z\right)/\partial z$. A Gaussian distribution maximizes coupling between the nearly Gaussian fundamental fiber mode. Such distribution also produces Gaussian output field profile. For corresponding $P\left(z\right)$

$$\frac{\partial P\left(z\right)}{\partial z} = e^{-\left(\frac{z - z_0}{\sigma}\right)^2} = G^2\left(z\right). \tag{5.21}$$

Therefore, the following equations can be written

$$-2\alpha\left(z\right) P\left(z\right) = -\, G^2\left(z\right). \tag{5.22}$$

$$\frac{\partial P\left(z\right)}{\partial z} = -\, G^2\left(z\right). \tag{5.23}$$

This pair of equations can be solved for $P\left(z\right)$ and $\alpha\left(z\right)$. The scattered power P_{sc} can be solved by integrating from the grating beginning to some point z:

$$P_{sc}\left(z\right) = \int_0^z G^2\left(z'\right) \mathrm{d}z'. \tag{5.24}$$

The actual propagating power is the complement of the scattered power:

$$P(z) = 1 - \int_0^z G^2\left(z'\right) \mathrm{d}z', \tag{5.25}$$

where the power is normalized with respect to 1 W. The scattering strength α can be solved from the other equation:

$$-2\alpha(z)\left(1 - \int_0^z G^2\left(z'\right) \mathrm{d}z'\right) = -G^2(z), \tag{5.26}$$

which results in

$$\alpha(z) = \frac{G^2(z)}{2\left[1 - \int_0^z G^2(z')\,\mathrm{d}z'\right]}. \tag{5.27}$$

The exponential dependence of the scattering on z has to be balanced to achieve a Gaussian output beam. Balancing requires increasing the element size in the end side of the grating because the elements there have to radiate more. Hence, the initial Gaussian element distribution can be multiplied by an increasing function. Equation (5.27) yields this function and the correct element size distribution. Elements chirped according to the equation radiate an output mode of Gaussian profile.

6 Simulation methods

In this work, grating couplers are analysed numerically. Such analysis requires knowledge of the coupled and propagating power. Optical power is stored in electric and magnetic fields. Hence, power cannot be known without knowing the fields. These fields carry energy between the structures of interest. Therefore, knowing the field distribution provides information of the power transfer and coupling efficiency. Finite element method (FEM) is designed to solve for electromagnetic fields in complex geometries. When solving for the fields, desired power values and efficiencies are solved as a by product.

This chapter represents the methods utilized in this thesis. The obtained results rely on the numerical methods utilized in the computation. These methods were tested to ensure their validity. Due to several error sources, such testing became important during the work, and the last sections of this chapter are devoted to testing methodology.

6.1 Finite element method

Sharp edges, small details, and complexity of photonic grating structures require the use of advanced numerical techniques. Such techniques should be capable of handling complex geometries with high computational speed. Therefore, finite element method (FEM) was selected as the method of simulations. The method is flexible with respect to geometry due to discrete field representation.

It is possible to discretise potentials, fields, or current densities that produce the fields. In FEM, the potentials or fields are discretised, whereas the current density method is called method of moments (MoM). Generally FEM leads to simpler mathematical formalism and is faster to solve.

Dividing the computational domain in finite subdomains offers a means to discretise the fields. Electric field can be defined in each subdomain in piecewise representation. In practice, subdomains can be composed of smaller domains where the fields have piecewise definition. The set of the smallest domains is called mesh and the intersections of these fundamental areas are the nodes of the mesh. The starting point in FEM is the generation of the computation mesh. This mesh can be composed of triangular or rectangular elements, or in 3D, tetrahedrons or hexahedrons.

Mesh elements have to satisfy several optimization conditions to provide a high quality mesh. Such criteria try to minimize the maximum angle of a triangle, maximize the minimum angle of a triangle, minimize triangle circumference and minimize the sum of all edge lengths in the mesh [83, ch. 1-2]. A triangle, which resembles equilateral has optimal properties for many purposes. Any other triangle would have at least one angle that is larger than 60° and one angle that is smaller. Typically, the elements can be further modified to better match the model geometry.

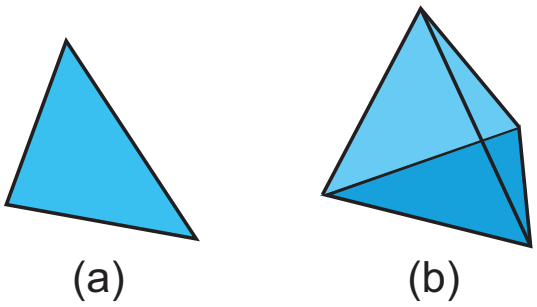

Figure 6.1: Typical mesh elements for (a) two dimensional, (b) three dimensional geometries.

There are several general principles, which hold in mesh generation. For example, higher number of mesh elements generally provides more accurate solution than lower number of elements. Electromagnetic models utilize smaller elements in regions where fields or potentials change rapidly. Otherwise the solution would become inaccurate as the discretisation would be far larger than the scale of the variation. Similar scaling is often required in regions where the geometry becomes detailed.

Constructing a high quality mesh with high number of elements generally requires mesh formation in a particular order. The order of meshing phases affects the mesh formation because each element is calculated from existing node data [84]. Therefore, elements, which are already formed determine position and shape of the remaining elements. The mesh elements have to be scaled according to geometrical details and the other mesh elements.

One means to generate high quality mesh is called approaching front method. In this method, points are set on the geometric surfaces, after which the computational domain is divided to the subdomains. An algorithm generates the mesh from the model boundaries towards the central parts of the model. In each phase, the algorithm adds a layer of mesh elements and performs a check to ensure no overlap between different fronts occur. [84]. In this work, advancing front technique was utilized with minor modifications. These modifications concern the direction of mesh generation, which started from the central parts of the simulation model.

Meshing techniques make up a detailed theory impossible to cover here [84], [85, pp.11-13]. Efficient meshing requires automated algorithms as the number of subdomains can reach tens of thousands of elements. Commercial codes have to minimize the number of mesh elements while maintaining high quality of the solution. In addition, the codes have to be flexible enough to handle different types of geometries. These complexities require detailed mathematical theory, such as Delaunay methods and dynamic programming. Former is a geometrical method for optimizing the element shape and the latter denotes an optimization method where the optimization is performed from the desired result (complete mesh) to the starting point [83, ch. 1.3]. Many books have been written on the topic. No further theory is represented here for it would make a thesis of its own.

The following description of FEM equations is based on [86, ch. 2-3]. Dividing the computational domain in finite subdomains offers an alternative for representing the unknown potential or field as a weighted sum of basis functions, which are assigned to each subdomainn node or edge of the mesh. These functions fulfill the electromagnetic boundary conditions. The differential equation with the unknown function is converted into a problem where the weights of the basis functions are unknown. Solving these coefficients demands multiplying the series expansion with a series of weight functions with suitable properties. After that, each equation can be integrated over the computational domain to obtain a group of scalar equations. These scalar equations turn into a matrix equation where the unknown coefficients are stored in a vector $\mathbf{x}$

$$\mathbf{A}_{nm}\mathbf{x}_n = \mathbf{b}_n. \tag{6.1}$$

This equation reveals that the amount of weight functions has to be greater or equal to the amount of basis functions. It requires computation of $n \times m + n$ integrals if the matrix $\mathbf{A}$ has no symmetry properties, which can be utilized in computation. This requirement arises from the number of matrix elements and elements in the excitation vector, which are typically obtained through integration. After calculating the integrals, the matrix $\mathbf{A}$ has to be inverted to solve $\mathbf{x}$. Modern computers perform the task fast and accurately.

The simplest basis functions in FEM are called linear nodal basis functions, denoted by N_i^k. The indices i and k refer to node i in element k. Therefore i is a local index in a global mesh where k runs through each element of the mesh. Functions N_i^k have value 1 at node i and value 0 at every other node of the element k. They are associated to certain nodes of the mesh and drop linearly to 0 in the adjacent nodes to i. Thus, functions N are defined in all the elements surrounding the node i. Linear nodal functions are adequate for describing potential in electrostatics. Potential inside element k of the mesh can be represented as a sum

$$\sum_i^3 N_i^k\,(x, y)\,\phi_i^k, \tag{6.2}$$

where ϕ_i^k is the voltage in node i of a triangle. However, describing fields require vector basis functions. Such functions can be formed by a linear superposition of nodal functions and their gradients as:

$$\mathbf{w}_{ij}^k = N_i^k \nabla N_j^k - N_j^k \nabla N_i^k. \tag{6.3}$$

These functions are associated to edges ij between nodes i and j. They satisfy electric boundary conditions for the electric field tangential component and electric flux density normal component are tangential and perpendicular to element boundaries respectively. Combining two of these functions gives the actual basis function connected to the edge ij. In Galerkin's method the basis functions and the testing functions are the same. Galerkin's method is a standard technique, which was utilized in this work. Hence, the theory above is adequate for formulating the problem.

The equation of interest in this thesis is the wave equation describing the waveguide mode propagation as well as the propagation of scattered light by a grating. The wave equation can be written formally as

$$\nabla \times \nabla \times \mathbf{E} - k_0^2 n^2 \mathbf{E} = \mathbf{0} \tag{6.4}$$

assuming homogeneous, nonmagnetic and isotropic medium. Equation (6.4) is also known as the Helmholtz equation [47]. Finite element formalism requires converting the equation into an integral form. This is possible by first replacing the unknown electric field by a series of basis functions $\mathbf{w}_i$:

$$\nabla \times \nabla \times \sum_i^N c_i \mathbf{w}_i - k_0^2 n^2 \sum_i^N c_i \mathbf{w}_i = \mathbf{0}. \tag{6.5}$$

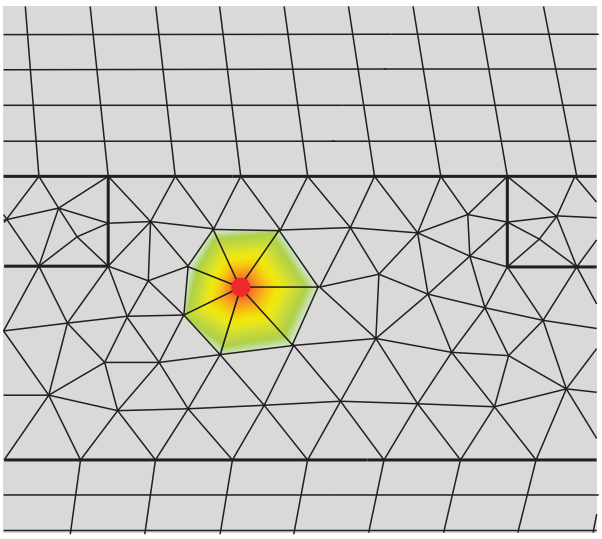

Figure 6.2: An example of mesh and a linear nodal basis function associated to the selected node (red circle). The sample represents a part of the real mesh used in the simulations of this work.

Equation (6.5) can be multiplied by testing function $\mathbf{w}_j$:

$$\mathbf{w}_j \cdot \sum_i^N c_i \nabla \times \nabla \times \mathbf{w}_i - k_0^2 n^2 \mathbf{w}_j \cdot \sum_i^N c_i \mathbf{w}_i = \mathbf{0}. \tag{6.6}$$

Here summation goes over each edge of the computation mesh. Integrating Equation (6.6) generates a scalar coefficient for each pair ij:

$$\sum_i^N \int_D c_i \mathbf{w}_j \cdot \nabla \times \nabla \times \mathbf{w}_i \mathrm{d}V - k_0^2 n^2 \sum_i^N \int_D c_i \mathbf{w}_j \cdot \mathbf{w}_i \mathrm{d}V = 0 \tag{6.7}$$

where each coefficient is composed of two integrals over the computational domain D. These coefficients can be written as a matrix as:

$$\mathbf{A} = [\mathbf{a}_1 \quad \mathbf{a}_2 \quad \mathbf{a}_3 \quad ... \quad \mathbf{a}_N] \tag{6.8}$$

$$\mathbf{a}_i = [a_{i1} \quad a_{i2} \quad a_{i3} \quad ... \quad a_{iM}]^T \tag{6.9}$$

and

$$a_{ij} = \int_D \mathbf{w}_j \cdot \nabla \times \nabla \times \mathbf{w}_i \mathrm{d}V - k_0^2 n^2 \int_D \mathbf{w}_j \cdot \mathbf{w}_i \mathrm{d}V. \tag{6.10}$$

Fitting into Equation (6.1) would give vector $\mathbf{x}$ defined as

$$\mathbf{x} = [c_1 \quad c_2 \quad c_3 \quad ... \quad c_N]^T. \tag{6.11}$$

These considerations are, however, not adequate because the basis functions have to meet several criteria to be applicable. A basis function should be square integrable but not necessarily twice differentiable. Therefore, the double derivative in the coefficients a_{ij} has to be converted into single derivatives. To write this weak formulation, double curl theorem can be applied

$$\nabla \cdot (\mathbf{F} \times \mathbf{G}) = \nabla \times \mathbf{F} \cdot \mathbf{G} - \nabla \times \mathbf{G} \cdot \mathbf{F} \tag{6.12}$$

This equation can be inserted in Eq. (6.10) to obtain

$$a_{ij} = \int_D \nabla \cdot (\nabla \times \mathbf{w}_i \times \mathbf{w}_j)\,\mathrm{d}V + \int_D \nabla \times \mathbf{w}_i \cdot \nabla \times \mathbf{w}_j \mathrm{d}V - k_0^2 n^2 \int_D \mathbf{w}_i \cdot \mathbf{w}_j \mathrm{d}V. \quad (6.13)$$

Then Gauss theorem can be applied to the first term, finally giving the boundary term

$$\int_{\partial D} \nabla \times \mathbf{w}_i \times \mathbf{w}_j \cdot \mathbf{dS}. \quad (6.14)$$

The value of this term is determined by the boundary conditions on ∂D. It is included in the matrix $\mathbf{A}$ elements in Eq. (6.10). Functions $\mathbf{w}_{ij}$ have to be selected such that they obey electromagnetic boundary conditions. For example, they are perpendicular to an ideal conductor surface and their tangential components are continuous across dielectric boundaries. Hence, initial conditions or excitations of an electromagnetic problem can be set by determining basis function values on selected boundaries. Because functions $\mathbf{w}_{ij}$ represent electric field, a field excitation can be set by two steps:

1. Setting basis function values on a selected edge by setting their coefficients c_i to a known value.
2. Setting testing function values $\mathbf{w}_j$ on the selected edge to zero.

These steps force the matrix Equation (6.1) to give desired values for the solution on the edge where the electric field is determined by excitation. This Dirichlet boundary condition is applied in the simulations to generate desired excitation fields. When applied to a boundary, the boundary is converted into an aperture, which is known to radiate the Fourier components of the aperture field [87, ch. 17]. This treatment of an aperture radiator is found in diffraction [88, ch. 3] theories where slits irradiated by electromagnetic field are considered.

6.2 Simulation models

Simulations of the studied grating structures utilize *2D-approximations*, which is justified by [45], [89], [27] and [1, pp. 47]. This considerably speeds up the computation, which would otherwise become impractically slow. Fast computation enables

this type of studies, because hundreds of simulations are required to obtain the desired results. Further simplifications for polarization and wavelength are required as well. For the same reasons, only TE-polarization (transverse electric field) and optical C-band (conventional band) around 1.55 µm are studied.

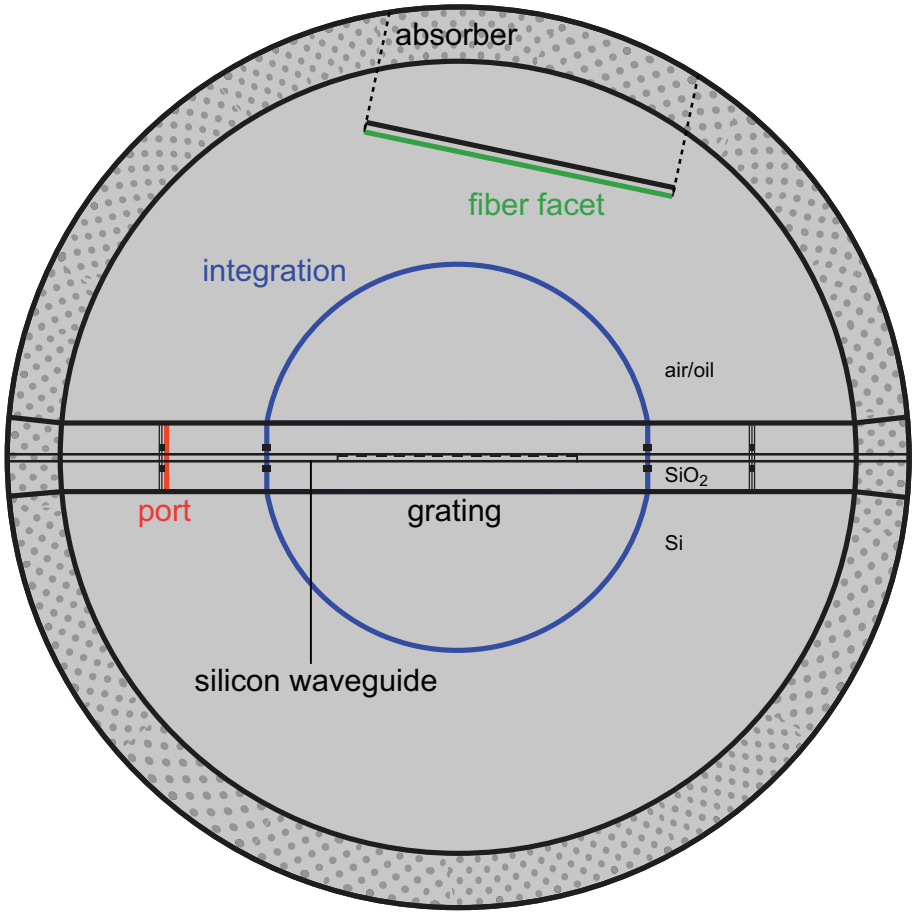

Figure 6.3: The main characteristics of the constructed model. The waveguide thickness in this work was 220 nm and the botton oxide layer (SiO_2) was 1 µm thick. The distance of the fiber from the grating midpoint was 10 µm measured from the fiber center. The grating element number was 13 in all simulations. The figure describes a 2D-model.

Use of a commercial software guarantees the best quality of the simulation results possible. COMSOL is an international company, which provides simulation tools for many distinct fields of physics. COMSOL provides finite element based tools designed to model electromagnetic fields and their interaction with materials. COMSOL Multiphysics software has an user interface, which allows for construction of a complete FEM (finite element) model with a relatively easy effort. Construction of geometry, meshing, solving and postprocessing are all available in one package. Therefore, COMSOL was selected as the simulation tool in this work. This study only utilized the RF (radio frequency) engineering package of COMSOL Multiphysics version 4.3.

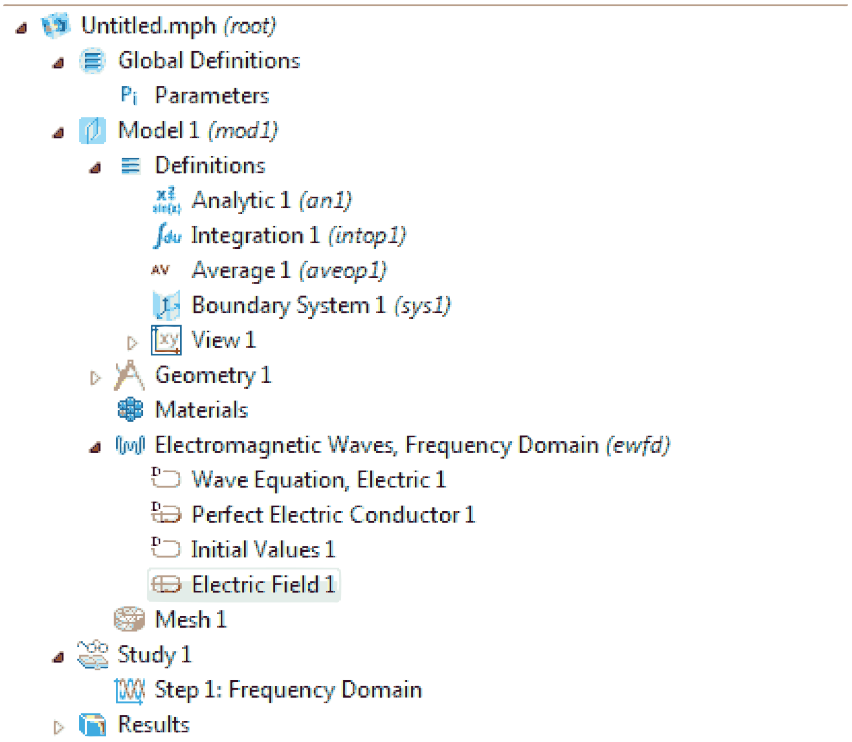

Figure 6.4: COMSOL model tree. Functions and integration boundaries are implemented in the definitions-node.

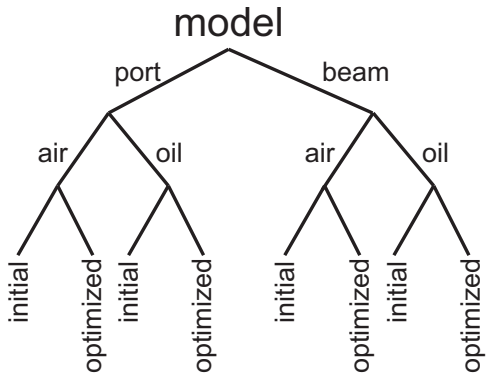

Figure 6.5: The structure of the comparison performed in this study.

Construction of a COMSOL model occurs in tree-like order where the geometry is created first. When the geometry is finished, user can generate the mesh, which requires geometrical details as an input. User can also determine global parameters, which can be associated to different model measures. For example, defining a refractive index requires insertion of one global parameter value, n, which can depend on the other parameters, such as wavelength, wl. COMSOL has tools for defining analytic functions as global parameters. Such functions can have one or more input parameters and one output parameter. Input parameters can include global geometrical definitions as coordinates x,y and z. A function can represent, for

example, electric field, which depends on these coordinates. COMSOL tools enable definition of integration boundaries and boundaries with well defined electric field. More about the software can be read from the user's manual [90].

COMSOL was utilized to study and compare two grating structures and two excitations. The simulated gratings were formed by 13 $70 - 90$ nm shallow etches in 220-nm-thick Si waveguide on top of a $SiO2$ buffer layer. They include an initial geometry with constant grating element width and an optimized geometry with varying element width. The optimized geometry was searched before the comparison. Both structures were simulated with two different cover materials: air and index matching oil ($n = 1.45$). The performance of the structures was compared with respect to their coupling efficiencies. Two power values were measured for all the simulated structures. These power values consist of the coupled power and power scattered by the grating when the fundamental waveguide mode is incident in the waveguide. The reasons for these additional simulations are explained later. However, two power values are necessary when trying to comprehend the influence of geometry on the coupled power. Hence, two different excitation schemes were realized in COMSOL.

6.2.1 Port excitation

Waveguide mode excitation can be utilized to study coupling out of the waveguide through a grating. Port boundary condition of COMSOL RF (radio frequency) engineering package can be utilized to create a field distribution, which corresponds to the fundamental mode of a waveguide. Such field distribution on waveguide cross section induces the mode in the waveguide.

The waveguide excitation is similar to typical excitation schemes of waveguides in RF technology. A waveguide can be excited by putting a current probe inside the waveguide in a position where the desired mode has corresponding value. Currents in the mode field direction generate the mode electric field [91]. In analogy, a boundary with a mode field distribution produces the mode inside the waveguide. This can also be understood through field apertures, which emit radiation based on the field distribution on the aperture [92]. A boundary with mode electric field radiates the field in a waveguide resulting in single mode propagation.

Propagation constant β of a waveguide mode is equal to the wavenumber longitudinal component k_z, which represents the propagation of the mode along the waveguide. In some sense, β defines the angles of the plane wave components in the mode Fourier-presentation. Fundamental mode of a waveguide has these angles near zero for light is guided almost directly through the waveguide.

COMSOL solving procedure executes two boundary mode type nodes in the COMSOL tree followed by frequency domain analysis for a well defined frequency. Boundary mode solver creates a field distribution along the port boundary corresponding

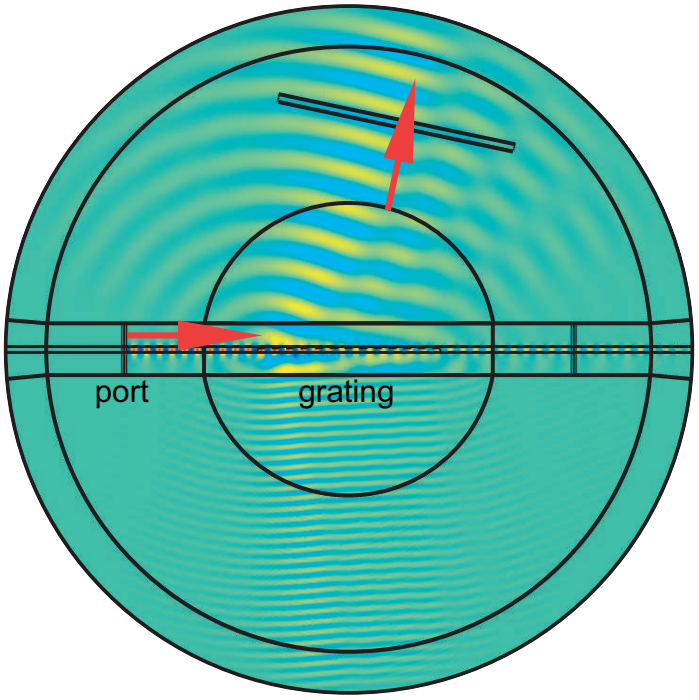

Figure 6.6: Port excitation model. Input is an electric field boundary with background areas removed from the computational domain. On the back side of the removed domains, electric field is set to zero. The figure describes a 2D-model.

to some effective refractive index of a mode. User can insert this value in COMSOL solver, which searches for the modes around the corresponding propagation constant. Effective index is

$$n_{eff} = \beta c/\omega. \tag{6.15}$$

This study is concentrated on modelling the fundamental waveguide mode and utilizes silicon refractive index (Eq. (2.1)) in the solver. In the boundary mode nodes, user is asked to give number of modes to be searched. While this work only is concentrated to the fundamental mode, the number can be set to 1 in all simulations. One mode has to be searched for the input, and one for the output port. The frequency domain solver calculates the electromagnetic fields based on the mode data provided by the boundary mode solvers. These two steps require separate "electromagnetic waves"-nodes (Fig. 6.4) in COMSOL with different computational domains and different boundary conditions.

Interior boundaries of a COMSOL model do not work as port boundaries. Therefore, port cannot excite a grating surrounded by absorbing material Fig. 6.3, as the excitation cannot penetrate the absorber. Separate model has to be utilized to

produce the waveguide mode inside the absorber. This was achieved by framing out a short section of the waveguide where the port boundary condition was utilized. No considerable losses occur when the simulated length of the waveguide is short enough and no perturbations in the waveguide geometry exist. Thus, the input mode field is also seen by the output port and by any other section of the waveguide. The field in the waveguide center can be copied to an electric field boundary defined outside the modelled section. Hence, it becomes possible to use the simulated mode field as an input of a following simulation, which includes the grating part of the model.

The simulation excludes half of the port modelling domains from the computational area and sets the boundaries of the domains as electric field boundaries. This creates a situation where one of the boundaries contains the copied mode electric field and the other boundaries are forced to maintain zero electric field strength. This corresponds to the Dirichlet boundary condition mentioned earlier. Hence, the pre-modelled half of the port domains appears metallic except for its rightmost front acting as a field source (Fig. 6.6). This reduces the computational effort because no information is required from the backside of the input port. The shadow cast by the metallic block imitates a situation where an external circuit is feeding power through the grating but is not affected by the grating behaviour.

Scattering occurs when the mode generated by the electric field boundary passes through the grating. The scattered power can be integrated over the blue semicircles of Fig. 6.3 (see Section 6.3.1). Integration yields an estimate of the up scattered power, which is required in the study of grating geometry. The power could reflect from the model boundaries if no absorber be implemented in the model.

An overall picture of the port excitation scheme contains two simulation steps. First, fundamental waveguide mode is solved in a short section of the waveguide to provide electric field distribution corresponding to that mode. Second, this electric field is copied in the outer boundary of the framed out section. This boundary acts as a port, and frequency domain analysers can be utilized to compute the mode field in the whole structure, which includes the grating. As the mode passes through the grating, power is scattered upwards. This power can be estimated by integrating power flux density.

6.2.2 Gaussian beam excitation

To estimate the coupled power, the grating of the model in Fig. 6.3 can be illuminated by a Gaussian beam. A Gaussian beam has an electric field profile, which obeys a Gaussian distribution [30, ch. 4.1]. As the beam propagates, it diverges as a result of diffraction. Divergence shapes the beam wave fronts as paraboloids with increasing curvature away from the beam middle region [65, ch. 3.2].

Electric field boundary condition provides means to realize Gaussian beam input in COMSOL. The condition allows user to write an analytic expression of the electric

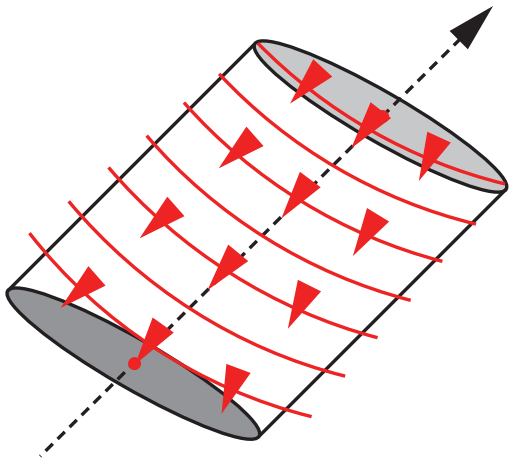

Figure 6.7: Gaussian beam power conservation. As the wave fronts diverge, direction of the powerflow changes causing leak of the power from the cylinder.

field on selected boundary, such as the green boundary in Fig. 6.3. The input realization resembles the one described for the port excitation earlier. The bottom side of the rectangle radiates as an aperture because the electric field is set to a known value. The other sides of the rectangle are set to zero field boundaries. This creates an illusion of a continuous optical fiber, which does not affect the grating (except through the Gaussian beam).

Total energy of the excitation beam is conserved resulting in a decrease in the field magnitude as it propagates. The focus of the beam is called its waist. Beam electric field reaches its maximum at the waist of the beam. Farther from the waist, decrease in magnitude occurs due to the divergence of the beam. When a cylinder is drawn around the beam axis, power flowing inside the cylinder decreases because a part of the power leaks out through the side walls (Fig. 6.7).

Gaussian beam is a three dimensional entity, which causes problems when trying to implement the beam in a 2D model. Three dimensional beam diverges in all directions away from the beam axis. When a plane is drawn through the beam axis, a projection of the beam is obtained on that plane. This projection represents the beam seen by a 2D model. Such projection loses power while propagating, because power can flow perpendicular to the plane of projection. Hence, the expression of 3D beam violates conservation of energy when inserted in a 2D model.

Real three dimensional Gaussian beam has a two dimensional (cylindrical) counterpart. The two dimensional description was utilized in this work because it conserves the power. A two dimensional Gaussian beam has an expression shown below [93]:

$$\mathbf{E}\left(\boldsymbol{\rho}, z\right) = \hat{\mathbf{x}} E_0 \sqrt{\frac{w_0}{w\left(z\right)}} \exp\left[-\frac{\rho^2}{2w_0^2}\right] \exp\left[-i\left(kz - \frac{\eta\left(z\right)}{2} + \frac{k\rho^2}{2R\left(z\right)}\right)\right]. \qquad (6.16)$$

Functions $w(z)$, $\eta(z)$ and $R(z)$ have following definitions:

$$w(z) = w_0\sqrt{1+\left(\frac{z}{z_R}\right)^2} \tag{6.17}$$

$$\eta(z) = \arctan\frac{z}{z_R} \tag{6.18}$$

$$R(z) = z + \frac{z_R}{z}z_R. \tag{6.19}$$

Quantity z_R is a Rayleigh range [94] defined as kw_0^2 and w_0 is the beam waist width measured between the e^{-1} intensity points.

The field defined by Equations (6.16)-(6.19) can be programmed in COMSOL utilizing five analytic functions and COMSOL internal coordinate variables. Field equation require two additional functions to describe ρ and z in a coordinate system, which moves together with the beam. This system becomes essential when varying the angle of incidence with respect to the grating.

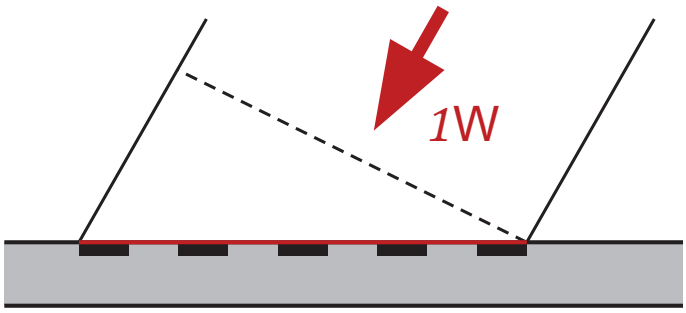

Figure 6.8: Power arriving to the grating. A gaussian beam has the majority of power inside the side walls (black lines).

Variation in the angle of incidence requires tuning of the beam amplitude because the beam has to preserve an input power of 1 W. This power has to be incident on the grating. Integration of power flow over the cross section determined by the grating (Fig. 6.8) results in an equation where the beam amplitude depends on the input power (see Section 6.3.1). This allows to solve the amplitude as a function of the power:

$$E_0 = \sqrt{\frac{2ZP_{in}}{\sqrt{2}w_0L}}\sqrt{\frac{w(z)}{w_0}}\sqrt{\operatorname{erf}\left(\frac{w_g\sin\alpha}{2w_0}\right)^{-1}} \tag{6.20}$$

where $Z = \sqrt{\mu/\epsilon}$ is the impedance of beam propagation medium, erf is the error

function, w_g is the width of the grating and α is the angle of incidence. The error function has no realization in COMSOL 4.2 and 4.3. However, it can be realized using a cubic spline interpolation, which is available in both versions of COMSOL. Previous equation defines the amplitude to match a certain power projected to the grating. This power is independent of the incidence because the amplitude varies with the angle α.

Equation (6.20) is formed with an approximation where the wave front shape remains nearly planar during propagation. Therefore, the input power can be calculated as an integral over planar surface. The approximation is valid when the beam diverges slow enough, and the distance from the waist is short relative to the beam size.

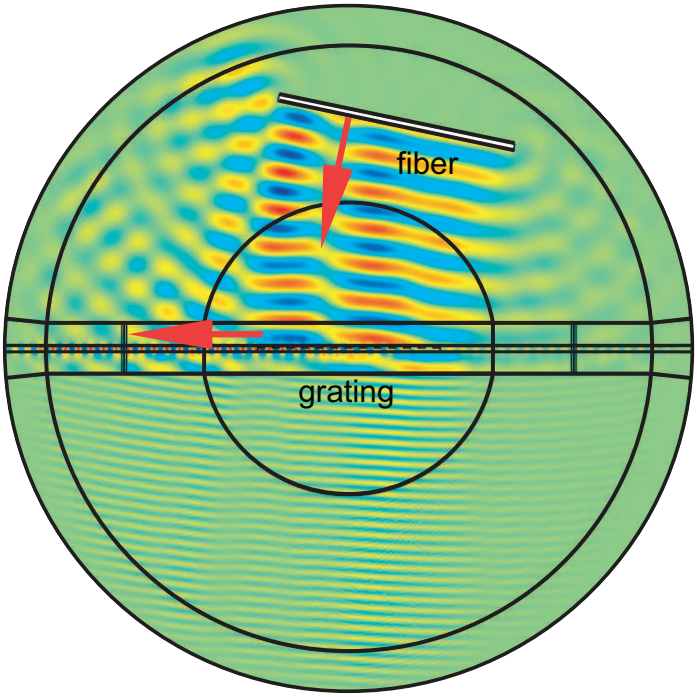

Figure 6.9: Beam excitation model. Input is an electric field boundary with background areas removed from the computational domain. On the back side of the removed domains, electric field is set to zero. The figure describes a 2D-model.

As a whole, the beam excitation has the following realization: the electric field boundary condition induces a Gaussian beam, which passes through the grating midpoint. The beam has an amplitude defined by Eq. (6.20). Therefore, input power of 1 W passes through the grating surface as shown in Fig. 6.8. A fraction of this power is coupled to the waveguide through the grating. Any other coupling, which might be possible is omitted because the grating has the major influence on the coupling. The power reflected by the grating and the transmitted power achieve the absorber on the model boundaries resulting in negligible reflections. The coupled power is obtained from the power flux density integrating over the blue

boundary between two leftmost black points nearest to the waveguide in Fig. 6.3. The boundary is selected to extend one waveguide height in both directions around the waveguide. Therefore, the major contribution to the integral comes from the waveguide modes. These modes pass through the waveguide and get eventually absorbed by the surrounding material. This ensures no back reflections occur that would contribute to the integration. All the simulations can be performed with a single electromagnetic waves-node and frequency domain solver.

6.2.3 Optimization methods

A large scale parameter sweep can be utilized to optimize the grating geometry for maximal coupling. Automatic sweep is necessary because the grating operation depends on many parameters, each of, which has to be taken into account. Hence, the sweep is required to go these parameters through and estimate coupled power for each grating structure. The results for the coupled powers and field distributions have to be saved during the computation. This spares memory required in the simulations and also prevents losing the data if an error occurs during the optimization.

The optimization procedure executes the beam excitation model of the previous section for each parameter combination and stores the power into a text file. The model directly yields the coupled power because of the unit input. While the calculation proceeds, the geometry corresponding to the maximum coupling is either updated or preserved in the memory. In addition, field plots and power values for all the blue boundaries in Fig. 6.3 are stored for each parameter combination. This allows for estimating the reliability of the obtained results.

To distinguish result files from each other, an unique ID number was generated for each geometry. ID is a string of capital letters followed by numbers, for example:

$$\texttt{1A1B1C1D1E2F1G1H1I1J2K1L1M1N1O1P1R1S1T1U1V1W3X1Y1.} \tag{6.21}$$

Here the first number refers to the excitation, each letter corresponds to a simulation parameter and the numbers following the letters correspond to different values of those parameters. For example $A1$ denotes the first simulation value of parameter A. When optimizing the coupled power, the first symbol always has value 1 denoting the beam excitation. These ID numbers are unique for each parameter combination and excitation scheme. Therefore, only one ID number and the corresponding coupling value has to be stored to keep track on the geometry, which yields the maximum power. This ID number can be printed in a file after the simulations. Hence, it becomes possible to filter out the optimal geometry from files, which are named according to IDs.

The grating geometry was modified based on a Gaussian function. Gaussian variables are included in table 6.1. The functional form of the etch width distribution

Table 6.1: Parameters varied during the optimization. The model contains more parameters not included in the optimization.

ID symbol	parameter	values
E	α	[6.1 11.8 17.5] deg
G	w_e	[2 0] μm
J	Λ	[600 630 650] nm
L	d	[70 80 90] nm
X	E_f	$[-1.2 \quad -1.8]$
W	σ	[1 1.4]
V	s	[0 0.2 0.4]
Y	T	[0.5 0.9]

utilized in the grating was obtained through a multiplication of the Gaussian and a Fermi-Dirac type function:

$$F(z) = e^{\frac{(z-s)^2}{2\sigma^2}} \left[1 - \left(e^{\frac{z-E_f}{T}} + 1 \right)^{-1} \right] \tag{6.22}$$

The last four parameters are named according to these functions. The symbols listed in the table represent angle of incidence (α), extra width between the grating and the integration boundaries (W_g), grating period (Λ), etch depth (d), Fermi-function half maximum point (E_f), standard deviation (σ), Gaussian shift (s), and Fermi function smoothness (T). A Gaussian shape shifted to the right (away from the port) is known to yield high coupling efficiency [95]. Therefore, all the swept parameter combinations create an etch width distribution similar to a shifted Gaussian.

COMSOL LiveLink^{TM} for Matlab allows for writing a COMSOL model as a code where Matlab commands can be utilized to process data. In this work, Matlab LiveLink^{TM} was utilized to save the desired power values into text files, to generate field plots during the simulation and to automatically go through the parametric sweep described earlier. LiveLink^{TM} provides commands, which were utilized to plot COMSOL graphics as PNG (portable network graphic) images. Matlab also provides a means to store the maximum geometry in a variable, which is updated for each simulation run. When the simulation sweep is complete, the variable can be used to indicate the optimal geometry for the user. In this work, LiveLink^{TM} produced a "flag file", which contained the automatically generated ID of the optimal geometry. This method enabled fast search for the associated power values and simulation results amongst various sweep geometries.

6.3 Postprocessing

This section describes the methods used to calculate coupled or scattered power, and to estimate the validity of the obtained results. First, power estimation methods are represented in theoretical level, following the realization in COMSOL. Next, different error are listed and their significance is analysed.

6.3.1 Methods for power estimation

Estimation of the coupled power requires information of the electromagnetic fields. Electromagnetic power flux arises from the interactions between the electric and magnetic fields. Thus, it has a definition based on these fields. A quantity called Poynting's vector can be defined as:

$$\mathbf{S} = \frac{1}{2} Re\left\{\mathbf{E}\left(\mathbf{r}\right) \times \mathbf{H}^{*}\left(\mathbf{r}\right)\right\}. \tag{6.23}$$

Equation (6.23) is a basic relation found in many electromagnetic textbooks, such as [96, p. 134] and [47, pp. 52-54]. It produces units of 1 W/m^2 and is proportional to intensity. Integral of power flux defined by Eq. (6.23) yields total power flow through the integration boundary. Power flowing through the surface is given by the equation

$$P = \int_S \mathbf{S} \cdot \mathbf{dS} = \int_S \frac{1}{2} Re\left\{\mathbf{E} \times \mathbf{H}^{*} \cdot \mathbf{dS}\right\}. \tag{6.24}$$

This expression simplifies when $\mathbf{S}$ becomes independent of one or more of the surface coordinates. For example, when $\mathbf{S}$ becomes independent of z-coordinate, integral over a cylindrical surface becomes a product of the cylinder length and a 1D integral over the circumference:

$$\int_S \mathbf{S} \cdot \mathbf{dS} = L \int_c \mathbf{S} \cdot \mathbf{dl}. \tag{6.25}$$

The model shown in Fig. 6.3 has a cylindrical geometry. COMSOL automatically presumes a 2D model to extend 1 m in the out-of-plane direction. Hence, Equation (6.25) can be utilized to estimate coupled or scattered power. The integral is calculated numerically over the blue semicircles of Fig. 6.3. The quantity L is set to 1 m corresponding to the COMSOL standard measure.

Correct value of L is important because the power, which passes through the ports is equal to 1 W. COMSOL presumes the ports to extend 1 m out-of-plane. Therefore, integration has to take into account a length of 1 m, which corresponds to integrating the total coupled or scattered power over the total length of the port boundaries.

The implementation of the integral (5.23) has to be converted into a COMSOL expressions. In COMSOL, user is allowed to specify model couplings below the definitions node of Fig. 6.4. These couplings include integration over a line.

However, Equation (6.25) contains a dot product of two vectors, namely the Poynting's vector and the line normal. Whereas the real electric field is a vector, COMSOL frequency domain solver only computes the components of the vector. Furthermore, as the angles of different scattered waves are unknown, the relation $\mathbf{a}\cdot\mathbf{b} = |\mathbf{a}|\,|\mathbf{b}|\cos\alpha$ cannot be used in the calculation. Therefore, the calculation of the dot product becomes non-trivial.

Dot product of two complex numbers is defined as the realdot-function in COMSOL. This function takes two complex numbers as its parameters and calculates their dot product. For example, if $a = a_r + ia_i$ and $b = b_r + ib_i$, the dot product of a and b is calculated as

$$a \cdot b = a_r b_r + a_i b_i. \tag{6.26}$$

Electric field can be converted into a complex number that enables calculation of a dot product as in Eq. (6.25):

`E`	=	`emw2.Ex + i emw2.Ey`
`n`	=	`nx + i ny`
$\mathbf{S}\cdot\mathbf{dl}$	=	`realdot(E,n)`

where `emw2` refers to the electromagnetic waves physics node in COMSOL. The normal vector is automatically defined for each boundary in COMSOL.

Expression (6.25) can be fed to an integral as a parameter. In COMSOL, power integration can be defined as `intop1(Eq. 6.25)`. Here `intop1` refers to the model coupling, which defines a boundary integration. The value of the integral can be found after the evaluation of the model. It is a global variable in COMSOL.

In the model of Fig. 6.3, the integration boundary can be on any of the blue boundaries marked in the figure. These boundaries are the same as those marked on Fig. 6.10. One integration is calculated over the green (upper) semicircle of Fig. 6.10.

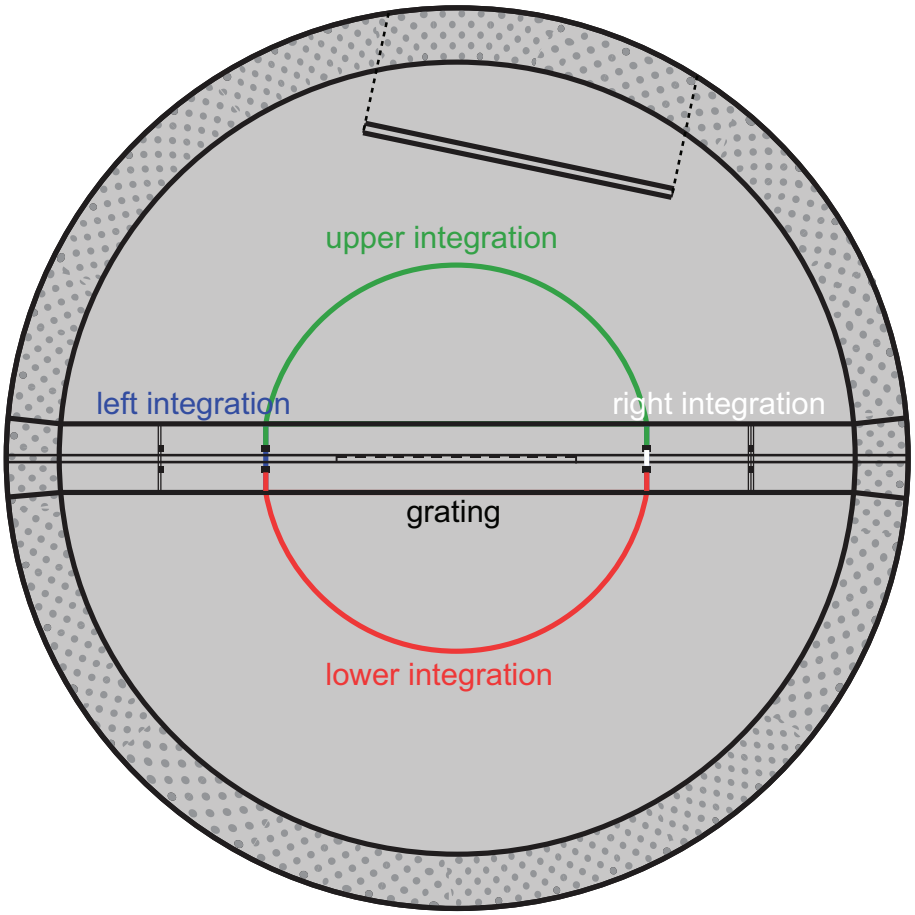

Figure 6.10: Integration boundaries utilized in the power estimation. The figure describes a 2D-model.

Another is calculated over the red (lower) semicircle in analogy. These integrations yield estimates of the up and down scattered powers in the port excitation. However, they also measure total power arriving in the model center and penetrating the waveguide in the beam excitation scheme. Power is also integrated between the black points in the left and right side of the model. In port excitation, integration over the blue (left) boundary yields the waveguide mode total power and integration over the white (right) boundary yields the power, which is transmitted through the grating. For the beam excitation, the same integrations yield the coupled power and power reflected in the waveguide by the grating respectively. In addition, the power can be integrated over the grating surface to ensure the incoming beam power is equal to one watt. This was done when the model was constructed but not in the final simulations. The coupled and scattered powers were directly obtained from the upper and left integrations with 1 W of input power.

After integration, coupling efficiency is obtained directly from the coupled power if 1 W is incident on the grating. Coupling loss can be calculated from the coupled power as $P_{loss} = 1\ \mathrm{W} - P_{cpl}$. However, power flow integration does not reveal the contribution of the field profile mismatch defined by Equation (4.3) in the coupling.

Calculation of Eq. (4.3) is difficult when the electric field has no analytic expression. The fields in a grating coupler are functions of the wavelength and the grating geometry, both of which vary in this study. Therefore, calculating the integral would require automatic interpolation of the unknown fields. However, a simpler approach exist to estimate the field profile mismatch in the coupling.

Comparison of the two excitations represented earlier can reveal the profile mismatch. Such comparison utilizes optical reciprocity principle, which states that the coupling efficiency should remain unaltered when the input and output of the system are exchanged. Hence, equal amounts of power can be transmitted from an optical fiber to a photonic waveguide and from a waveguide to a fiber. The light coupled to the waveguide has lost power due to reflection from the waveguide surface, scattering in opposite direction and transmittance through the waveguide. However, a part of these losses is explained through the mode mismatch. The excitation through the waveguide also experiences losses. However, the light can scatter in any angle and intensity profile with no mode mismatch. Therefore, the power scattered by the grating always exceeds the coupled power. The amount of excess depends on the mode mismatch. This allows for the estimation of the mismatch by calculating the difference of the scattered and coupled power:

$$P_{loss,mm} = P_{sct} - P_{cpl}. \tag{6.27}$$

The expression above follows from the straight definition of the Gaussian beam on the grating surface. As the beam shape is well defined, only the field components, which correspond to the waveguide mode field on the boundaries can couple to the waveguide. The mismatch would disappear if the incoming beam of light would perfectly math the grating output mode.

6.3.2 Error sources and reliability

Several errors may occur due to the numerical modelling. Such errors contain power, which is generated as a result of numerical inaccuracy, non-physical reflection, reflections from model boundaries and errors in input definition. These all were tested to ensure the correct operation of the constructed COMSOL model.

Numerical inaccuracy or noise originates from the finite amount of basis functions utilized in the simulations. Therefore, Maxwell's equations are not satisfied accurately but rather as an average value. Hence, also power conservation may be violated. As FEM (finite element method) aims to minimize the total energy of the computational domain, majority of non-physical power is canceled by opposite effects. However, a small fraction of power remains and is generated in the structures.

This power is stored in electromagnetic fields and it can be estimated by integrating the divergence of Poynting's vector over the computational domain:

$$P_{eff} = \int_D \nabla \cdot \mathbf{S} \mathrm{d}V. \tag{6.28}$$

Any value different from zero indicates the influence of numerical noise because no power is generated in the modelled domains. The values obtained from the integral can cause a few percent errors to the coupled powers.

Non-physical reflections may origin from, at least, three reasons. First, numerical reflections may occur when the mesh density changes rapidly. Second, the absorber utilized in the model causes reflection, because the attenuation is not perfect. Third, a small fraction of scattered power can reach the model boundaries and reflect back towards the interior. However, higher reflection origins from the power, which is directly reflected from the absorber. Here, the reflections occur before the field has experienced considerable attenuation.

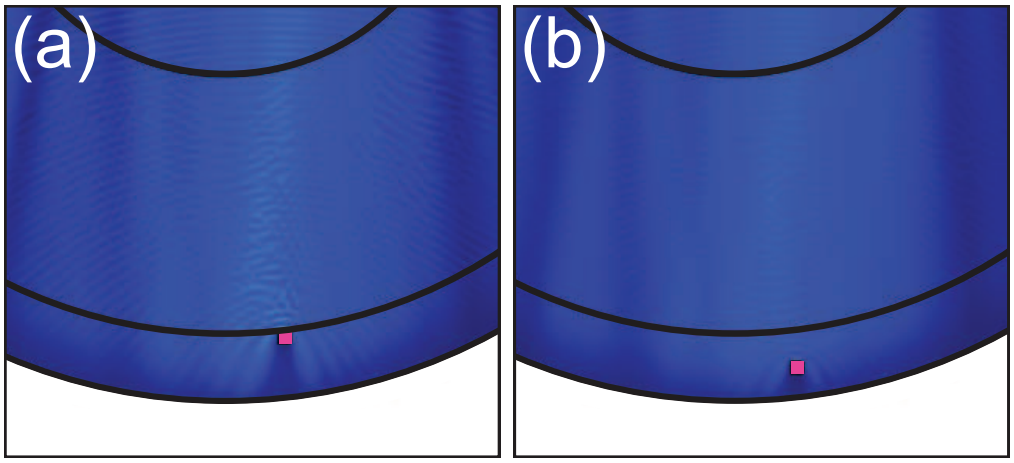

Figure 6.11: Reflection from an ideally conductive square inside the absorber layer. While the distance from the surface increases, the reflection disappears. (A) $d =$ 50 nm, (b) $d = 850$ nm. The figure describes a 2D-model.

Numerical reflections can be avoided by creating a slowly varying mesh. This becomes particularly important near the absorber because numerical reflections carry power away from the absorber. Therefore, a mapped mesh, shown in Appendix C, was utilized in the absorber domains. A mapped mesh has rectilinear elements, which remain constant through the mesh.

The power could reflect from the model boundaries if no absorber were implemented in the model. This power would then contribute to the integration. Such contribution would cause error in the estimated scattered power. COMSOL provides perfectly matched layers (PMLs) to avoid this problem. PML is a material, which

absorbs all the incoming radiation. Such material can be a superposition of several anisotropic components or through a coordinate transform [98]. COMSOL utilizes a coordinate transform, which automatically results in high absorption for any thickness of the layer. The PML equation of COMSOL maps the coordinates t to the complex plane [97, p. 34]:

$$t^{'} = \left(\frac{t}{\delta_w}\right)^n (1-i)\,\lambda F, \tag{6.29}$$

which can be written as

$$t^{'} = 2\pi \left[\left(\frac{t}{\delta_w}\right)^n F - i\left(\frac{t}{\delta_w}\right)^n F\right] \frac{\lambda}{2\pi}. \tag{6.30}$$

When inserted in electric field phasor presentation, these equation give attenuating field because

$$\exp\left[-ik_t t^{'}\right] = \exp\left[-i\frac{2\pi}{\lambda}\sin\theta_t t^{'}\right] \sim \exp\left[-2\pi\left(\frac{t}{\delta_w}\right)^n F\sin\theta_t\right] \tag{6.31}$$

These equations show that the attenuation is independent of wavelength and because the coordinate t is divided by the layer thickness, PML has equal attenuation for any thickness of the layer. The values n and F are called the order and the scaling factor of the PML [97, p. 34]. They tune the PML scaling according to the problem at hand.

It might appear that PML is an ideal boundary condition when studying scattering over wide bandwidths and utilizing large scale model in the study. However, as shown in Appendix B, PML layers do not produce reliable results when PML layer is composed of more than one material. This situation is met when studying photonic waveguides, because the waveguide divides the computational domain in two halves. Hence, similar operation has to be achieved by other means. Slowly varying refractive index offers one alternative because smooth variation of the index combined with absorption results in a low reflectivity. In this work, the absorber in Fig. 6.3 was realized as a material with a refractive index defined as:

$$n\left(\rho\right) = n_i - i\frac{\rho-\rho_0}{\delta_w}. \tag{6.32}$$

This equation can be combined with the phasor presentation:

$$\exp\left[-in\left(\rho\right)\mathbf{k}\cdot\boldsymbol{\rho}\right]\sim\exp\left[-\frac{\rho-\rho_0}{\delta_w}\mathbf{k}\cdot\boldsymbol{\rho}\right]. \tag{6.33}$$

Equation (6.33) is analogous to Equation (6.31) when n is set to 2 and δ_w is selected correspondingly. A plane wave propagating in a direction $\boldsymbol{\rho}$ experiences attenuation, which depends quadratically of the distance from the absorber inner boundary shown in Fig. 6.3. The major difference between Equations (6.33) and (6.31) is their wavelength dependency. As k is inversely proportional to wavelength, Equation (6.33) produces attenuation, which changes as a function of the wavelength. However, the studied wavelengths lie near each other in this study and the wavelength dependent absorption becomes insignificant.

The reflections caused by the absorber are always present. However, with adequately smooth variation of the refractive index, reflection can be limited to practically insignificant value. The operation of the absorbing layer can be tested by inserting an ideally conductive block inside the absorber. Reflections from such an object show as parabolic wavefronts in the electric field norm plots. The figure 6.11 shows that the reflection disappears when the block is moved far enough under the surface.

The errors in input definition can arise from inaccurate electric field expressions. These expressions are associated to selected boundaries of the simulation model. These boundaries have finite size resulting in cutting of the field on the edges.

Effect of the cutting of the excitation fields varies between the excitation types. Cutting has practically no impact to the beam excitation scheme because the fields in an optical fiber are well confined inside the fiber. However, in the port excitation, the exponential tails of the waveguide mode are cut on the edges of the input boundary. This leads to a discontinuous electric field expression, which does not exactly correspond to the waveguide mode. To reduce this effect, the waveguide input boundary has to extend an adequate width around the waveguide. Such width can be, for example, two times the waveguide core thickness.

7 Results and discussion

The motivation for this study was to optimize the coupling at 1.55 μm wavelength. Coupled power can be obtained directly from power integration when a Gaussian beam is focused on the grating. Different geometries of the compared structures also lead to different coupling characteristics. These characteristics are tunable by altering the grating element profile.

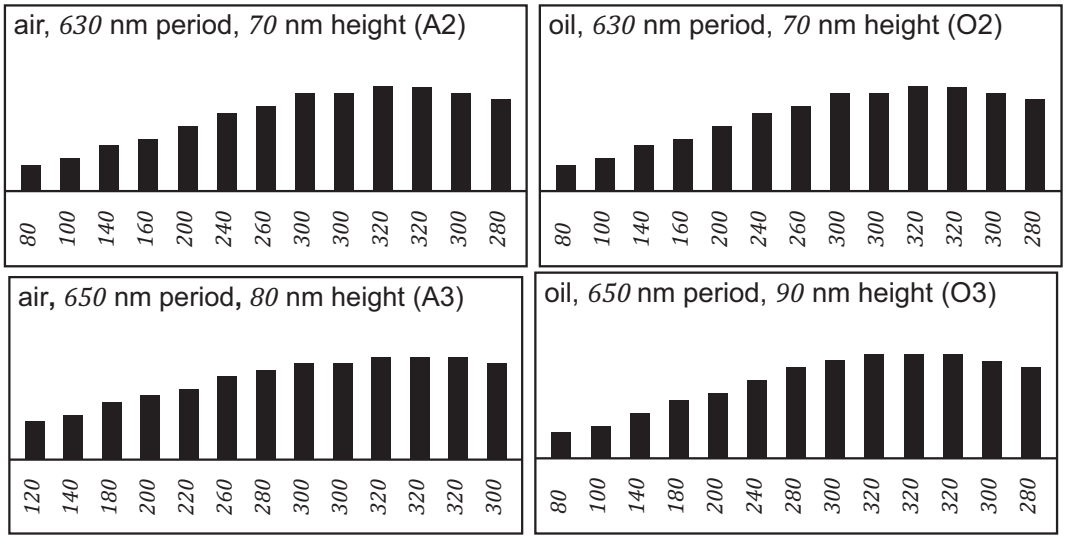

Figure 7.1: Optimized grating geometries for air and oil above the waveguide. The optimization produced geometries for fixed period of 630 nm and maximum etch depth of 70 nm, which are typical parameters utilized at 1.55 μm wavelength. In addition, the overall maximum was calculated for both cases. This corresponds 80 nm etch depth for air and 90 nm depth for oil.

As mentioned in Chapter 5, refractive indices around a grating affect its scattering properties. This can be utilized to boost the coupling between the grating and an optical fiber. Maximum power exchange with the studied structures can be achieved when the optimized geometry is adjusted for index matching oil above the grating. The obtained geometry slightly deviates from the optimized geometry obtained for air cover material.

Each branch of the parameter tree in Fig. 6.5 corresponds to a different grating geometry and excitation configuration. The optimization procedure generates etch width distributions for air and oil based geometries. These distributions show significant differences when compared to the initial distribution with 70 nm etch depth and uniform 630 nm etch width.

From now on, the studied distributions are named as geometries $A1-3$ and $O1-3$ where A denotes air, O denotes oil and numbers $1-4$ denote the degree of optimization, 3 being the structure corresponding to highest coupling. Indices 2

and 3 are reserved for gratings with asymmetric distribution. The distributions are shown in Fig. 7.1.

7.1 Frequency responses for the port excitation

Geometries A1 − 2 and O1 − 2 can be compared to each other. Structures A1 and O1 represent uniform gratings and are different from geometries A2 and O2. Asymmetric element distribution generally leads to lower scattering values because scattering by a single grating element is proportional to element size. In this study, grating elements have a maximum width of half period resulting in higher number of large elements for uniform distributions.

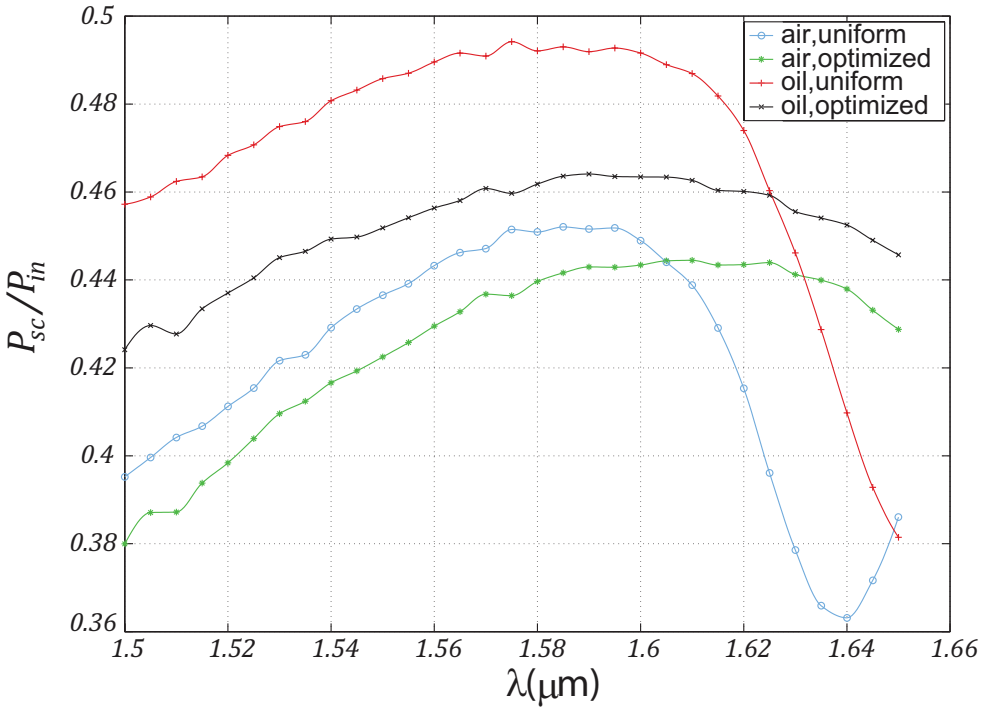

Figure 7.2: Normalized scattered powers for the air and oil based geometries. The figure shows frequency responses for the initial and optimized geometries.

Figure 7.2 shows how the frequency response changes when asymmetric profile is implemented. After approximately 1.61 μm wavelength, a dip occurs where the scattering power is significantly reduced. The drop of power occurs considerably faster for the initial geometries A1 and O1. Optimized geometries (A2 and O2) also scatter less, but the slope of the curve is significantly smaller.

The reduced scattering is known to occur due to reflection back to the waveguide [49]. As a waveguide mode passes the grating, mode wave fronts encounter grating elements causing the reflection. This reflection depends on the refractive index contrast

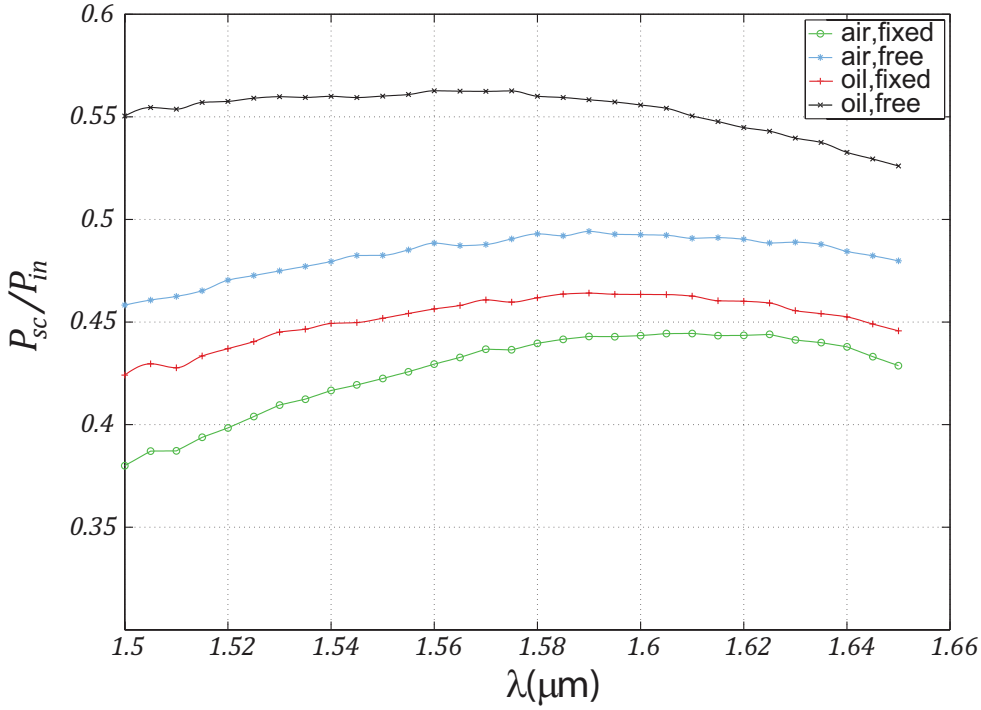

Figure 7.3: Scattering curves for geometries with fixed and free dimensional parameters. When parameters are selected freely, optimization procedure finds the geometries with optimum performance.

at the grating. Such discontinuity has to be considered in terms of the effective index described in Section 6.2. The effective refractive index can be interpreted as an approximate average of the indices surrounding the waveguide. A grating alters the effective index because the waveguide width varies periodically at the grating elements. Gradual increase in etch size leads to gradually decreasing effective index in contrast to an instant change caused by uniform grating. Therefore, optimized geometries should have lower back reflection and significantly lower drop in the scattered power.

Maximum scattering occurs near 1.6 μm for all the compared geometries. However, the wavelengths of maximum and minimum scattering slightly vary across different geometries. Here, optimization and index matching oil seem to have similar influence. When the coupling is enhanced, the scattering curve is shifted to the right. In other words, the maximum and minimum scattering occur at higher wavelengths.

Shift of the maximum may occur because the grating optical size is increased in both cases. O geometries have a higher refractive index than A geometries leading to higher effective mode index. Similarly, the gradual change of effective index for the optimized geometries results in optically larger structure.

Figure 7.4 was obtained fixing the parameters $\Lambda = 630$ nm, and $d_{max} = 70$ nm.

Therefore, the optimization does not return the geometry with the highest possible coupling. The results shown in the figure matter because limitations of typical grating manufacture lead to geometries, which are not necessarily optimal. Geometries A3 and O3 ore obtained when these requirements are loosened. Figure 7.5 compares the fixed optimization results to the results obtained with free parameters. Geometries with free parameters scatter more power for both cover media.

7.2 Frequency responses for the beam excitation

As the grating structures were optimized with respect to coupling, the optimized geometries are expected to have higher power values at 1.55 µm. The enhanced coupling values can be explained by improved mode overlap, expressed by integral (2.4). This overlap accounts for the case when a Gaussian beam irradiates the grating.

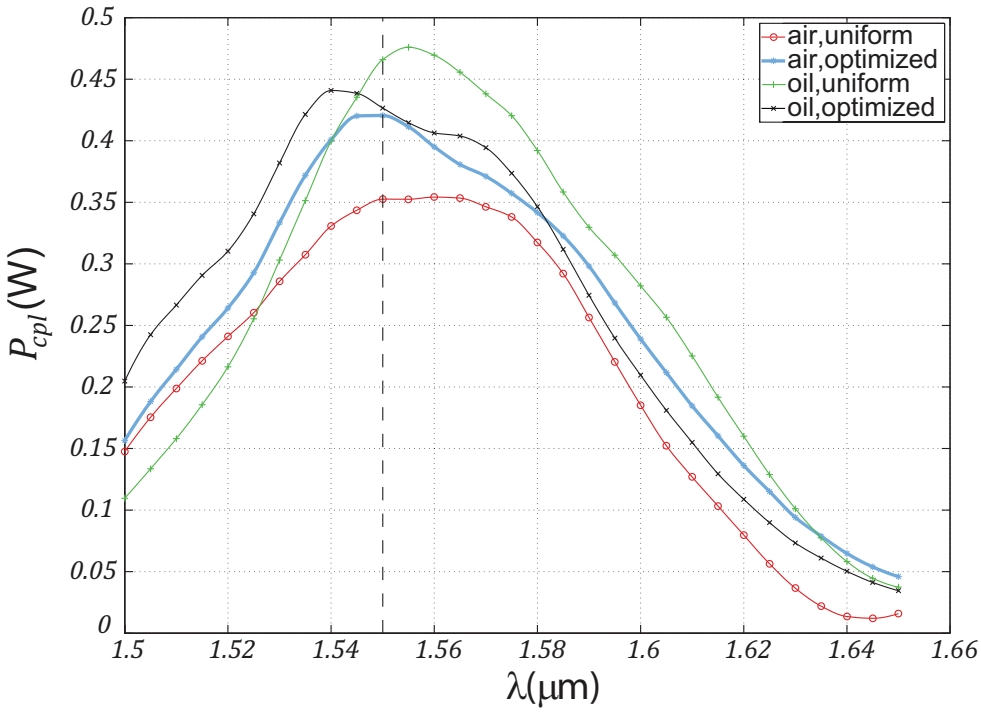

Figure 7.4: Coupled powers for the initial geometry and the optimized geometries with $\Lambda = 630$ nm and $d_{max} = 70$ nm.

As shown in Fig. 7.4, the optimization produces desired results for A geometries. However, the parametric sweep cannot find an optimized geometry for index matching oil. Instead, coupling at 1.55 µm is reduced when applying an etch width distribution. Therefore, higher coupling requires changing the period and maximum etch depth of a grating element.

The coupling curves of Fig. 7.5 show that free optimization parameters lead to enhanced coupling compared to the fixed parameters. This occurs in all cases. The greatest improvement occurs for the oil based geometry O2, where the maximum coupling can be improved by 0.14 % of the input power. With this improvement, geometry O3 exceeds O1 in maximum coupling efficiency. Air geometry also has these improvements but they are not as high as for the oil geometry when compared to the fixed case.

The maximum coupling occurs at a certain angle for each geometry. Different aspect ratio leads to different angle of diffraction. Hence, the angle is approximately 11.8 ° when operating with oil and 17.5 ° when having air above the grating . However, these angles are different for each distribution. These distributions contain geometries with different periods because the phase matching condition only depends on the matching of the wavenumber longitudinal component with the grating period. This, furthermore, determines the angle of maximal coupling as it determines the wave vector components.

The −3 dB bandwidths for the frequency responses of Fig. 7.4 are around 90 nm. Geometries A1 and A2 have an approximate bandwidth of 95 nm, whereas O1 produces a narrower peak of 85 nm and O2 has a bandwidth of 96 nm. Figure 7.5 shows that the optimized geometry $O3$ has broader bandwidth than O1. This becomes desirable when designing wide band applications. However, the bandwidth for O3 geometry is 97 nm, which only deviates by 0.2 % from the initial case.

Table 7.1: Maximum values of the coupled and scattered powers and −3 dB bandwidths for various grating designs.

Geometry	Scattering (%)	Coupling (W)	−3 dB bandwidth (nm)
Air,initial	0.45	0.35	95
Air,optimized	0.44	0.42	95
Oil,initial	0.49	0.48	85
Oil,optimized	0.46	0.44	96
Air,free parameters	0.49	0.49	94
Oil,free parameters	0.56	0.56	97

In summary, limitations in parameter range prevent perfect optimization of the structures. The studied parameters include period (Λ) and maximum etch depth (d_{max}), which were fixed in earlier simulations. When these parameters are allowed to change more freely (increasing the range), optimization can find parameter combinations, which yield improved coupling. Table 7.1 shows good agreement with the theoretical 49 % coupling limit for uniform grating geometries and results published in [49], [99, Table 1], and [100, ch. 2.2].

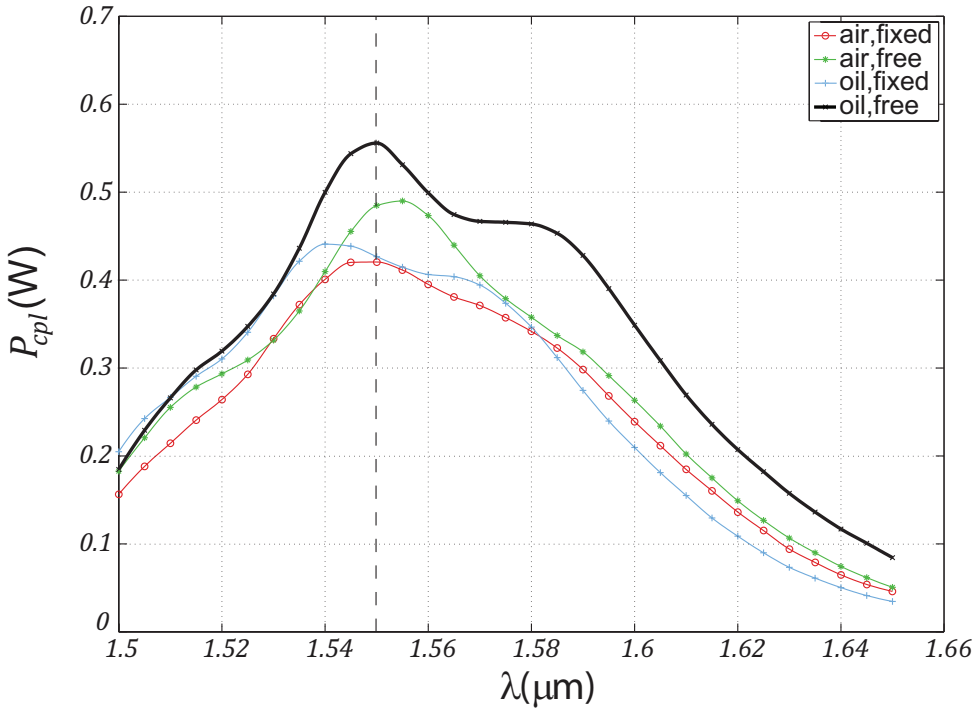

Figure 7.5: Coupled powers for fixed and free optimization geometries. The coupling is significantly enhanced when utilizing free optimization parameters.

7.3 Comparison of the frequency responses

Previous sections show that more power is scattered than is coupled for all cases. This is natural because only a fraction of the scattered power can couple to the fiber. If the mode mismatch were zero, all the scattered power would be coupled yielding equal scattering and coupling efficiencies. However, the scattered power profile does not perfectly match the fundamental fiber mode. On the other hand, a Gaussian beam cannot produce illumination on the grating surface, which would perfectly correspond to illumination provided by the fundamental waveguide mode. Hence, losses occur in coupling and coupling figures are lower than scattered powers by the grating.

The difference between the coupled and scattered power indicates the amount of power lost due to the mode mismatch. This difference is reduced by the optimization, as shown in Fig. 7.6. The figure only shows the frequency responses for A1 and A2 geometries but the same phenomenon is repeated for all studied structures. This can be seen by calculating the differences from the frequency responses and comparing the results with each other.

Table 7.2 shows the loss estimations for all the studied structures. When the air geometry is optimized, the loss is reduced to a level, which is lower than the accuracy

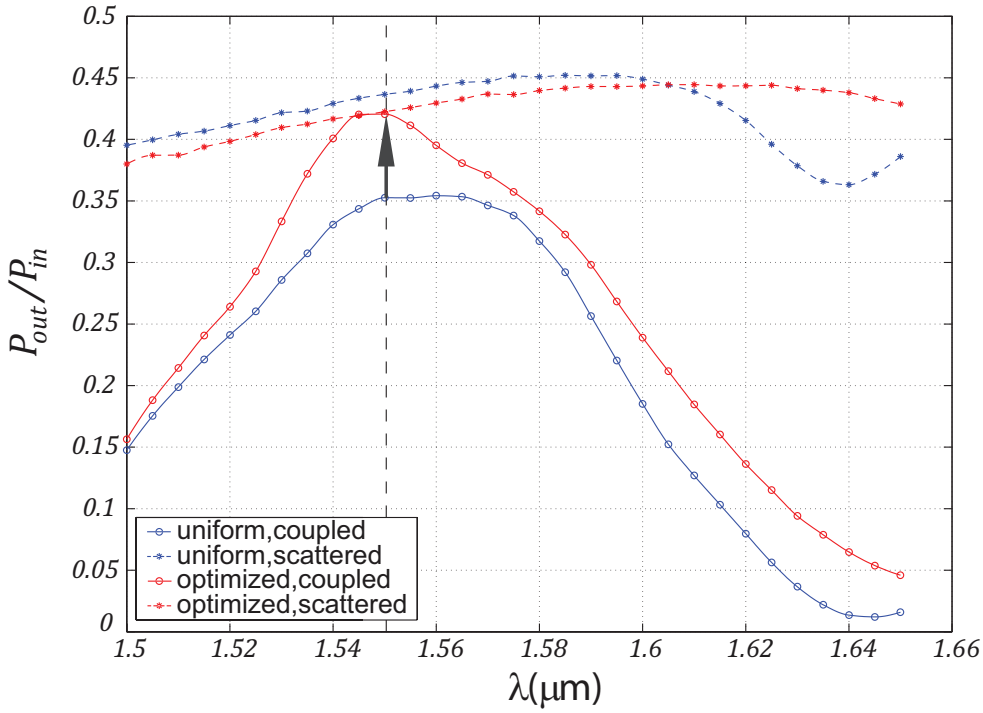

Figure 7.6: Coupled and scattered powers for the fixed air geometries. The black arrow shows the improvement in coupling while scattered power remains approximately unaltered.

Table 7.2: Estimated coupling losses of the studied geometries. The percentages are calculated from the input power.

Geometry	Loss at 1.55 μm (%)	Maximum loss (%)
Air,initial	0.084	0.090
Air,optimized	0.002	0.016
Oil,initial	0.020	0.011
Oil,optimized	0.025	0.008
Air,free parameters	> 0	> 0
Oil,free parameters	0.004	0.004

of representation. Therefore, the loss values for the optimized air geometry are shown to be larger than zero indicating the existence of losses.

The scattered electric field norm can be plot for an initial and an optimized geometry to visualize the electric field mismatch behind the coupling loss. The difference becomes evident when the compared structures have coupling efficiencies maximally far from each other. Therefore, the comparison should contain the geometries with the highest and lowest coupling losses. A1 and O3 geometries represent these ex-

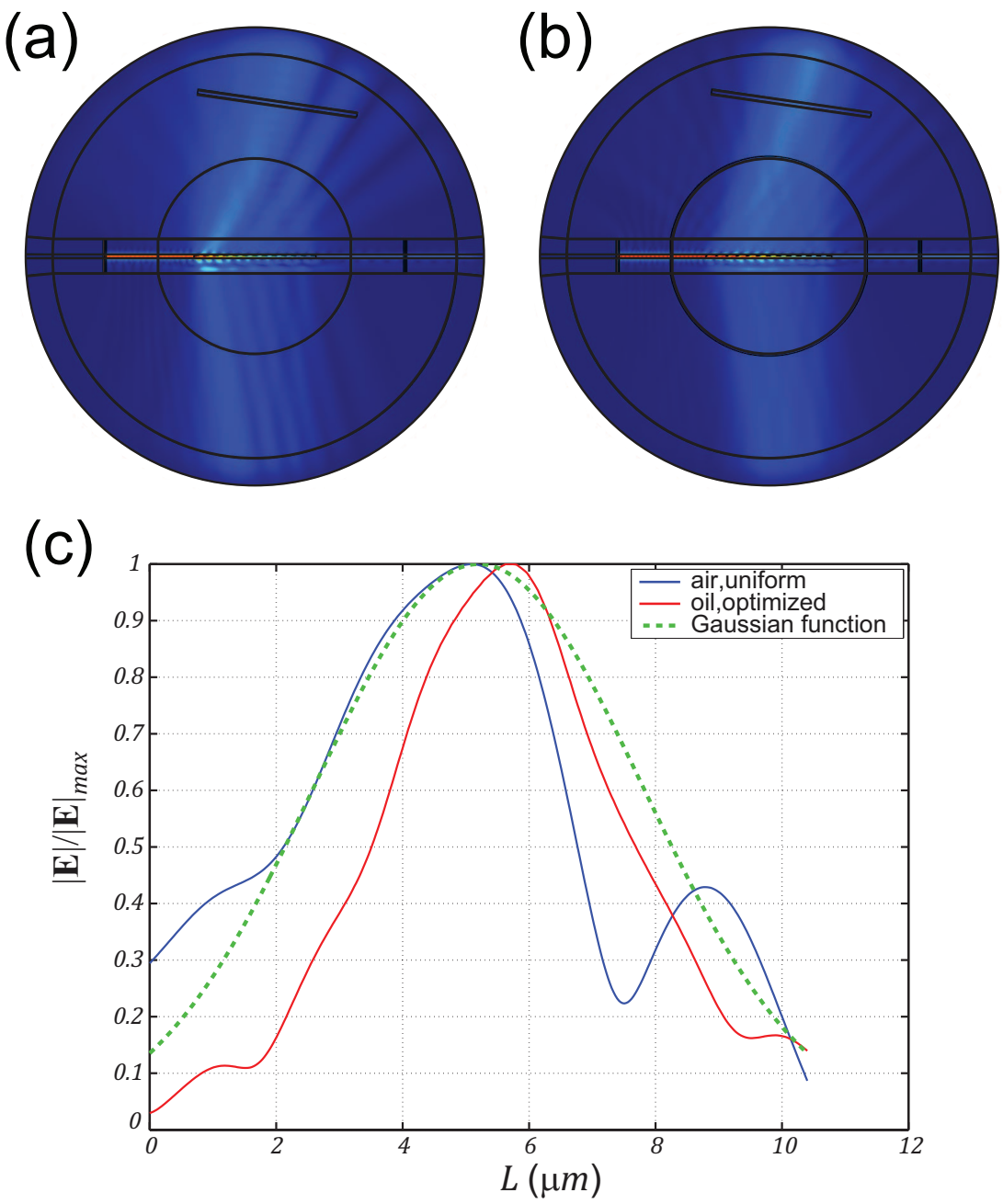

Figure 7.7: Comparison of the A1 and O3 output field distributions. (A) and (b) show electric field norm for these structures respectively. (C) represents plots of the same field distributions on the fiber facet shown in (a) and (b). The fiber was aligned with an 8.3 ° angle. The figure describes a 2D-model.

treme cases in this study. Fig. 7.7 shows the electric field norm as a 1D plot and projected on the fiber facet.

7.4 Future work

Only a small fraction of grating coupling phenomenon was studied in this work. This thesis covers coupling between a shallow etched SOI (silicon on insulator) grating and a standard single mode fiber. It only considers TE-polarization (transverse electric field) on the optical C-band (conventional band) around 1.55 μm. Therefore, some fundamental aspects of optimal coupling remain unstudied.

First, the model constucted here is a two dimensional approximation, which enables high speed computation. This approximation is valid and supported by several articles [45], [89], [27], [1, pp. 47]. However, a three dimensional simulations may produce more accurate results and provide some information of the grating behaviour that is not achievable by a 2D model.

The Gaussian input beam in this model obeys a two dimensional formula. In three dimensional picture this beam represents a cylindrically spreading wave generated, for example, by a slit, because power is not propagating of the plane. In reality, photonic grating structures are generally excited by three dimensional beams that spread in all spatial directions. These beams can be realized in a 3D model.

In all simulations, the divergence of the Gaussian beam could be neglected. This would not be the case if the distance between the optical fiber and the grating was considerably longer than 10 μm. In long distances, the divergence shapes the wavefront, which cannot be treated as planar. Therefore, many of the formulas and assumptions used in this study become invalid. Hence, study of the divergence would improve the understanding of the coupling.

Furthermore, other excitation fields can be tried instead of Gaussian beams. Plane wave excitation may reveal some theoretical aspects of the studied grating couplers. On the other hand, the excitation could arise from a particular field distribution on an aperture. This type of excitation could have, for example, a sinc-function shaped electric field profile [63, pp. 465].

Grating couplers operate differently for different polarizations. Hence, TM-polarized (transverse magnetic field) input may provide higher coupling values than those reported in this study. If the other polarization has higher coupling efficiency, it has to determine the upper bound for coupling of mixed polarization light. Therefore, some uncertainty remains in the validity of the true optimality of the O3 geometry.

Polarization has to be considered particularly when the input beam has a component, which is perpendicular to the waveguide plane. Such a component would make the field polarization mixed. Three dimensional Gaussian beams have two polarization components that may affect on the coupling [65, ch. 3.2.3].

The frequency dependence of the index matching oil refractive index was not considered in this study. However, almost all materials show some type of dispersion over characteristic range of frequencies. The simulation models created in this thesis

could be improved by taking this dispersion into account. However, as the obtained results were near to the reference values,the oil dispersion probably causes only small correction to the results.

The refractive index of the oil could be altered as a parametric sweep to find the optimal value for the coupling. For all the other parameters, higher coupling values could be found if the parameter ranges were swept over longer intervals. Adding parameters and utilizing three dimensional model would require running the simulation in a cluster or in a distributed network of computers. However, COMSOL only supports the first alternative. This produces a need for analytical optimization methods.

Finally, this thesis does not represent methods for estimating the angle of maximal coupling. The phase matching formula only yields rough approximation of the angle due to complexity of the real coupling situation. Methods for angle estimation would highly benefit grating design because the gratings could be designed according to desired angle. Automated angle estimation could be based on utilizing the existing database of simulated grating structures and their associated angles. This database could be utilized together with theory to predict the angle of coupling in some accuracy.

8 Conclusions

In this study, two different excitations were compared for six different photonic grating geometries and two cover materials. The goal of the study was to compare the frequency responses obtained through simulation and to optimize the grating structure through the simulated element distribution. This required construction of a working numerical model in COMSOL Multiphysics. This software was selected because it supports fast calculation and automatic simulation process.

The proper selection of the grating element distribution was found to enhance the performance over the whole studied frequency range. In this study, a spectral range around 1.55 µm communication wavelength was selected, which is typically used in grating couplers. The performance was measured with respect to coupling to a SOI (silicon on insulator) channel waveguide. The frequency responses of all the studied structures were compared to determine the most optimized structure for the coupling. As a result of the optimization, the coupling efficiency of the input power could be improved by more than 10 % of the input, compared to the initial structures. Therefore, the grating geometry was successfully optimized on the selected band.

The optimum geometry involved the use of an index matching oil with a refractive index of 1.45 as a cover material. The optimization process was based on tuning the grating element dimensions and calculating the in-coupled power. The resulting geometry has an asymmetric element distribution. This distribution resembles a shifted Gaussian, as predicted by the grating theory. All the obtained coupling and scattering figures were similar to those mentioned for similar structures in other publications. In contrast, scattering directions, which were measured with respect to the grating normal, deviated several degrees upwards from the reference values.

The numerical models developed in this study utilize techniques which can be generalized for some other problems. Particularly, these techniques include solving of scattering problems where the computational domain is divided to two half spaces with different materials. As traditional PML (perfectly matched layer) fails to handle such models, the approach used in this work may provide a solution to model complex scattering objects, which are located in proximity of a material interface.

The models represented here can be improved by more accurate description of the studied structures. The structures can be modelled in three dimension with more realistic excitation field. Furthermore, the material dispersion of the index matching oil can be taken into account. These improvements and modelling the grating structures with TM-polarization (transverse magnetic field) would give more realistic insight into the grating behaviour. However, this insight would require more computational power and time compared to the amounts that were available for this work.

References

[1] Galán, J. Addressing Fiber-to-Chip Coupling Issues in Silicon Photonics. Ph.D. Thesis, Universidad Politécnica de Valencia, Departamento de Comunicaciones, Valencia, 2010.

[2] Pal, G. *Textbook of Practical Physiology.* Chennai, IN, Orient Longman Private Limited, 2001.

[3] RP Photonics Encyclopedia AB. Optical Fiber Communicationss. Web-document. Updated 2013. Referred 16.12.2013. Available: http://www.rp-photonics.comoptical_fiber_communications.html.

[4] Heck, M., Bauters, J., Davenport, M. *et al.* US. Government. *Hybrid Silicon Photonic Integrated Circuit Technology*.

[5] Miller, D. Device Requirements for Optical Interconnects to Silicon Chips. *Proceedings of The IEEE*, 2009, vol. 97, pp. 1166–1185.

[6] Baehr-Jones, T., Pinquet, T., Guo-Qiang, P. *et al.* Myths and rumours of silicon photonics. *Nature Photonics*, 2012, vol. 6, pp. 206–208.

[7] Kotura. Home. Web-document. Updated 2013. Referred 15.12.2013. Available: http://www.kotura.com/

[8] Luxtera. Home. Web-document. Updated 2013. Referred 15.12.2013. Available: http://www.luxtera.com/

[9] Jalali, B., Fathpour, S. Silicon photonics. *Journal of Lightwave Technology*, 2006, vol. 24, no 12, pp. 4600–4615.

[10] Wolfe, J. The Race for Photon Supremacy, in Silicon. *Forbes*, Web-magazine, March, 2012. Referred 09.10.2013. Available: http://www.forbes.com/sites/joshwolfe/2012/03/02/the-race-for-photon-supremacy-in-silicon/.

[11] Okamoto, K. *Fundamentals of Optical Waveguides*. US, Elsevier, 2006.

[12] Ibach, H., Lüth, H. *Solid State Physics*. 4th ed. London, Springer, 2007.

[13] Franssila, S. *Introduction to Microfabrication*. 2nd ed. Chichester, UK, Wiley, 2010.

[14] Schroder, D., Thomas, R., Swartz, J. Free Carrier Absorption in Silicon. *IEEE Journal of Solid-State Circuits*, 1978, vol. 13, pp. 180–187.

[15] Saleh, B., Teich, M. *Fundamentals of Photonics*. 2nd ed. New Jersey, Wiley, 2007.

[16] International Telecommunication Union (ITU). *Optical fibres cables and systems*. Geneva, CH, ITU, 2009.

[17] Djurišić, A., Li, E. Modeling the index of refraction of insulating solids with a modified Lorentz oscillator model. *Applied Optics*, 1998, vol. 37, pp. 5291–5297.

[18] NextGenLog. Europe Focuses Fiber Optics on Silicon Photonics. Web-document. Updated 2010. Referred 16.02.2014. Available: http://nextgenlog.blogspot.fi/2010/09/europe-focuses-fiber-optics-on-silicon.html

[19] Lindsley, K. Light Speed. Web-document. Updated April 2001. Referred 27.9.2013. Available: http://www.rit.edu/research/other_story.php?id=54.

[20] Mekis, A. Silicon Photonics, Lighting Up The Chip. *Nature Photonics*, 2008, vol. 2, pp. 389–390.

[21] Gu, T., Petrone, N., McMillan, J., *et al.* Regenerative oscillation and four-wave mixing in graphene optoelectronics. *Nature Photonics*, 2012, vol. 6, pp. 554–559.

[22] Imec News. Imec offers Fully Integrated Silicon Photonics Platform in a Multi-Project Wafer Service. Web-document. Updated 2014. Referred 16.02.2014. Available: http://www2.imec.be/be_en/press/imec-news/photonics2013.html

[23] Ihp-microelectronics. Technology Solutions. Web-document. Updated 2014. Referred 16.02.2014. Available: http://www.ihp-microelectronics.com/en/solutions/technology-solutions.html

[24] Foster, M., Turner, A., Sharping, J. *et al.* Broad-band optical parametric gain on a silicon photonic chip. *Nature*, 2006, vol. 441, pp. 960–963.

[25] Silicon Photonics Summer School. Rationale. Web-document. Updated 2013. Referred 16.02.2014. Available: http://www.st-andrews.ac.uk/microphotonics/spschool/

[26] NextGenLog. Silicon Photonics Uses Vapor-Filled Waveguide. Web-document. Updated 2010. Referred 16.02.2014. Available: http://nextgenlog.blogspot.fi/2010/09/silicon-photonics-uses-vapor-filled.html

[27] Schmid, B., Petrov, A., Eich, M. Optimized Grating Coupler With Fully Etched Slots. *Optics Express*, 2009, vol. 17, pp. 11066–11076.

[28] Dumon, P., Bogaerts, W., Wiaux, V., *et al.* Low-Loss SOI Photonic Wires and Ring Resonators Fabricated With Deep UV Lithography. *IEEE Photonics Technology Letters*, 2004, vol. 16, pp. 1328–1330.

[29] Montalbo, T. Fiber to Waveguide Couplers for Silicon Photonics. M.Sc. Thesis, Massachusetts Institute of Technology, Departament of Materials Science and Engineering, Massachusetts, 2004.

[30] Neumann, E. *Single-Mode Fibers*. Berlin, Springer, 1988.

[31] Pavesi, L., Lockwood, D. *Silicon Photonics*. Berlin, Springer, 2004.

[32] Haisheng, R., Richard, J., Ansheng, L. *et al.* A continuous-wave Raman silicon laser. *Letters to Nature*, 2005, vol. 433, pp. 725–727.

[33] Claps, R., Raqhunatan, V., Dimitropoulos, D. *et al.* Influence of nonlinear scattering on Raman amplification in silicon waveguides. *Optics Express*, 2004, vol. 12, no 12, pp. 2774–2780.

[34] Soref, R, Friedman, L. "Silicon-based strain-symmetrized Ge-Si quantum lasers". US Patent 6154475, 28 November 2000.

[35] Geo.Arizona.edu. Lecture 12. Web-document. Updated 2013. Referred 17.02.2014. Available: http://www.geo.arizona.edu/xtal/geos306/fall13-12.htm

[36] Takashi, A., Yoshinobu, A., Susumu, N. High efficiency blazed grating couplers. *Applied Physics Letters*, 1976, vol. 29, pp. 303–304.

[37] Sheppard, C., Iaosong, G. Free-space propagation of femto-second light pulses. *Optics Communications*, 1997, vol. 133, pp. 1–6.

[38] Juarez, J., Dwivedi, A., Hammons, R. *et al.* Free-space Optical Communications for Next-Generation Military Networks. *IEEE Communications Magazine*, 2006, pp. 46–51.

[39] Räisänen, A., Lehto. A. *Radiotekniikan perusteet*. 13th ed. Helsinki, Otatieto, 2011.

[40] Gardes, F., Reed, G., Knights, A. *et al.* Sub-micron optical waveguides for silicon photonics formed via the Local Oxidation of Silicon (LOCOS). *Proc. SPIE*, 2008, vol. 6898.

[41] Abbate, G., Castaldo, F., De Stefano, L. *et al.* Analysis of modal coupling between glassy and liquid crystal planar waveguides. *Optics Communications*, 1993, vol. 97, pp. 173–177.

[42] Xiaoming, J., Liwei, C., Jianxin, C. *et al.* High power slab-coupled waveguide laser. *Proc. SPIE*, 2006, vol. 6343.

[43] Gibson, R., Kvavle, J., Selfridge, R. *et al.* Improved sensing performance of D-fiber/planar waveguide couplers. *Optics Express*, 2007, vol. 15, pp. 2139–2144.

[44] Gibson, R., Selfridge, R., Schultz, S. Electric field sensor array from cavity resonance between optical D-fiber and multiple slab waveguides. *Proc. of SPIE*, 2009, vol. 7293.

[45] Taillaert, D., Bienstman, P., Boets. R. Compact efficient broadband grating coupler for silicon-on-insulator waveguides. *Optics Letters*, 2004, vol. 29, pp. 2749–2751.

[46] RP Photonics Encyclopedia AB. Planar Waveguides. Web-document. Updated 2013. Referred 27.11.2013. Available: http://www.rp-photonics.com/planar_waveguides.html.

[47] Sihvola, A., Lindell, I. *Sähkömagneettinen Kenttäteoria*. 5th ed. Helsinki, Otatieto, 1996.

[48] Tao, S., Wang, B., Burr, G., *et al.* Diffraction Efficiency of Volume Gratings With Finite Size: Corrected Analytical Solution. *Journal of Modern Optics*, 2004, vol. 51, pp. 1115–1122.

[49] Taillaert, D., Van Laere, F., Ayre, M. *et al.* Grating Couplers for Coupling between Optical Fibers and Nanophotonic Waveguides. *Japanese Journal of Applied Physics*, 2006, vol. 45, pp. 6071–6077.

[50] Wikipedia, The Free Encyclopedia. Prism Coupler With Incident Beam. Web-document. Updated 2011. Referred 16.02.2014. Available: http://en.wikipedia.org/wiki/File:Prism_Coupler_with_incident_beam.png

[51] Tien, P., Ulrich, R., Martin, R. Modes of Propagating Optical Light Waves in Thin Deposited Semiconductor Films. *Applied Physics Letters*, 1969, vol. 14, pp. 290–294.

[52] Pasmooij, W., Mandersloot, A., Smit, M. Prism-Coupling of Light into Narrow Planar Optical Waveguides. *Journal of Lightwave Technology*, 1989, vol. 7, pp. 175–180.

[53] Pan, Y., Chang, R. Highly efficient prism coupling to whispering gallery modes of a square cavity. *Applied Physics Letters*, 2003, vol. 82, pp. 486–489.

[54] Okamoto, T., Yamoto, M., Yamaguchi, I. Optical waveguide absorption sensor using a single coupling prism. *Applied Physics Letters*, 2000, vol. 17, pp. 1880–1886.

[55] Shoji, T., Tsuchizawa, T., Watanabe, T., *et al.* Low Loss Mode Size Converter from 0.3 μm Square *Si* Wire Waveguides to Singlemode Fiber. *Electronics Letters*, 2002, vol. 38, pp. 1669–1670.

[56] Fimmprom, a bi-directional optical propagation tool. An Inverted Optical Taper (Fiber to Chip Coupler). Web-document. Updated 2014. Referred 16.02.2014. Available: http://www.photond.com/products/fimmprop/fimmprop_applications_06.htm

[57] Doylend, J., Knights, A. Design and Simulation of an Integrated Fiber-to-Chip Coupler for Silicon-on-Insulator Waveguides. *IEEE Journal of Selected Topics in Quantum Electronics*, 2006, vol. 12, pp. 1363–1370.

[58] Almeida, V., Panepucci, R., Lipson, M. Nanotaper for Compact Mode Conversion. *Optics Letters*, 2003, vol. 28, pp. 1302–1304.

[59] Thourhout, D., Roelkens, G., Baets, R., *et al.* Coupling mechanisms for a heterogeneous silicon nanowire platform. *Semiconductor Science and Technology*, 2008, vol. 23, pp. 1–9.

[60] Tang, Y., Wang, Z., Wosinski, L., *et al.* Highly efficient nonuniform grating coupler for silicon-on-insulator nanophotonic circuits. *Optics Letters*, 2010, vol. 35, pp. 1290–1292.

[61] Yang, J., Zhou, Z., Jia. H. High-performance and compact binary blazed grating coupler based on an asymmetric subgrating structure and vertical coupling. *Optics Letters*, 2011, vol. 36, pp. 2614–2616.

[62] Vermeulen, D., Selvaraja, S., Verheyen. P. High-efficiency fiber-to-chip grating couplers realized using an advanced CMOS-compatible Silicon-On-Insulator platform. *Optics Express*, 2010, vol. 18, pp. 18278–18283.

[63] Hecht, E. *Optics*. 4th ed. San Francisco, CA, US, Addison Wesley, 2002.

[64] Soto-Crespo, J., Nieto-Vesperinas, M. Electromagnetic scattering from very rough random surfaces and deep reflection gratings. *Optical Society of America*, 1989, vol. 6, pp. 367–384.

[65] Novotny, L., Hecht, B. *Principles of Nano-Optics*. New York, Cambridge, 2006.

[66] Kim, M. *Digital Holographic Microscopy*. London, Springer Science + Business Media, 2011.

[67] Feynman, R. *Lectures in Physics*. US, Basic Books, 2013.

[68] Sharma, K. *Optics:Principles and Applications*. Burlington, MA, US, Academic Press, 2006.

[69] Palmer, C., Loewen, E. *Diffraction Grating Handbook*. 6th ed. Rochester, New York, US, Newport Corporation, 2005.

[70] Pavesi, L., Vivien, L. *Handbook of Silicon Photonics*. Florida, US, Taylor & Francis, 2013.

[71] Wang, B., Jiang, J. *et al.* Compact slanted grating couplers. *Optics Express*, 2004, vol. 12, pp. 3313–3326.

[72] Ang, M., Reed, G., Vosonici. A. *et al.* Blazed grating couplers in Unibond SOI. *SPIE*, 1999, vol. 3896, pp. 360–368.

[73] Wu, S., Glytsis, E. *et al.* Optimization of finite-length input volume holographic grating couplers illuminated by finite-width incident beams. *Applied Optics*, 2005, vol. 44, pp. 4435–4436.

[74] Brazas, J., Li, L. Analysis of input-grating couplers having finite lengths. *Applied Optics*, 1995, vol. 34, pp. 3786–3792.

[75] Moharam, M. Coupled -Wave Analysis of Two -Dimensional Dielectric Gratings. *SPIE*, 1988, vol. 883, pp. 8–11.

[76] Taillaert, D., Chong, H., Borel. P. *et al.* A Compact Two-Dimensional Grating Coupler Used as a Polarization Splitter. *IEEE Photonics Technology Letters*, 2003, vol. 15, pp. 1249–1251.

[77] Ghizoni, C., Chen, B., Tang. C. *et al.* Theory and Experiments on Grating couplers for Thin-Film Waveguides. *IEEE Journal of Quantum Electronics*, 1976, vol. 12, pp. 69–73.

[78] Potton, R. Reciprocity in Optics. *Reports on Progress in Physics*, 2004, vol. 67, pp. 717–754.

[79] Herzig, H. *Micro-Optics: Elements, Systems And Applications*. London, Taylor & Francis, 1997.

[80] Tervo, J., Kuittinen, M., Vahimaa, P., Turunen, J., *et al.* Efficient Bragg-waveguide grating analysis by quasi-rigorous approach based on Redheffer's star product. *Optics Communications*, 2001, vol. 198, pp. 265–272.

[81] Orobtchouk, R., Layadi, A., Gualous. H. *et al.* High-efficiency light coupling in a submicrometric silicon-on-insulator waveguide. *Applied Optics*, 2000, vol. 39, pp. 5773–5777.

[82] Roelkens, G., Thourhout, D., Baets. R. High efficiency Silicon-on-Insulator grating coupler based on a poly-Silicon overlay. *Optics Express*, 2006, vol. 14, pp. 11622–11630.

[83] Du, D., Hwang, F. *Computing in Euclidean Geometry*. World Scientific Publishing, Co. Pte. Ltd., 1992.

[84] Oven, S. A Survey of Unstructured Mesh Generation Technology.*IMR*, 1998, pp. 239–267.

[85] George, P., Frey, S. *Mesh Generation*. 2nd ed. Hoboken, Wiley, 2008.

[86] Zhu, Y., Cangellaris, A. *Multigrid Finite Element Methods for Electromagnetic Field Modeling*. Hoboken, New Jersey, US, John Wiley & Sons, 2006.

[87] Orfanidis, S. *Electromagnetic Waves and Antennas*. 5th ed. Helsinki, Otatieto, 2008.

[88] Goodman, J. *Fourier Optics*. 3rd ed. Greenwood Village, US, Roberts & Company, 2005.

[89] Halir, R., Cheben, P., Janz, S., *et al.* Waveguide Grating Coupler With Subwavelength Microstructures. *Optics Letters*, 2009, vol. 34, pp. 1408–1410.

[90] Comsol AB. *Comsol Multiphysics, Quick Start and Quick Reference, version 3.5a.* 2008.

[91] Lindell, I. *Aaltojohtoteoria.* Helsinki, Otatieto, 1997.

[92] Snyder, A. Excitation and Scattering of Modes on a Dielectric or Optical Fiber. *IEEE Transactions on Microwave Theory and Techniques*, 1969, vol. 17, pp. 1138–1144.

[93] Kravtsov, Y., Berczynski, P. Description of the 2D Gaussian Beam Diffraction in a Free Space in Frame of Eikonal-Based Complex Geometric Optics. *Wave Motion*, 2004, vol. 40, pp. 23–27.

[94] Gbur, G., Wolf, E. The Rayleigh Range of Gaussian Schell-Model Beams. *Journal of Modern Optics*, 2009, vol. 48, pp. 1735–1741.

[95] Chen, X., Li, C., Fung, C. Apodized Waveguide Grating Couplers for Efficient Coupling to Optical Fibers. *IEEE Photonics Technology Letters*, August 2010, vol. 22, pp. 1156–1158.

[96] Kraus, J., Fleisch, D. *Electromagnetics With Applications.* 5th ed. US, McGraw-Hill, 1999.

[97] Comsol AB. *Comsol Multiphysics, RF Module User's Guide, version 4.3.* 2012.

[98] Johnson, S. Notes on Perfectly Matched Layers (PMLs). Lecture Notes, Massachusetts Institute of Technology, Massachusetts, US, 2008.

[99] Antelius, M., Gylfason, K., Sohlström, H. An apodized SOI waveguide-to-fiber surface grating coupler for single litography silicon photonics. *Optics Express*, 2011, vol. 19, pp. 3592–3598.

[100] Wirth, J. Silicon Grating Couplers for Low Loss Coupling Between Optical Fibers and Silicon Nanowires. M.Sc. Thesis, Purdue University, Electrical and Computer Engineering, West Lafaytte, Indiana, US, 2011.

A Silicon band diagram and conductivity

Silicon band diagram describes the dependency of charge carrier energy on the wavenumber k. Each band of the diagram describes possible energies $E(k)$ for a wide range of wavenumbers . Therefore, a particle with a wavenumber k can have different amounts of energy, depending on the band. This is different from a free particle, which has energy proportional to k^2 [12, pp. 163]. In periodic lattice, such quadratic dependency is only valid in low energies and small wavenumbers, near to the Γ-point of the diagram [12, pp.171].

Silicon lattice can be represented as a periodic potential, which affects on the electron energy. Origin of this potential is the electrical interaction between the charge carriers and the atomic nuclei. Huge size and periodicity of the silicon crystal structure guarantee periodicity of the potential experienced by the charge carriers. [12, pp. 159] Such periodicity leads to a Fourier series representation of the potential [12, pp. 160]. This determines the reciprocal lattice of the crystal.

Infinite periodic potential shapes the wavefunctions of the charge carriers. These wavefunctions can be assumed periodic as well. They can be described by Bloch waves

$$\psi_{\mathbf{k}}(\mathbf{r}) = u(\mathbf{r})\, e^{i\mathbf{k}\cdot\mathbf{r}}, \tag{A.1}$$

which are associated to the wavevector $\mathbf{k}$. Bloch waves can be considered as modulated planewaves with lattice periodicity. In the other words, amplitude u has similar periodicity to the lattice. Consequently, adding lattice vector $\mathbf{G}$ to k does not change the Bloch wave. Hence, energy is periodic in $\mathbf{G}$. [12, pp. 161–162]

Bloch waves can be considered as extensions of single silicon atom wavefunctions. These wavefunctions are associated with different energy states of an atom. Therefore, their energies are separated with gaps. [12, ch. 7.3] However, energy of each state depends on $\mathbf{k}$ because silicon lattice appears different in different directions and for different wavelengths. As a result, single atom energy states spread and become dependent on k. These spread states are the energy bands of the diagram.

In tight binding approximation wavefunctions can be written as

$$\psi_{\mathbf{k}}(\mathbf{r}) = \sum_n \phi_n(\mathbf{r} - \mathbf{r}_n)\, e^{i\mathbf{k}\cdot\mathbf{r}_n}, \tag{A.2}$$

where ϕ_n are the atomic eigenfunctions [12, pp. 169]. These functions can be

characterized as Bloch waves. Energy of such wave can be calculated as

$$E(\mathbf{k}) = \frac{\langle \psi_{\mathbf{k}} | H | \psi_{\mathbf{k}} \rangle}{\langle \psi_{\mathbf{k}} | \psi_{\mathbf{k}} \rangle}, \tag{A.3}$$

where H is the Hamiltonian in the Schrödinger equation [12, pp. 168]. H describes energy of a particle, and is simplified with no far interactions. The diagram of Ch. 2 is obtained, when the interaction is considered with nearest neighbour atoms for each atomic eigenfunction [12, pp. 168].

Typically, the band diagram is represented in some symmetry plane of the crystal [12, pp. 173]. On the selected plane, the band diagram repeats itself with a period of G. However, any other plane could be chosen as well. Together these planes span a surface, which represents an unit cell in the reciprocal space. Such unit cell represents one period of the three dimensional band structure of the crystal. Generally, it is called the first Brillouin zone [12, pp. 173]. Periodicity allows for representing crystal characteristics within the first Brillouin zone and different planes of symmetry.

It is a well known principle in materials science that a full band does not conduct current when an electric field is applied [12, pp. 246]. Electrical current requires more charge carriers with either positive or negative values of wavevector. In the other words, the charge carriers have to move collectively to the direction set by the field. However, full band has equal amounts of opposite moving charge carriers [12, ch. 9.2]. The impact of electric field can be summarized to the following equation [12, pp. 243]:

$$\hbar \frac{d\mathbf{k}}{dt} = q\mathbf{E}. \tag{A.4}$$

Equation A.4 requires change in the wavenumber when electric field is present. On a partially filled band this means that the charge carriers are drifted to the other side of the band. Hence, electric field creates a situation with collectively moving charge carriers. In silicon, this is enabled by thermal excitations of the charge carriers from the valence band (lower E) to the conduction band (higher E). The excited charge carriers leave the band partially filled.

B Radiation by PML divided in two materials

This appendix shows the failure of PML (perfectly matched layer) divided in two subdomains by a material interface. Two structures are studied as an example. The first structure contains an ideal mirror (electric field zero condition) between two homogeneous half spaces of similar material. The second structure has the same geometry divided by the mirror in two materials with different indices of refraction. The both structure are excited by a plane wave background field:

$$\mathbf{E} = \hat{\mathbf{z}} E_0 e^{-ik_0 ny}. \tag{B.1}$$

In a working model, the plane wave ideally reflects from the mirror. The reflection has an opposite phase to the incident field. Therefore, the superposition of the counterpropagating waves creates a standing wave:

$$\mathbf{E}_{sum} = \hat{\mathbf{z}} E_0 \left[e^{-ik_0 ny} - e^{ik_0 ny} \right] = -2i\hat{\mathbf{z}} E_0 \sin\left(k_0 ny\right). \tag{B.2}$$

This interference pattern does not depend on the lower material because the incident wave never passes through the mirror. Hence, the field on the back side of the mirror is ideally zero. However, with nonhomogeneous PML, an intense field appears on the lower material. This field is radiated from the PML towards the mirror where it reflects back producing a standing wave pattern.

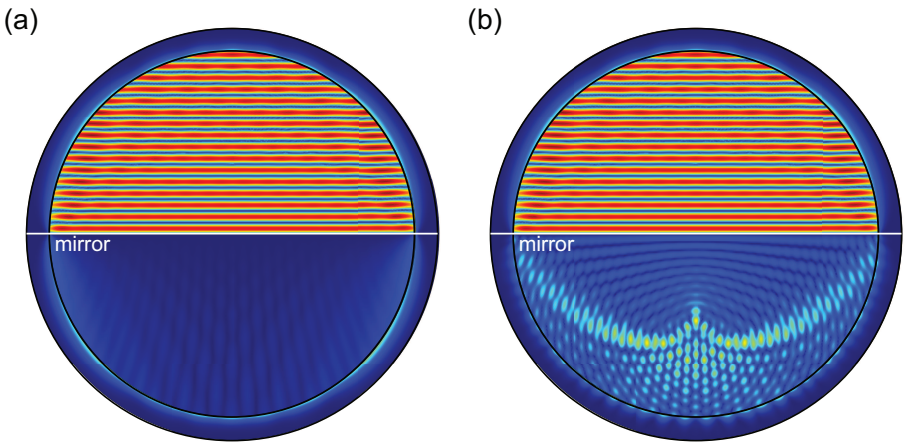

Figure B.1: Radiation by PML. (A) shows the example structure when only one material is present. (B) shows the same structure with a nonhomogeneous PML. Red color denotes the highest electric field strength. The figure describes a 2D-model.

C The mesh utilized in the simulations

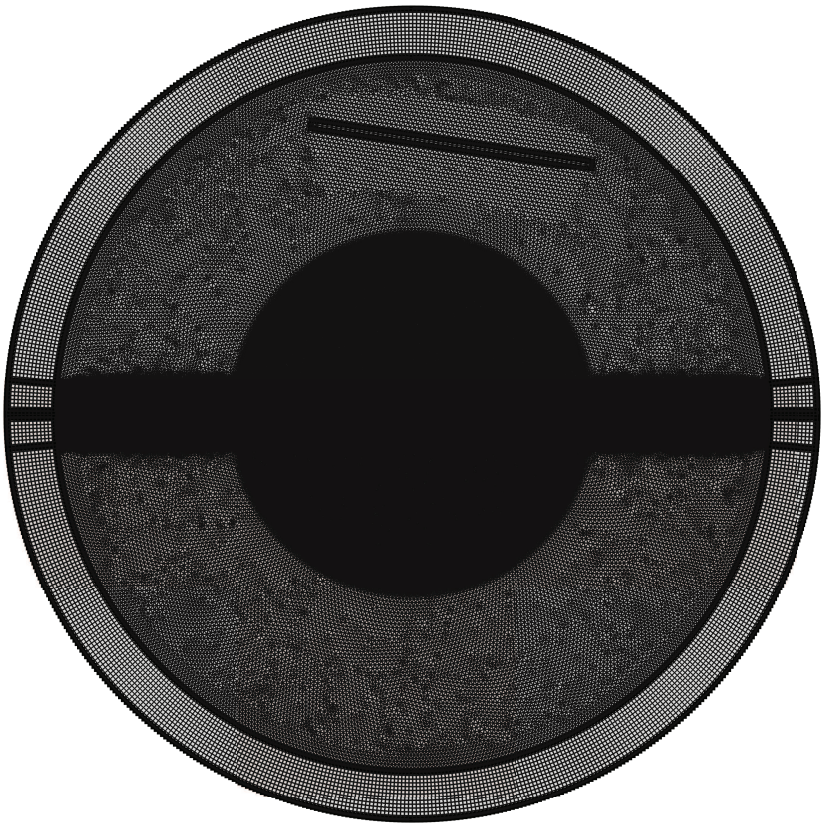

Figure C.1: Overview of the utilized mesh. (Zoom in to distinguish more details.)

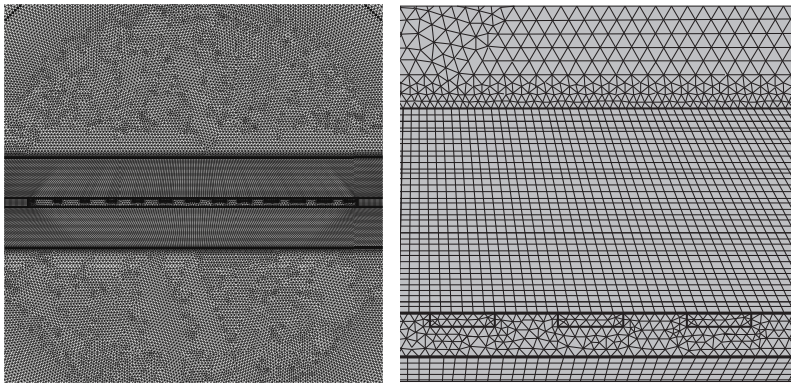

Figure C.2: Mesh in the central regions of the model.